INTEGRATING MACHINE LEARNING WITH LEVEL SET METHOD FOR MEDICAL IMAGE SEGMENTATION

AGUS PRATONDO

(B. Eng., M. Eng., Bandung Institute of Technology)

A THESIS SUBMITTED FOR THE DEGREE OF DOCTOR OF PHILOSOPHY

DEPARTMENT OF ELECTRICAL AND COMPUTER ENGINEERING

NATIONAL UNIVERSITY OF SINGAPORE

2016

Declaration

I hereby declare that this thesis is my original work and it has been written by me in its entirety. I have duly acknowledged all the sources of information which have been used in the thesis.

This thesis has also not been submitted for any degree in any university previously.

Agus Pratondo

16th November 2016

Acknowledgments

In the name of Allah, the Beneficent, the Merciful

I would like to take this opportunity to express my gratitude to people who have contribution to my successful study. Many people, in one way or another, have helped to make this thesis a reality. I can only mention a few of them here.

I would like to thank my supervisor, Prof. Ong Sim Heng, for letting me be one of his students, and guiding me during my Ph.D. candidature. Both this thesis and my research publications would not have been possible without his guidance, patience, and understanding.

I would also like to thank my co-supervisor, Prof. Chui Chee Kong, for his mentorship, advice and encouragement. Without his support, my achievement would not be so much in the journey of pursuing my Ph.D.

My appreciation also goes to Nguyen Phu Binh, for providing his insightful discussions and suggestions on my research work. I enjoy every inspiring discussion and feel lucky to have the opportunity to work with him.

Many thanks go to all group members: Wen Rong, Duan Bin, Cai Lile, Chin Boon, Chen Xuan, and Yvonne for their friendship.

It is nice to have them as team members. Special thanks to the lab officers, Md. Hamidah, Md. Hoey, and Mr. Sakthi, who have helped me a lot since I came to the Control and Mechatronics Lab 1.

I would like to acknowledge the financial, academic and technical supports from the National University of Singapore (NUS) through research scholarship program. I am sure, the university will be the leading university for quality student engagement and partnerships globally. I also would like to acknowledge the supports from the ASEAN University Network and the Southeast Asia Engineering Education Development Network Project (AUN/SEED-Net). I believe it will be successful in promoting human resource development in engineering in ASEAN.

Last but not the least, I would like to thank my mother who raised me in all my pursuits, my wife who gives all her best efforts to take care our children, and all my children who are very patient during my candidature. I know they always pray for me. I love them so much.

Summary

Many segmentation methods have been proposed but none is universally applicable, especially for medical images. The level set method (LSM) is popular in medical image segmentation since it can be used to minimize the energy functional and make the solutions more elegant, e.g., the use of LSM for active contour models. However, some difficulties often arise for particular implementations, e.g., sensitive to initialization and parameter tuning. Another popular approach is the use of machine learning algorithms to classify each pixel based on training data which is able to handle complex patterns. However, further post-processing such as morphological operation is often required to find the final solution which is no objective function inside. To overcome the limitation of those approaches, we present some integration of machine learning algorithms and active contour models using the level set methods.

Firstly, we utilize machine learning algorithms to obtain rough segmentation results. Morphological opening is applied to refine the results where the boundaries are close enough to the true boundary. Subsequently, edge-based active contours are utilized to find the desired boundaries through energy minimization using the level set method. Generally, the better the coarse

initialization is, the better the final result will be. The edge-based active contour using the LSM improves the accuracy of the final segmentation. Since there is no one ML algorithm that outperforms all the others, it is important to choose an appropriate ML algorithm. Among the investigated machine learning algorithms, the integration of the k-nearest neighbors and support vector machines with the edge-based active contour generally gives more accurate results.

Secondly, we propose a framework to construct a group of edge-stop functions (ESFs) for edge-based active contour models to segment objects with poorly defined boundaries. Traditional ESFs utilize only gradient information, which fails to stop contour evolution at such boundaries because of the small gradient magnitudes. In our framework, which incorporates gradient information as well as probability scores from a standard classifier, the ESF can be constructed from any classification algorithm and applied to any edge-based model using a level set method. Experiments on medical images using the distance regularized level set for edge-based active contour models as well as the k-nearest neighbors and the support vector machine confirm the effectiveness of the proposed approach.

Finally, we propose a framework which integrates machine learning algorithms with region-based active contour models. Classification probability scores from machine learning algorithms, which are regularized using a particular non-linear function, are used to replace the pixel intensity in the process of minimizing

the energy functional. An experimental implementation by integrating the k-nearest neighbors as well as the support vector machine with the Chan-Vese method confirms the improved results compared to other methods. Furthermore, the solutions can be obtained easily with lower sensitivity to parameter tuning.

Contents

Abbreviations xi

List of Figures xiii

List of Tables xvi

1 Introduction **1**

1.1 Background and Motivation 1

1.2 Thesis Contributions 3

1.3 Thesis Organization 5

2 Literature Review **7**

2.1 Medical Image Segmentation Methods 7

2.2 Machine Learning 9

2.2.1 Machine Learning Algorithms 11

2.2.2 Mixture Model 18

2.2.3 Reinforcement Learning 19

2.3 Level Set Method in Image Segmentation 21

2.4 Random Field Model and Graph Cut for Image Segmentation 30

2.5 Segmentation Quality Assessment 32

3 Combinatorial Method for Medical Image Segmentation **35**

3.1 Introduction 35

3.2 Proposed Framework 36

3.3 System Modeling 39

3.4 Element Design 40
3.5 Segmentation Methods 41
3.6 Path Finding 44
3.7 Implementation 46

4 Active Contour with Initialization from Classification Algorithms 48
4.1 Introduction 48
4.2 Proposed Framework 51
4.2.1 Initialization 51
4.2.2 Training 53
4.2.3 Testing 53
4.3 Results and Discussions 55
4.3.1 Experimental Setup 55
4.3.2 Results 57
4.3.3 Discussion 57
4.4 Summary 65

5 Active Contour with Gradient and Class Probability 67
5.1 Introduction 67
5.2 Proposed Framework 68
5.3 Experimantal Setup 71
5.3.1 Data Set 71
5.3.2 Parameter Setting and Quality Assessment 74
5.3.3 How the Proposed Method Works 77
5.4 Results and Discussions 77
5.5 Summary 86

6 Active Contour with Region of Class Probability **87**

6.1 Introduction 87

6.2 Proposed Framework 88

6.3 Experimental Setup 90

6.3.1 Data Set 92

6.3.2 Parameter Tuning 92

6.3.3 Quality Assessment 94

6.3.4 How the Proposed Method Works 95

6.4 Results and Discussions 96

6.5 Summary 101

7 Conclusions and Future Work **103**

7.1 Conclusions 103

7.2 Future Work 105

References **108**

List of Publications **127**

Abbreviations

k-NN	k-Nearest Neighbors.
AC	Active Contour.
ANN	Artificial Neural Networks.
DRLSE	Distance Regularized Level Set Evolution.
ELM	Extreme Learning Machine.
ESF	Edge-stop Function.
JI	Jaccard Index.
LSM	Level Set Method.
ML	Machine Learning.
NBC	Naive Bayesian Classifier.
RF	Random Forest.

RL	Reinforcement Learning.
SI	Similarity Index.
SVM	Support Vector Machine.

List of Figures

2.1 An example for computing k-NN socres. 13

2.2 Function φ transforms data from lower to higher dimensional space. It is easier to separate the data in higher dimensional space. 14

2.3 A simple perceptron 15

2.4 Scheme of feed-forward neural networks 16

2.5 Interaction between an agent and its environment 20

2.6 Curves with parameter $\in [0, 1]$. A simple closed curve holds when $\mathcal{C}(0) = \mathcal{C}(1)$. 22

2.7 Implicit contours through zero level set lines. The red lines indicate the isocontour where $\phi(x) = 0$ 23

2.8 Information for image labeling. 31

3.1 An example of a combinatorial among modalities, organs, and methods. 36

3.2 Proposed framework. 38

3.3 Three basic elements of the model. 39

3.4 Sequence of process and function. 42

3.5 Path construction for $\ell = 4$. 44

3.6 Some paths, indicated with colored line. 45

4.1 Flowchart for the proposed framework 52

4.2 An example of: (a) an original image, (b) initializations, (c) a binary classification result using NBC, (d) a segmentation result after applying a morphological operator. 54
4.3 Segmentation results for the liver tumor. 61
4.4 Segmentation results for the brain tumor. 62
4.5 Segmentation results for the renal cyst. 63
4.6 Segmentation results using (a) only the SVM and (b) the SVM + AC. The green, magenta, and red line indicate the ground truth, the result using only the SVM, and the result using the SVM+ AC, respectively. 64

5.1 The proposed framework. 69
5.2 Gradient map, regularized probability score map, and their integration. 72
5.3 (a) User initialization containing red and green marks on the brain tumour image, (b) an initial contour is generated from the red-mark boundary, (c) the contour after 10 iterations, (d) the contour after 40 iterations. For convenience, images (b)−(d) are shown in contrast enhancement. 73
5.4 Maps of ρ using various k on a liver tumor image. 75
5.5 Using only ρ as the stop function for various images does not work. Red solid lines denote the final segmentation, blue dotted lines the initialization contour, and green dashed lines the ground truth. 78
5.6 Segmentation results for the brain tumor using various methods 79
5.7 Segmentation results for the liver tumor using various methods 80
5.8 Segmentation results for the renal cyst using various methods 81

5.9 Results from various initializations on the brain tumor image. 85

6.1 Various types for regularization function. 91

6.2 User initialization and the corresponding binary result using Equation (6.1). 93

6.3 Regularized probability score map using Equations (a) 6.2 and (b) 6.6 in pseudo-color. 94

6.4 Segmentation results for the renal cyst using various methods 97

6.5 Segmentation results for the liver tumor using various methods 98

6.6 Segmentation results for the brain tumor using various methods 99

List of Tables

4.1 Segmentation performance for the liver tumor datasets (CT images) 57

4.2 Segmentation performance for the brain tumor datasets (MR images) 58

4.3 Segmentation performance for the renal cyst datasets (US images) 58

4.4 Computational time to complete the segmentation tasks 65

5.1 Preliminary results for the JI on the value of k 74

5.2 Preliminary results for the SI on the value of k 76

5.3 Computational time (in second) 82

5.4 Segmentation accuracy from various methods 83

5.5 Segmentation accuracy using Equation (5.5) 83

6.1 Image data set 92

6.2 Parameter setting for the experiments 93

6.3 Comparison of segmentation accuracy 96

6.4 Segmentation accuracy using Equation (6.6) 100

6.5 Computational time (in second) 101

Chapter 1

Introduction

1.1 Background and Motivation

Image segmentation plays an important role in medical image analysis in partitioning the region or structure of interest based on similarity of features or characteristics [1]. Segmentation is used widely to diagnose abnormalities, identify tumors, construct models for surgical planning, and plan medical treatment [2]. Depending on the degree of user intervention, medical image segmentation can be categorized into three types: manual, semi-automatic, and fully-automatic segmentation [3, 4]. Manual segmentation by an expert is not only tedious but also very time consuming. However, it may generate a precise result which can be used as ground truth during experiments in semi- as well as fully-automatic segmentation [5]. While fully automatic segmentation does not need any intervention, a semi-automatic segmentation requires user interaction and more preferable due to better performances.

Many medical image segmentation algorithms have been proposed and no single algorithm can perform well to handle all cases because each organ or tissue has its own unique characteristics. The use of energy minimization

in image segmentation has been popular since Kass et al. introduced the snake model [6]. Among energy-minimization based, the level set method (LSM) in image analysis has received much attention. It is used to minimize an energy functional when segmenting an object. The basic idea of the LSM was first described in [7] and was popularized by [8]. Subsequently, the active contour model using the LSM was applied to image segmentation.[9, 10].

Generally, existing image segmentation models using level set methods can be grouped into two categories: edge-based models and region-based models [11, 12, 13, 14]. Edge-based models utilize edge information while region-based models utilize a region descriptor to control the motion of the active contour [15]. Edge-based models are not sensitive to inhomogeneity of image intensities, i.e., the overlapping of the intensity ranges, but are sensitive to objects with poorly defined boundaries. In images where intensities change gradually in the vicinity of a poorly defined boundary, the edge-stop function (ESF) fails to stop the contour [16]. On the other hand, region-based models are not sensitive to objects with poorly defined boundaries but are sensitive to inhomogeneity of image intensities, i.e., the overlapping of the intensity ranges. Furthermore, they are also sensitive to parameter tuning [17, 18] which are not desirable in practical use.

Another popular approach is the use of machine learning (ML) algorithms to classify each pixel based on training data. A number of the algorithms appear in literature such as the k-nearest neighbors (k-NN), support vector machine (SVM), extreme learning machine, etc [19, 16]. These algorithms can handle complex patterns; however, further post-processing such as morphological operations are often required to find the final solution

which has no objective function inside.

To overcome the limitation of those approaches, we present some integration of machine learning algorithms and active contour models using the level set methods.

1.2 Thesis Contributions

Integrated methods have become more popular since they can incorporate the advantages of each component method. We are interested in integrating ML based approaches with active contour models using the LSM. Some questions related to the integrations are described below.

1. *Among various ML algorithms, which algorithm tends to generate good initializations?* In edge-based active contour model, contour initializations contribute an important role for segmenting objects. The use of ML algorithms to generate good initializations is well known and found in the literature; however, the studies only focus on a single algorithm. We intend to conduct a comparison of various ML algorithms to observe the accuracy of each algorithm and recommend particular algorithms that generally produce good initializations. The results are useful for those who utilize ML algorithm as an intermediate steps to generate rough segmentation results to initialize the contour.

2. *How do we create a family of edge-stop functions that is robust and insensitive to low gradient magnitudes?* The use of gradient magnitude for the stop-function in edge-based active contour model is not

adequate when segmenting objects with poorly defined boundaries. More information to indicate the vicinity of boundaries is required. One possible solution is the use of the classifier probability score from ML algorithms where the the values change gradually from the foreground to the background. Pixels with score 0 or 1 are clearly classified as background and foreground, respectively. A value of 1 is given. In contrast, pixels with score 0.5 are ambiguous and a value of 0 is given due to the ambiguity. A function $\rho(s)$ for mapping the probability scores to values $[0, 1]$ is defined. The function ρ is used to improve the performance of traditional ESFs.

3. *How to enhance the accuracy as well as the computational time of the well-known region-based active contour model, i.e., the Chan-Vese method by utilizing classifier probability score from ML algorithms?* The use of the classifier probability score is applicable not only to the edge-based but also to the region-based active contour model, e.g., the Chan-Vese method. The scores replace the role of pixel intensity values in the process of minimizing the energy functional. Results indicate the enhancement of the performance as follows:

   (a) improving the accuracy,

   (b) reducing the computational time,

   (c) reducing the sensitivity to parameter tuning.

1.3 Thesis Organization

This thesis is organized as follows. Chapter 2 provides the literature review of the related works. The theories as well as the equations related to our works are briefly described here. Firstly, we review image segmentation in general including categorization based on some aspects. Secondly, the review of ML algorithms used in our work is presented, i.e., k-nearest neighbors, support vector machine, extreme learning machine, naive Bayesian, artificial neural networks, and random forest. Thirdly, a brief description of the edge-based and region-based active contour models using the LSM is introduced. Popular methods namely active contours are shortly reviewed namely the active contour model without edge proposed by Chan and Vese [15], and the edge-based active contour proposed by Li et al [20]. Lastly, some measurements for segmentation quality assessment are reviewed, e.g., Jaccard index and the Dice overlap (similarity index).

Chapter 3 describes a big framework for combinatorial methods in medical image segmentation. The combination covers different imaging modalities and organs. Possible combinations of methods are represented as function compositions where the number of functions may vary. Theoretically, there are many possible combinations of methods for solution candidates; however, we are interested in the combination of machine learning algorithms and the level set methods. Furthermore the combination is investigated deeply. Various ways to combine the machine learning approach and level set methods are discussed in the next three chapters.

Chapter 4 elaborates on the comparison for some ML algorithms

integrated with the LSM which is utilized by edge-based active contour model. Six selected algorithms are integrated and evaluated using various imaging modalities. The integration is implemented sequentially where the boundaries from ML algorithm results are utilized for the initial contours.

Chapter 5 introduces a robust ESF for edge-based active contour models by utilizing the classifier probability score from ML algorithms. Two ML algorithms namely the k-nearest neighbors and support vector machines are chosen to generate the class probability map. Some regularization functions for the map are introduced to enhance the traditional ESF. We also show the implementation of the enhanced ESF for the distance regularized level set evolution which is employed by the edge-based active contour model. Furthermore, quantitative results and selected segmented images from the implementation are also presented.

Chapter 6 extends the use of the classifier probability score from ML algorithms to the region-based active contour model. We use the active contour model without edge from Chan and Vese [15]. Some regularization functions for the scores are introduced. We also show how the region-based active contour subsequently use the regularized score, instead of using pixel intensity, to find the optimal solutions. A general parameter tuning is also described here for all imaging modalities.

Finally, chapter 7 concludes the previous chapters. The highlight finding from over all works are presented here. To end the conclusion, some future directions are listed which may be useful for researchers to continue our works.

Chapter 2

Literature Review

In this chapter, we present the literature review related to our proposed methods. The areas of medical image segmentation, machine learning algorithms, and level set methods for medical images are covered.

2.1 Medical Image Segmentation Methods

A number of medical imaging modalities are available in practical use and most of them generate images in gray values. We let $\mathbf{I}$ denote a medical image and $I(x, y)$ denotes the intensity at (x, y) where $x \in [1, N_x]$ and $y \in [1, N_y]$. The main objective of the segmentation process is to partition an image into regions S_k that are homogeneous with respect to one or more characteristics or features, where

$$\bigcup S_k = \mathbf{I}; \tag{2.1}$$

$$S_k \cap S_j = \varnothing, k \neq j. \tag{2.2}$$

The indices k and j lie in the interval $[1, K]$ and K is the number of sub-classes. Equation (2.1) ensures that image segmentation should be complete, while Equation (2.2) indicates that there is no overlapping segmentation results.

Depending on the degree of user intervention, medical image segmentation can be categorized into manual, semi-automatic, and fully-automatic [21]. Manual segmentation by an expert is not only tedious but also very time-consuming. However, it typically generates an accurate result which can be used as ground truth during experiments in semi- as well as fully-automatic segmentation [22]. While fully automatic segmentation does not require any intervention, a semi-automatic segmentation requires user interaction and is preferred due to better performances.

Semi- and fully-automatic segmentation in medical image analysis have attracted many researchers [23]. A classic classification of image segmentation divides segmentation into three approaches [24].

1. Pixel based: each pixel is segmented based on gray-level values without any contextual information, e.g., thresholding [25].

2. Region-based segmentation: it considers gray-levels from neighboring pixels, for example, region growing [26], split-and-merge [27], watershed segmentation[28], clustering methods [29].

3. Edge-based segmentation: all pixels are initially labelled as either being on an edge or not, with the edge pixels then linked to form contours [25].

Withey and Koles [30] introduce another view of medical image segmentation.

They use the term generation and divide the classification into three generations.

1. First generation: it includes low-level techniques where little, if any, prior information is included, for example, thresholding [25], region growing [26], and edge tracing [31].

2. Second generation: it introduces uncertainty models and optimization methods, e.g., statistical pattern recognition (supervised methods such as Bayesian classifiers [32], discriminant analysis [33], and k-nearest neighbor classification [34], and unsupervised methods using expectation-maximization [35]), C-means clustering [36], deformable models [37], graph search [38], and neural networks [39].

3. Third generation: it incorporates higher-level knowledge such as *a priori* information, expert defined rules, and object models (e.g., shape). Examples are the active shape model [40], active appearance model [41], atlas-based segmentation [42], and rule-based segmentation.

Some second generation segmentation methods which utilize ML algorithms or LSM are employed in our work. The selected ML algorithms are reviewed in Section 2.2 while while the fundamental theory of the LSM is presented in Section 2.3.

2.2 Machine Learning

Machine learning is a field of study that aims to give computers the ability to learn without explicitly being programmed [43]. Depending on the learning

methodology, machine learning algorithms can be grouped into three broad categories [44]:

1. Supervised learning: Given example inputs and their desired outputs, the goal is to learn a general rule that maps the inputs to the outputs [45]. Formally, letting $N = \{(x_1, y_1), (x_2, y_2), ..., (x_n, y_n)\}$ where $x_i \in X$ is a feature vector and $y_i \in Y$ is its label, an ML algorithm generates a function

$$f : X \to Y. \tag{2.3}$$

   Training samples are always labeled; however, labeling by experts is not practical in use.

2. Unsupervised learning: Training samples are unlabeled during the learning algorithms [46]. The system forms clusters or natural groupings of the input patterns.

3. Reinforcement learning: An interaction between a computer program with a dynamic environment in which the former must perform a certain goal (for example driving a vehicle), with no information as to whether it has moved close to its goal [47].

Both labeled and un-labeled training samples may be used to reduce the labeling cost and it can be considered as a semi-supervised learning.

Based on the desired output of a machine-learned system, machine learning algorithms can be categorized [48] as follows.

1. In classification, inputs are assigned into two or more classes. The predictor generates a model that assigns unseen inputs to one or more

of these classes. The task is handled in a supervised way.

2. In regression, outputs are continuous rather than discrete. This is also a form of supervised learning.

3. In clustering, inputs are to be divided into groups where the groups are not known a priori. This is an unsupervised task.

4. Density estimation, where the task is to find the distribution of inputs in some space.

5. Dimensionality reduction, which simplifies inputs by mapping them into a lower-dimensional space.

2.2.1 Machine Learning Algorithms

In our work, we use supervised learning specifically for pixel classification. Six supervised machine learning algorithms are selected and listed below.

Naive Bayesian Classifier

The NBC is a probabilistic classifier based on Bayes' theorem. In a particular class variable, the method assumes that the value of a certain feature is unrelated to the value of any other feature. The objective is to minimize the probability of error in a classification by always choosing the state that maximizes the posterior probability [49], which can be expressed by

$$P(c|x) = \frac{P(x|c)P(c)}{P(x)} \tag{2.4}$$

where $P(c|x)$ is the posterior probability of class given a predictor, $P(c)$ is the prior probability of class, $P(x|c)$ is the likelihood, and $P(x)$ is the prior probability of the predictor. In practice, $P(x)$ is constant and can be ignored. When dealing with continuous data, the likelihood of feature x is assumed to be Gaussian, parameterized by μ (the mean) and σ (the standard deviation). Letting x be a continuous attribute of the training data, μ_c is the mean of the values in x labeled with class c, and σ_c^2 is the variance of the value x labeled with class c, then the probability distribution of a particular value v given a class c, $p(x = v|c)$, can be computed by

$$p(x = v|c) = \frac{1}{2\sqrt{\pi\sigma_c^2}} e^{-\frac{(v-\mu_c)^2}{2\sigma_c^2}}. \tag{2.5}$$

k-Nearest Neighbors

The k-NN algorithm is a non-parametric method in pattern recognition for classification and regression [49]. It uses observations in the training set k closest in input space to x to form $\hat{Y}$ which is defined [50] as follows:

$$\hat{Y}(x) = \frac{1}{k} \sum_{x_i \in N_k(x)} y_i, \tag{2.6}$$

where $N_k(x)$ is the neighborhood of x defined by the k closest points x_i in the training sample. It provides scores in the range $[0, 1]$. The predicted label comes from the majority vote of the nearest neighbors by calculating the distance in a feature space. Some common distance functions are the Euclidean, city block, Minkowski, and Chebychev distances which are

defined by

$$D(x,q) = \begin{cases} \sqrt{\sum_{i=1}^{k}(x_i - q_i)^2} & \text{for Euclidean distance,} \quad (2.7a) \\ \sum_{i=1}^{k}|x_i - q_i| & \text{for city block distance,} \quad (2.7b) \\ \sqrt[p]{\sum_{i=1}^{k}|x_i - q_i|^p} & \text{for Minkowski distance} \quad (2.7c) \\ \max_i\{|x_i - q_i|\} & \text{for Chebychev distance.} \quad (2.7d) \end{cases}$$

The value of k should be set to an odd integer to avoid ties in binary classification [49].

Figure (2.1) shows an example how to compute a particular point where Euclidean distance is used. Assuming $k = 5$ is used, the 5 nearest points from the green point consist of 3 blue and 2 red points. The k-NN score for the green point to be classified as blue is $\frac{3}{5}$ while red is $\frac{2}{5}$. Since there are more blue points compared to the red, the k-NN will fully classify the green point as blue.

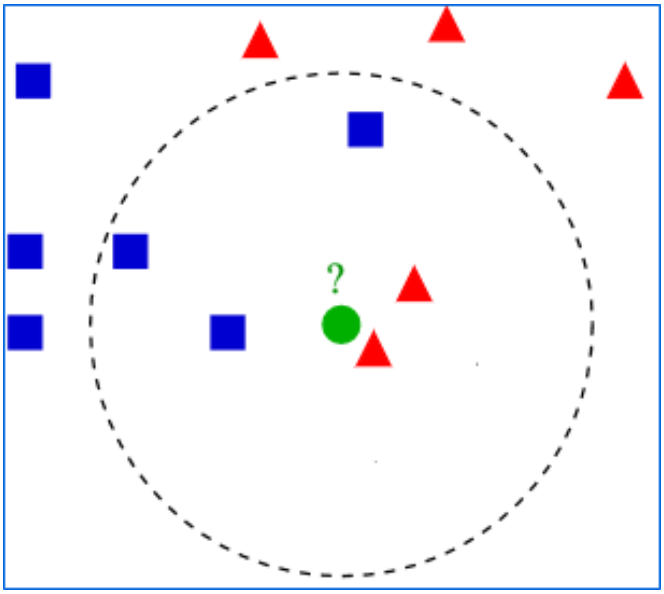

Figure 2.1: An example for computing k-NN socres.

Support Vector Machine

SVM is a supervised learning method that classifies data using the best separation hyperplane which separates the data of a class from those of another, and gives the largest margin between these two classes [51, 52]. The classification is performed by

$$\text{class}(x) = \text{sign}(h(x)) \tag{2.8}$$

where $h(x)$ is the separating hyperplane for the two classes. For linearly separable data in dimension d, the hyperplane is expressed by

$$h(x) = \mathbf{w}_0^T \mathbf{x} + b_0 \tag{2.9}$$

where $\mathbf{w}_0 \in \mathcal{R}^d$ is the optimal weight vector, $\mathbf{x} \in \mathcal{R}^d$ is the data, and b_0 is the optimal bias. Since it may be difficult to separate the data in the original input space, mapping the data into a higher dimensional space through function φ is introduced (see Figure (2.2)). Then $h(x)$ can be

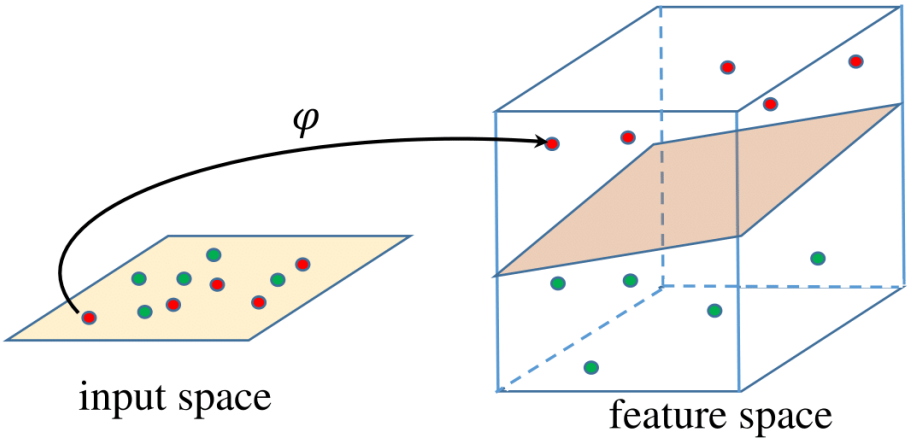

Figure 2.2: Function φ transforms data from lower to higher dimensional space. It is easier to separate the data in higher dimensional space.

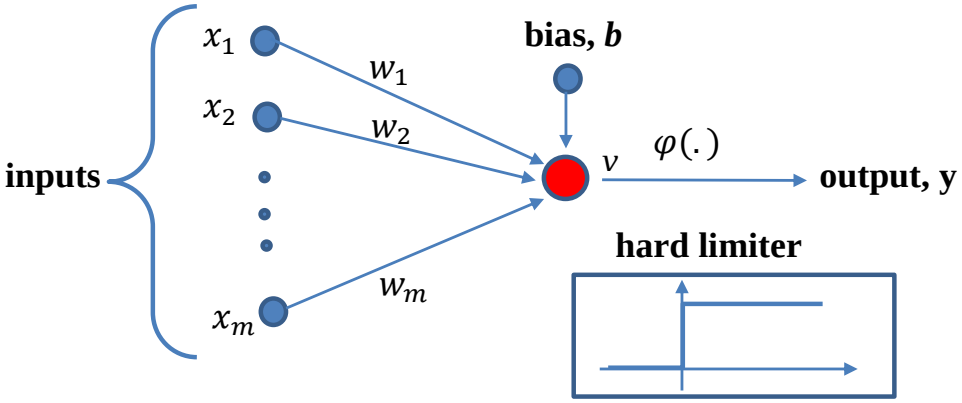

Figure 2.3: A simple perceptron

expressed as

$$h(x) = \mathbf{w}_0^T \varphi(\mathbf{x}) + b_0. \tag{2.10}$$

Finding an explicit φ is often difficult; instead, kernel [53, 54] $K(\mathbf{x}, \mathbf{x}_i)$ is used to compute directly the dot product. Subsequently, $h(x)$ is expressed by

$$h(x) = \sum_{i=1}^{N} \alpha_i y_i K(\mathbf{x}, \mathbf{x}_i) + b_0 \tag{2.11}$$

where a_i is the estimated SVM parameter, and $y_i \in \{+1, -1\}$ is the desired class for the corresponding $\mathbf{x}_i$. The value of $h(x)$ is the SVM evaluation score and the sign is the predicted class [55].

Artificial Neural Networks

Artificial neural networks (ANNs) are models inspired by biological neural networks. The idea started with a simple perceptron introduced by Frank Rosenblatt in 1958 (Figure 2.3). Letting $x = (x_1, x_2, ..., x_m)^T$ denote the feature vector, $w = (w_1, w_2, ..., w_m)^T$ the weight vector and n the iteration

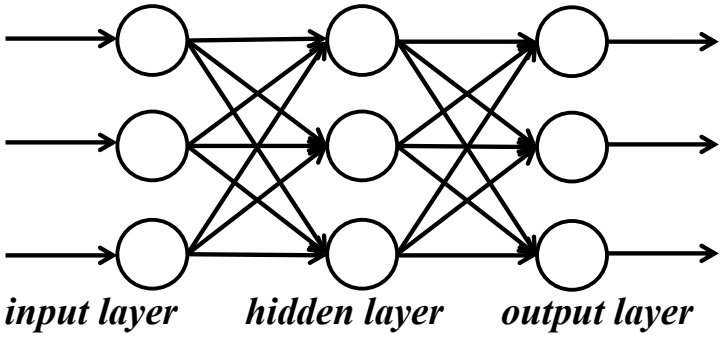

Figure 2.4: Scheme of feed-forward neural networks

steps, then

$$v(n) = \sum_{i=1}^{m} w_i(n)x_i(n) + b(n), \tag{2.12}$$

$$y(n) = \begin{cases} 1 & \text{if } v(n) > 0, \quad (2.13a) \\ 0 & \text{if } v(n) < 0. \quad (2.13b) \end{cases}$$

The concept is then expanded to the multi-layer perceptron. A popular model is the feed-forward network [56, 57, 58] (Figure 2.4). In this network, the information moves from the input nodes to the output node through the hidden nodes in one direction. The structure is simplest when there are no hidden nodes. Some important parameters for designing the network are: the number of hidden layers and hidden neurons, the activation function in the hidden layers and the output neurons, and the learning style (sequential or batch learning).

Extreme Learning Machine

The extreme learning machines (ELM) are single-hidden layer feed-forward neural networks (SLFNs) [57, 58] where the weights that connect inputs to hidden nodes are assigned randomly and learned in a single step.

According to Weimin et al. [59], the ELM provides good generalization performance at a fast learning speed. Given a training set $\aleph = (x_i, t_i)|x_i \in \mathcal{R}^n, t_i \in \mathcal{R}^m, i = 1, ..., N$, activation function $g(x)$, and hidden node number N, the ELM algorithm can be summarized as follows [60]:

1. Randomly assign input weight w_i and bias $b_i, i = 1, ..., N$.

2. Calculate the hidden layer output matrix H.

3. Calculate the output weight β

$$\beta = H^{\dagger}T \tag{2.14}$$

where $T = [t_1, ..., t_N]^T$, $H^{\dagger}$ is the Moore–Penrose generalized inverse of matrix H. The details about extreme learning machine can be found in [60].

Random Forests

The RF is based on the voting of the most popular class from a large number of trees [61]. Formally, it is defined as a classifier consisting of a collection of tree-structured classifiers $\{h(x, \Theta_k), k = 1, ...\}$ where the Θ_k are independent identically distributed random vectors and each tree casts a unit vote for the most popular class at input x. The algorithm is chosen due to its simplicity and popularity in machine learning. The RF algorithm for classification [62] is as follows.

1. From the original data, draw n_{tree} bootstrap samples

2. For each of the boot straps sample, grow a classification tree without pruning it. At each node, sample randomly m_{try} of the predictors and select the best split from among those variables.

3. For predicting new data, aggregate the predictions of the ntree trees through majority votes.

Two additional items of information from RF are:

1. Variable importance, which measures the importance of the predictor variable

2. Proximity measure : the (i, j) element of the proximity matrix produced by random forest is the fraction of trees in which elements i and j fall in the same terminal node.

2.2.2 Mixture Model

A mixture model represents the probability distribution of observations in the overall population. This probabilistic model is formed by taking linear combinations of basic distributions such as Gaussians [48, 50, 49]. Assuming there are K Gaussian densities, the mixture of Gaussians can be represented by

$$p(\mathbf{x}) = \sum_{k=1}^{K} w_k \mathcal{N}(\mathbf{x}|\mu_k, \sum_k). \tag{2.15}$$

Each component of the mixture, i.e. Gaussian density $\mathcal{N}(\mathbf{x}|\mu_k, \sum_k)$, has its own mean μ_k and covariance $\sum_k$. The parameters w_k are called mixture

weights where their properties are:

$$\sum_{k=1}^{K} w_i = 1, \tag{2.16}$$

$$0 \leq w_i \leq 1. \tag{2.17}$$

It should be noted that both $p(\mathbf{x})$ and the individual Gaussian components are normalized.

According to the sum and product rule, the marginal density for $p(\mathbf{x})$ can be expressed [48] by

$$p(\mathbf{x}) = \sum_{k=1}^{K} p(k)p(\mathbf{x}|k). \tag{2.18}$$

Equation (2.18) is equivalent to Equation (2.15) where the prior probability of picking the k^{th} component, $p(k)$, equals to w_k and the probability of $\mathbf{x}$ conditioned on k, $p(\mathbf{x}|k)$, equals to $\mathcal{N}(x|\mu_k, \sum_k)$.

Generally, mixture models can use any component densities in place of the Gaussian in Equation (2.15); however, the Gaussian mixture model is most popular.

2.2.3 Reinforcement Learning

Reinforcement learning (RL) is a field of machine learning concerned with how an agent interacts with its environment by taking actions so as to maximize its reward (Figure (2.5)) [63] [64] [65]. An RL agent learns from the consequences of its actions rather than from being explicitly taught, and it selects its actions on basis of its past experiences (exploitation) and also

by new choices (exploration) [66]. It is essentially trial and error learning.

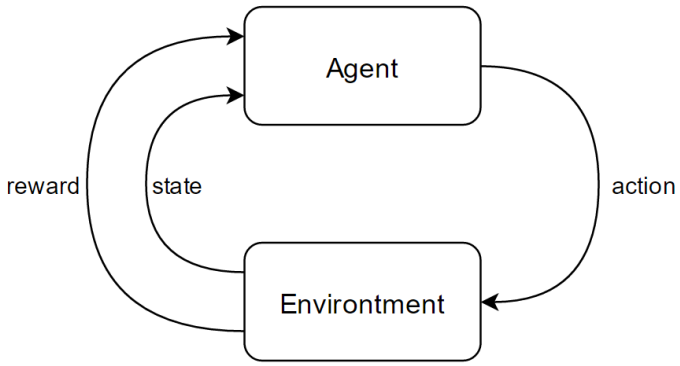

Figure 2.5: Interaction between an agent and its environment

A set of possible states for an agent is denoted by $S = \{s_1, s_2, ...\}$ and the actions by $A = \{a_1, a_2, ...\}$. The state of an agent may change through a transition function. The deterministic transition function can be expressed by

$$\bar{f}(s, a) = s', s' \in S \tag{2.19}$$

and the non-deterministic by

$$f(s, a, s') = P(s_{t+1} = s' | s_t = s, a_t = a) \equiv P^a_{ss'} \tag{2.20}$$

where $P(a|b)$ =Probability of a being true under condition b. Equations (2.19) and 2.20 denote an agent takes an action a to move from state s to s'. Subsequently, the agent receives reward r one time-step later (i.e. at s'). The reward for taking a_t at s_t at time-step t and reaching s_{t+1} can be expressed by

$$r_{t+1} = \rho(s_t, a_t, s_{t+1}) \tag{2.21}$$

where $\rho : S \times A \times S \rightarrow \mathcal{R}$ is named the reward function. For non-deterministic transitions, the reward for taking a at s is characterized by the expected

value of r_{t+1} over all possible new states:

$$\begin{aligned} E\Big[r_{t+1}\Big|s_t = s\Big] &= \sum_{s'} \Big(P^a_{ss'} r_{t+1}\Big|s_{t+1} = s'\Big) \\ &= \sum_{s'} P^a_{ss'} \rho(s, a, s'). \end{aligned} \tag{2.22}$$

If the agent continues to make transitions, the total reward is expressed by

$$\begin{aligned} R_t &= r_{t+1} + \gamma r_{t+2} + \gamma r_{t+3} + ... \\ &= \sum_{k=0}^{\infty} \gamma^k r_{t+k+1} \end{aligned} \tag{2.23}$$

where k is the index time steps after t, with $k = 0$ being first step and γ is the discount rate, with $0 \leq \gamma \leq 1$.

2.3 Level Set Method in Image Segmentation

The use of energy minimization in image segmentation has been intensively studied, starting from the snake model [6]. Through variational methods, the segmentation of a given image $I : \Omega \to \mathbb{R}$ is computed by contour evolution using appropriate partial differential equations. In the snake model proposed by Kass et al., an explicit (parametric) curve $\mathcal{C} : [0, 1] \to \Omega$ as described in Figure (2.6) is used to represent the contour which is evolved by minimizing the energy functional

$$\mathcal{E}(\mathcal{C}) = -\int |\nabla I(\mathcal{C})|^2 ds + v_1 \int |\mathcal{C}_s|^2 ds + v_2 \int |\mathcal{C}_{ss}|^2 ds, \tag{2.24}$$

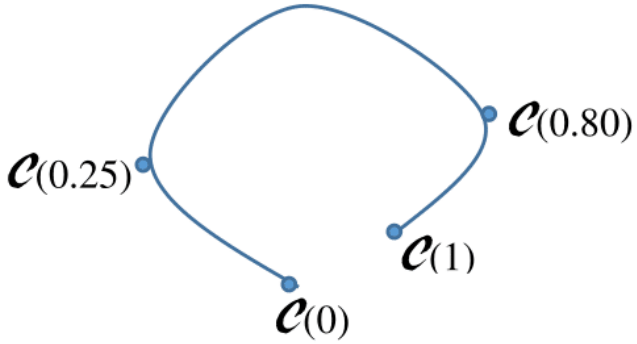

(a) an open curve

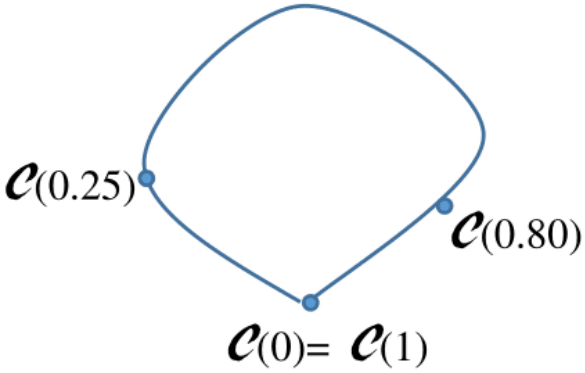

(b) a closed curve

Figure 2.6: Curves with parameter $\in [0, 1]$. A simple closed curve holds when $\mathcal{C}(0) = \mathcal{C}(1)$.

where $\mathcal{C}_s$ and $\mathcal{C}_{ss}$ denote the first and second derivative with respect to the curve parameter s. The first term in (2.24) is the external energy which accounts for the image information, in the sense that the minimizing contour will favor locations of large image gradient. The remaining two terms, weighted by non-negative parameters v_1 and v_2, are internal energy terms that measure the length of the contour and its stiffness.

Another way to implement curve $\mathcal{C}$ is by representing in implicit con-

tours the zero level line of some embedding function $\phi : \Omega \to \mathbb{R}$:

$$\mathcal{C} = \{x \in \Omega | \phi(x) = 0\}. \tag{2.25}$$

Figure (2.7) shows an example of a zero level set indicated by red lines and its corresponding segmentation results.

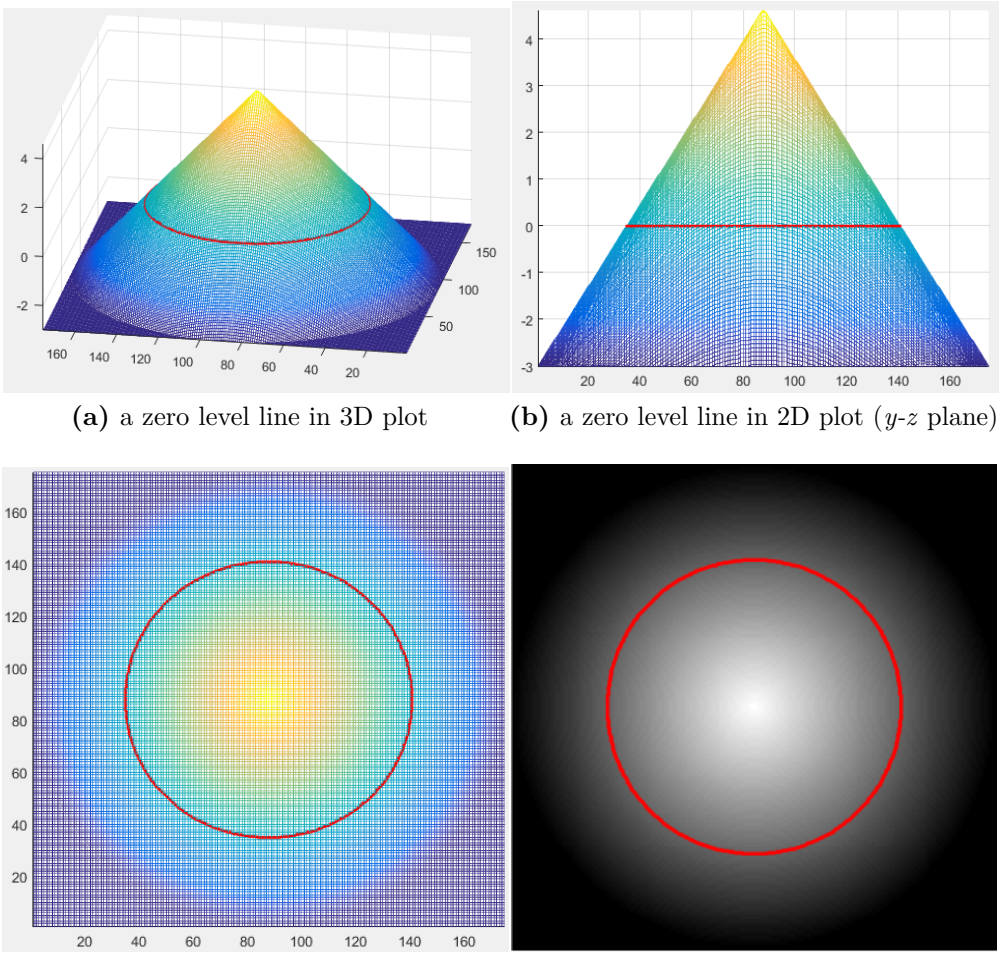

(a) a zero level line in 3D plot **(b)** a zero level line in 2D plot (y-z plane)

(c) a zero level line in 2D plot (x-y plane) **(d)** a corresponding segmentation result

Figure 2.7: Implicit contours through zero level set lines. The red lines indicate the isocontour where $\phi(x) = 0$

Among various methods to evolve the contours implicitly, the level set method (LSM) in image analysis has received much attention and is

popularly used to minimize an energy functional when segmenting an object. The basic idea of the LSM was first described in [7] and was popularized by [8]. The curve evolves along the normal n with a speed F where the following equation holds:

$$\frac{\partial \mathcal{C}}{\partial t} = F.n. \tag{2.26}$$

Since

$$\phi(\mathcal{C}(t), t) = 0 \tag{2.27}$$

at all times, the total time derivative of ϕ at locations of the contour follows

$$\begin{aligned} \frac{\partial \phi(\mathcal{C}(t), t)}{\partial t} &= \nabla\phi \frac{\partial \mathcal{C}}{\partial t} + \frac{\partial \phi}{\partial t} \\ &= \nabla\phi F.n + \frac{\partial \phi}{\partial t} \\ &= 0. \end{aligned} \tag{2.28}$$

Recalling the definition of the normal

$$n = \frac{\nabla\phi}{|\nabla\phi|} \tag{2.29}$$

we obtain the evolution equation for ϕ:

$$\frac{\partial \phi}{\partial t} = -|\nabla\phi|F. \tag{2.30}$$

The first applications of the level set formalism for image segmentation were proposed by Caselles et al. [9] and Malladi et al. [67, 68, 69]. Subsequently, Caselles et al. [70, 10] and Kichenassamy et al. [71] independently

proposed a level set formulation for (2.24) expressed by:

$$\begin{aligned}\frac{\partial\phi}{\partial t} &= |\nabla\phi|\text{div}\left(g(I)\frac{\nabla\phi}{|\nabla\phi|}\right)\\ &= g(I)|\nabla\phi|\text{div}\left(\frac{\nabla\phi}{|\nabla\phi|}\right)+\nabla g(I)\cdot\nabla\phi,\end{aligned} \tag{2.31}$$

where $g(I)$ is an edge-detector or edge-stop function (ESF). A common ESF is

$$g(I)=\frac{1}{1+|\nabla(G_\sigma * I)|^p}, p=1,2,... \tag{2.32}$$

where I is an image on a domain Ω and G_σ is a Gaussian kernel with standard deviation σ. For simplification, $g(I)$ is written as g. This approach is popular as the *geodesic active contour*.

Active Contour Model using Distance Regularized Level Set Evolution

The traditional LSF requires reinitialization to avoid irregularities during its evolution [72, 73]. Since reinitialization often leads to difficulties, Li et al. [74] proposed the distance regularized level set evolution (DRLSE) which removes the need for reinitialization.

Li et al. [74] introduced an energy functional $\mathcal{E}(\phi)$ for a level set function $\phi:\Omega\to\Re$ on a domain Ω as

$$\mathcal{E}(\phi)=\mu\mathcal{R}_p(\phi)+\mathcal{E}_{\text{ext}}(\phi) \tag{2.33}$$

where μ is a positive constant, $\mathcal{R}_p(\phi)$ is the level set regularization term,

and $\mathcal{E}_{\text{ext}}(\phi)$ is the external energy. The regularization term $\mathcal{R}_p(\phi)$ is defined as

$$\mathcal{R}_p(\phi) \triangleq \int_\Omega p(|\nabla\phi|)d\mathbf{x} \tag{2.34}$$

where p is a potential function $p : [0, \infty) \to \Re$ defined by

$$p = \begin{cases} \dfrac{1}{(2\pi)^2}(1 - \cos(2\pi s)) & \text{if } s \leq 1, \quad (2.35a) \\ \dfrac{1}{2}(s-1)^2 & \text{if } s > 1. \quad (2.35b) \end{cases}$$

The general DRLSE in (2.33) can be applied to image segmentation in the form of an active contour model utilizing edge-based information in the external energy. For image segmentation, the external energy in (2.33) is subsequently expanded by considering the length and area term which can be expressed as

$$\mathcal{E}_\epsilon(\phi) = \mu \int_\Omega p(|\nabla\phi|)d\mathbf{x} + \lambda \int_\Omega g\delta_\epsilon(\phi)|\nabla(\phi)|d\mathbf{x} + \alpha \int_\Omega g H_\epsilon(-\phi)d\mathbf{x} \tag{2.36}$$

where δ_ϵ and H_ϵ are defined [75] by

$$\delta_\epsilon(x) = \begin{cases} \dfrac{1}{2\epsilon}[1 + \cos(\dfrac{\pi x}{\epsilon})] & \text{if } |x| \leq \epsilon, \quad (2.37a) \\ 0 & \text{if } |x| > \epsilon\ , \quad (2.37b) \end{cases}$$

$$H_\epsilon(x) = \begin{cases} \dfrac{1}{2}(1 + \dfrac{x}{\epsilon} + \dfrac{1}{\pi}\sin(\dfrac{\pi x}{\epsilon})) & \text{if } |x| \leq \epsilon, \quad (2.38a) \\ 1 & \text{if } x > \epsilon\ , \quad (2.38b) \\ 0 & \text{if } x < -\epsilon\ . \quad (2.38c) \end{cases}$$

The energy functional in (2.36) can be minimized by solving the gradient

flow

$$\frac{\partial \phi}{\partial t} = \mu \text{div}(d_p(|\nabla \phi|)\nabla \phi) + \lambda \delta_\epsilon(\phi) \text{div}\left(g \frac{\nabla \phi}{|\nabla \phi|}\right) + \alpha g \delta_\epsilon(\phi). \tag{2.39}$$

The ESF g in either (2.39) or (2.31) plays an important role in stopping contour evolution and can be explored further by considering not only gradient information but also decision-boundary values in pixel classification.

Region-Based Active Contour Model

The active contour model in the original form in Equation (2.31) and in the modified form in (2.39) utilize edge detector to stop the contour. Instead of using gradient information, Chan and Vese [15] propose an active contour model using region information based on the Mumford-Shah model [76]. Chan and Vese introduced an energy functional $F(c_1, c_2, \mathcal{C})$ defined by

$$\begin{aligned} F(c_1, c_2, \mathcal{C}) = \mu.\text{Length}(\mathcal{C}) + v.\text{Area}(inside(\mathcal{C}))+ \\ \lambda_1 \int_{\text{inside}(\mathcal{C})} |u_0(x,y) - c_1|^2 dxdy+ \\ \lambda_2 \int_{\text{outside}(\mathcal{C})} |u_0(x,y) - c_2|^2 dxdy \end{aligned} \tag{2.40}$$

where $\mathcal{C}$ is the evolving curve, c_1 and c_2 are, respectively, the values of u inside and outside of C, $\mu \geq 0, v \geq 0, \lambda_1, \lambda_2 > 0$ are constants, and u_0 is the input image. The minimization problem is expressed by

$$\inf_{c_1, c_2, \mathcal{C}} F(c_1, c_2, \mathcal{C})$$

and can be accomplished by applying the level set method introduced by Osher and Sethian [8]. The curve $\mathcal{C}$ is implicitly represented by the zero level set of a Lipschitz function as shown in Equation (2.25). The sign of ϕ indicates the inside or outside of $\mathcal{C}$ expressed by

$$\begin{cases} \mathcal{C} = \partial\omega & = (x,y) \in \Omega : \phi(x,y) = 0, & \text{(2.41a)} \\ \text{inside}(\mathcal{C}) = \omega & = (x,y) \in \Omega : \phi(x,y) > 0\ , & \text{(2.41b)} \\ \text{outside}(\mathcal{C}) = \Omega \backslash \bar{\omega} & = (x,y) \in \Omega : \phi(x,y) < 0\ . & \text{(2.41c)} \end{cases}$$

The unknown variable $\mathcal{C}$ in Equation (2.40) subsequently can be replaced by the unknown variable ϕ as described in [75]. Using the Heaviside function

$$H(z) = \begin{cases} 1 & \text{if } z \geq 0\ , \quad \text{(2.42a)} \\ 0 & \text{if } z < 0\ . \quad \text{(2.42b)} \end{cases}$$

and the one-dimensional Dirac delta function

$$\delta_0(z) = \frac{d}{dz} H(z) \tag{2.43}$$

the energy functional in Equation (2.40) can be written as

$$\begin{aligned} F(c_1, c_2, \phi) = \mu \int_\Omega \delta(\phi(x,y)) |\nabla \phi(x,y)| dxdy + v \int_\Omega H(\phi(x,y)) dxdy + \\ \lambda_1 \int_\Omega |u_0(x,y) - c_1|^2 H(\phi(x,y)) dxdy + \\ \lambda_2 \int_\Omega |u_0(x,y) - c_2|^2 (1 - H(\phi(x,y))) dxdy. \end{aligned} \tag{2.44}$$

By considering the Mumford-Shah partition problem and keeping the ϕ fixed, the constants c_1 and c_2 in Equation (2.44) can be written as functions

of ϕ expressed by

$$c_1(\phi) = \frac{\int_\Omega u_0(x,y)H(\phi(x,y))dxdy}{\int_\Omega H(\phi(x,y))dxdy} \tag{2.45}$$

$$c_2(\phi) = \frac{\int_\Omega u_0(x,y)(1-H(\phi(x,y)))dxdy}{\int_\Omega (1-H(\phi(x,y)))dxdy} \tag{2.46}$$

To compute the unknown function ϕ with the help of the Euler-Lagrange equation, the functions H and δ_0 are regularized, denoted by H_ϵ and δ_ϵ, as $\epsilon \to 0$. Letting H_ϵ be any regularization of H, and

$$\delta_\epsilon = H'_\epsilon, \tag{2.47}$$

the approximation of Equation (2.44) can be expressed as

$$\begin{aligned} F_\epsilon(c_1,c_2,\phi) = \mu \int_\Omega \delta_\epsilon(\phi(x,y))|\nabla\phi(x,y)|dxdy + v\int_\Omega H_\epsilon(\phi(x,y))dxdy + \\ \lambda_1 \int_\Omega |u_0(x,y)-c_1|^2 H_\epsilon(\phi(x,y))dxdy + \\ \lambda_2 \int_\Omega |u_0(x,y)-c_2|^2 (1-H_\epsilon(\phi(x,y)))dxdy. \end{aligned} \tag{2.48}$$

In the approximation, Chan and Vese introduced the regularization of H_ϵ,

$$H_\epsilon(z) = \frac{1}{2}\left(1 + \frac{2}{\pi}\arctan\left(\frac{z}{e}\right)\right). \tag{2.49}$$

Minimizing F_ϵ with respect to ϕ by keeping c_1 and c_2 fixed and considering the associated Euler-Lagrange equation for ϕ, Chan and Vese introduced a

gradient flow

$$\frac{\partial \phi}{\partial t} = \delta_\epsilon(\phi)\left[\mu \ \mathrm{div}\left(\frac{\nabla \phi}{|\nabla \phi|}\right) - v - \lambda_1(u_0 - c_1)^2 + \lambda_2(u_0 - c_2)^2\right] = 0 \text{ in } \Omega,$$
$$\frac{\delta_\epsilon(\phi)}{|\nabla \phi|}\frac{\partial \phi}{\vec{n}} = 0 \text{ on } \partial\Omega \quad (2.50)$$

where δ_ϵ is the regularized Dirac function, Ω is a bounded open subset of $\mathbb{R}^2$ with $\partial\Omega$ its boundary, $\vec{n}$ denotes the exterior normal to the boundary, and $\frac{\partial \phi}{\vec{n}}$ denotes the normal derivative of ϕ at the boundary. Equation (2.50) contains a number of parameters that should be tuned carefully in advance [15].

2.4 Random Field Model and Graph Cut for Image Segmentation

Image segmentation can be considered as a pixel labeling problem. For binary segmentation, the task is done by classifying each pixel into a background or foreground. Given the observed data of an input image, $X = \{x_i\}_{i \in S}$, where x_i is the data from i^{th} site of the image set S, and $L = \{l_i\}_{i \in S}$ is the corresponding label at the image site, the image segmentation problem is to find L that maximizes the conditional probability $P(L|X)$:

$$L^* = \arg\max_L P\{L|X\}. \quad (2.51)$$

Let l_i be the label of the i^{th} site of the image set S and N_i be the neighboring sites of site i, as shown in Figure 2.8 [77]. The label set $L = \{l_i\}_{i \in S}$ is

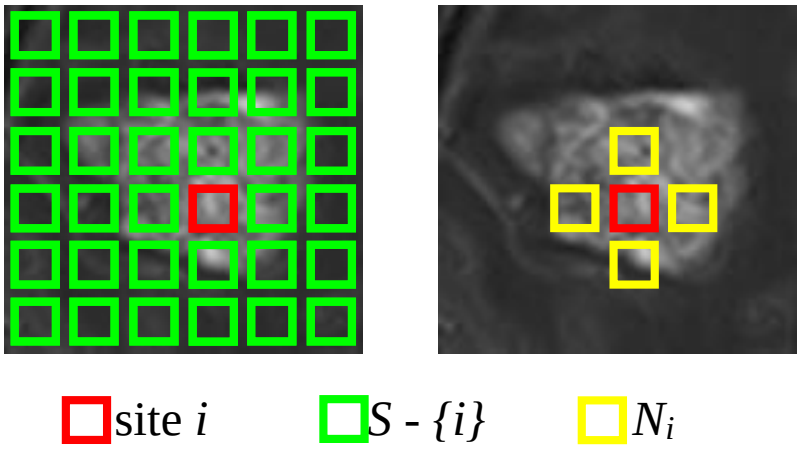

Figure 2.8: Information for image labeling.

a Markov random field on S w.r.t. a neighborhood N if and only if the following condition is satisfied:

$$P(l_i|l_{S-\{i\}}) = P(l_i|l_{N_i}) \tag{2.52}$$

where $S - \{i\}$ is the set of all sites except the site i. When conditioned on X, (X, L) is a conditional random field (CRF) [78, 79, 80, 77] if the random variables l_i follows the Markov property:

$$P(l_i|X, l_{S-\{i\}}) = P(l_i|X, l_{N_i}). \tag{2.53}$$

The solution for the optimal L^* can be done using discrete optimization based on a particular energy functional. A common form for the energy functional from literature [81, 82, 83] can be rewritten as

$$E(L) = \sum_{p\in\mathcal{P}} D_p(L_p) + \sum_{(p,q)\in\mathcal{N}} V_{p,q}(L_p, L_q), \tag{2.54}$$

where $L = L_p \in \mathcal{P}$ is a labeling of image $\mathcal{P}$, $D_p(.)$ is a data penalty function, $V_{p,q}$ is an interaction potential, and $\mathcal{N}$ is a set of all pairs of neighboring pixels. The solution can be reached by applying standard minimum cut algorithms [83] to optimize the energy functional over the segmentation.

The graph cut and level set methods have been widely used for energy-based segmentation. Each method has its own properties and advantages [84, 85]. The graph cut is based on discrete functional and the formulation is convex. Its solution achieves the global minimum and is an integer. In contrast, the level set method is a continuous functional. Its formulation is non-convex and offers solutions that are local minima. Nevertheless, the level set method for medical image segmentation has continued to be researched intensively since it can achieve high accuracy particularly when sub-pixel accuracy is required [85, 86].

2.5 Segmentation Quality Assessment

Segmentation results using a particular method can be evaluated by comparing with the ground truth. There are some ways to measure the accuracy in the literature [87]. Three of them are briefly described here.

Suppose P_1 as the extracted region by a proposed method and P_2 as the true region given by the reference standard. The union and the intersection operations are the voxel-wise minimum and maximum operations, and $|P|$ denotes the number of voxels in the region P. The following indexes can be calculated.

1. Jaccard index (JI)

   To evaluate the similarity between the segmentation result of a method and the reference standard, the Jaccard index between the extracted region and the corresponding reference standard is calculated by:

$$\mathrm{JI}(P_1, P_2) = \frac{P_1 \cap P_2}{P_1 \cup P_2} \tag{2.55}$$

   JI is 1 for a perfect segmentation result and 0 for the worst segmentation where an extracted region and the ground truth do not overlap at all.

2. The Dice overlap (or similarity index, SI)

   To account for the volume overlap, the Dice overlap (similarity index, SI) between two regions is defined by:

$$\mathrm{SI}(P_1, P_2) = \frac{2|P_1 \cap P_2|}{|P_1| + |P_2|} \tag{2.56}$$

   SI is a positive performance measure, where a higher value indicates more accurate segmentation.

3. False positive and false negative Dice

   To further characterize the segmentations by the different methods, the false positive Dice (FPD) and the false negative Dice (FND) are available as alternative measurements. Let $\bar{P}_2$ and $\bar{P}_1$ be the complements of the gold standard and the segmentation results respectively. FPD gives a measure of over-segmentation and FND of under-segmentation. FPD is expressed by

$$\mathrm{FPD}(P_1, P_2) = \frac{2|P_1 \cap \bar{P_2}|}{|P_1| + |P_2|} \tag{2.57}$$

while FND is formulated by

$$\mathrm{FND}(P_1, P_2) = \frac{2|\bar{P_1} \cap P_2|}{|P_1| + |P_2|} \tag{2.58}$$

It is worth noting that Jaccard and the similarity index are equivalent and can be expressed by

$$\mathrm{JI} = \frac{\mathrm{SI}}{2 - \mathrm{SI}} \tag{2.59}$$

or

$$\mathrm{SI} = \frac{2\mathrm{JI}}{1 + \mathrm{JI}} \tag{2.60}$$

Chapter 3

Combinatorial Method for Medical Image Segmentation

3.1 Introduction

Methods in image segmentation have improved over time. While much effort has been devoted to improving a particular method, not many studies have been done on the combination of methods, organs, and modalities. Some previous studies related to this issue can be found in the literatures such as in [88, 89]. However, a framework that specifically utilizes the combination of modalities and methods has not been studied.

In this chapter, the combination of segmentation methods and imaging modality is studied. A general framework on combinatorial medical image segmentation is proposed. However, this framework has not been fully implemented yet. This chapters plays a role to introduce our core work.

Our work is limited to two popular approaches, machine learning algorithms and the level set method. The investigation covers various combinations for the two approaches and are discussed in the next three

chapters.

3.2 Proposed Framework

We propose a framework that utilizes prior knowledge to determine the optimal method to segment a medical image. In other words, given any organ and an imaging modality, the system will recommend the suitable method(s) to segment the image.

The recommendation involves the combination of different elements as shown in Figure 3.1. The first element is an imaging modality, such as

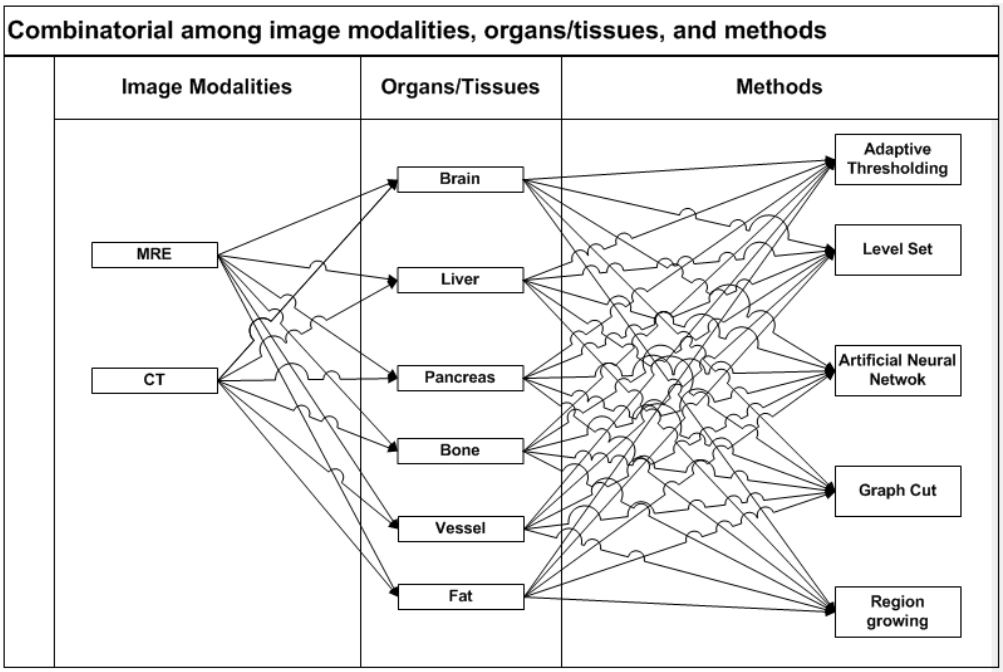

Figure 3.1: An example of a combinatorial among modalities, organs, and methods.

magnetic resonance imaging, computerised tomography, and ultrasound imaging. The second element is an organ/tissue which is the object being

diagnosed, e.g, brain tumor, liver tumor, pancreas, and renal cyst. The third element is a method, e.g., the artificial neural networks, the level set method, and the graph cuts.

The system is intended to work as follows. The inputs are the imaging modality and the specific organ. Initially, the system has no knowledge and no recommendation is given. In this case, a user is free to choose a method randomly. Each time a method is executed, the system updates the database with these elements: imaging modality, organ/tissue, method and accuracy. Over time, for a particular case, i.e., a specific imaging modality and organ/tissue, many segmentation methods may have been employed. With a new segmentation application, the system will refer to the available knowledge in the database to recommend a suitable segmentation method by selecting one that generates the minimum error (maximum accuracy). However, a user may choose another method to compare the result with the recommended method. If the results are different, the new knowledge can be added to the system, as shown in Figure 3.2.

The main engine in the framework is knowledge inference. Prior knowledge is represented in such a way it can be retrieved easily with a new case. Given a particular case with a known imaging modality and a specific organ/tissue, the system should find the most suitable method which generates minimum error. It is a field of artificial intelligence, i.e., knowledge representation and reasoning. Some issues relating to this framework are discussed in the following sections.

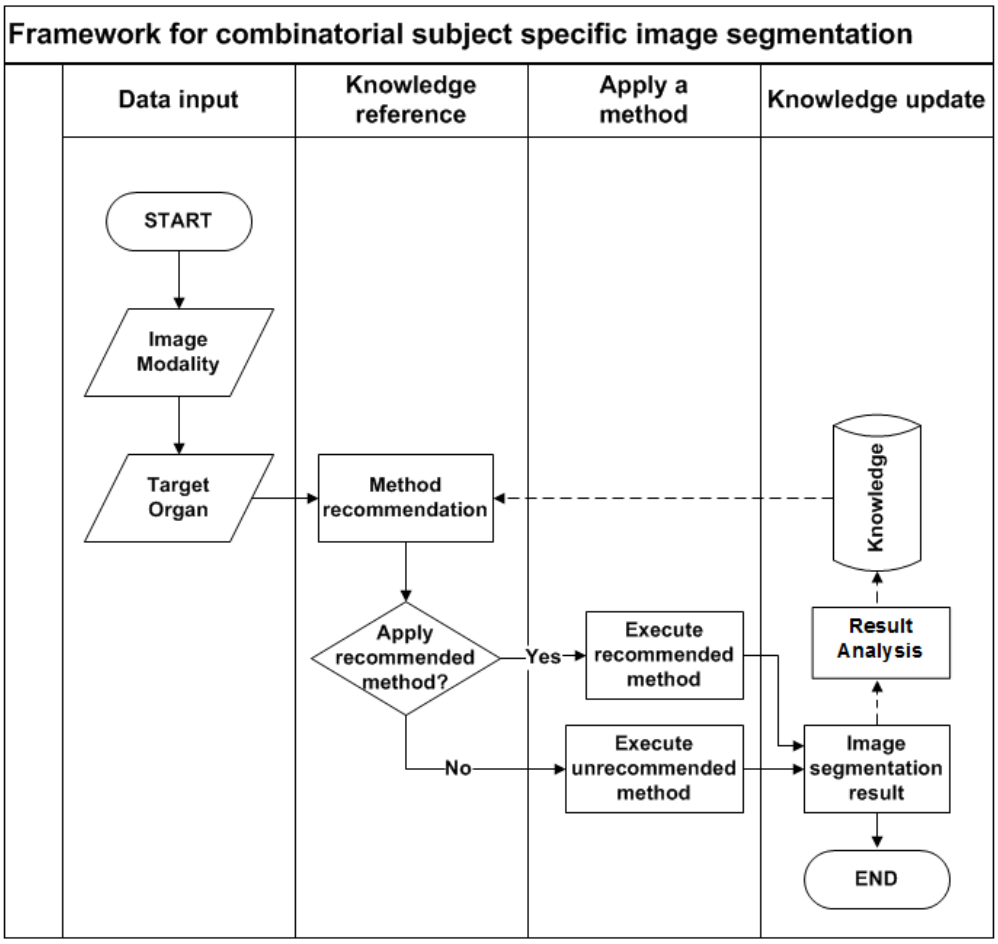

Figure 3.2: Proposed framework.

3.3 System Modeling

Each element in the system contains a set of possible words. A particular word can be associated with a single node in a graph (Figure 3.3). The third

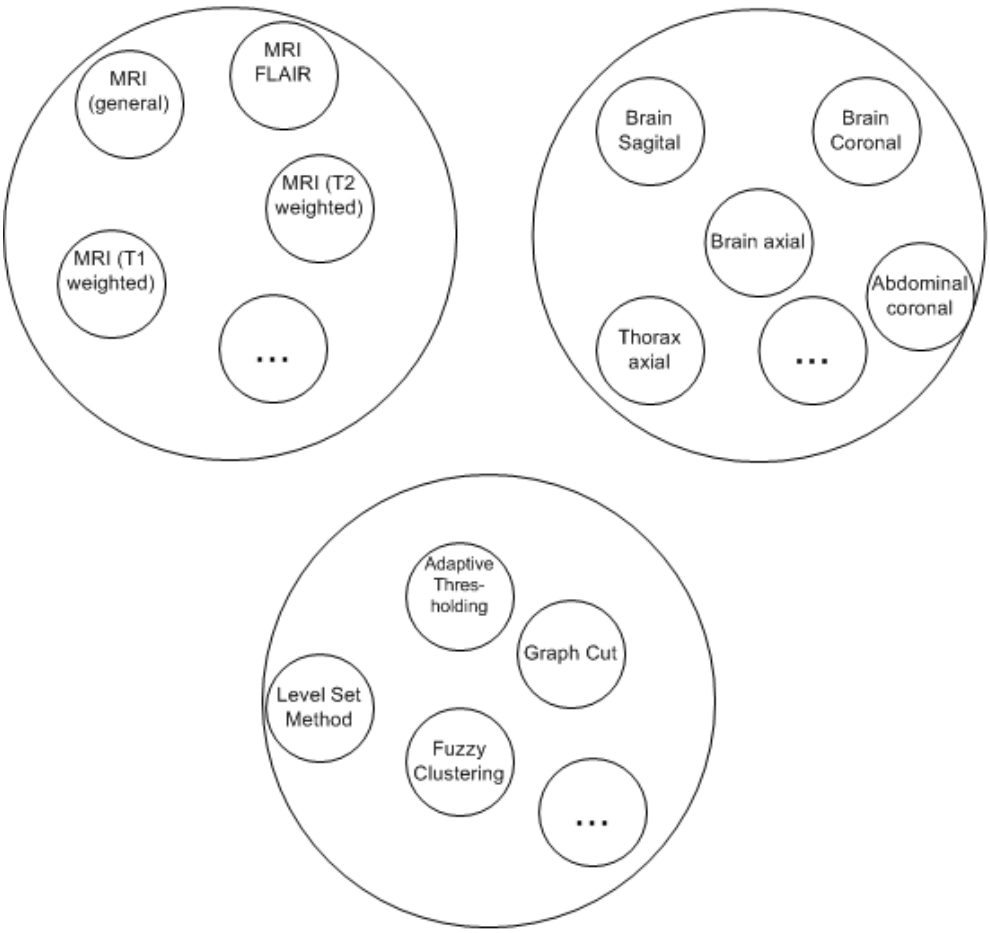

Figure 3.3: Three basic elements of the model.

element, i.e., the method to be used for segmentation, can be extended by applying it more than once and each method can be associated with an independent node.

Let $G(V, E)$ be a graph where V and E represent the set vertices and

edges. Let sub graph G_i represent the element of the system with properties

$$\bigcup_{i=1}^{n} G_i = G \tag{3.1}$$

$$\bigcap_{i=1}^{n} G_i = \emptyset \tag{3.2}$$

The first property ensures that the element is independent of others and the second property ensures that all elements are part of the system with a method applied a maximum of $n-2$ times. Letting $g_i \in G_i$ be the possible value of sub graph G_i, we can simplify the representation as an n-dimensional vector $g = (g_1, ..., g_n)^T$. Our goal is to find g such that the result of the segmentation has minimum error, which can be expressed as:

$$\arg\min_{g} \mathrm{Err}(g). \tag{3.3}$$

The final result should be evaluated by comparison with the ground truth. There are some ways to measure the accuracy as described in Section 2.5.

3.4 Element Design

Implementing the model above requires many algorithms for image segmentation from the basic algorithm to the sophisticated one. The problem that may be faced is the connection between one element and the other which leads to the second work, that is how to connect the elements which happens when more than one segmentation method is applied.

In each method discussed in the literature review, we have to adjust

the algorithm such that it can work together with other algorithms which means that the output of one element may be the input for another element as shown in Figure 3.4.

Formally, we have

$$F(\mathbf{g}) = f_n(g) \circ f_{n-1}(g) \circ ...f_1(g). \tag{3.4}$$

where F is the composite, f_i is a function representing an element. A difficulty in connecting the elements is: setting the range of the previous function, R, so that it matches with the input range of the next function, D,

$$\forall(f_{i-1}, f_i), R_{f_{i-1}} = D_{f_i}. \tag{3.5}$$

3.5 Segmentation Methods

The proposed framework uses segmentation methods as its basic engine. All segmentation methods will have the same input, which is a subject-specific image. Some sub-tasks related to this work are discussed below.

1. Implementing segmentation methods on various data sets

   Various segmentation methods are required in the development of the proposed framework. Some methods in the literature review are implemented. Various organ or tissue datasets from National University Hospital are used to test the proposed method.

2. Connecting two or more segmentation methods

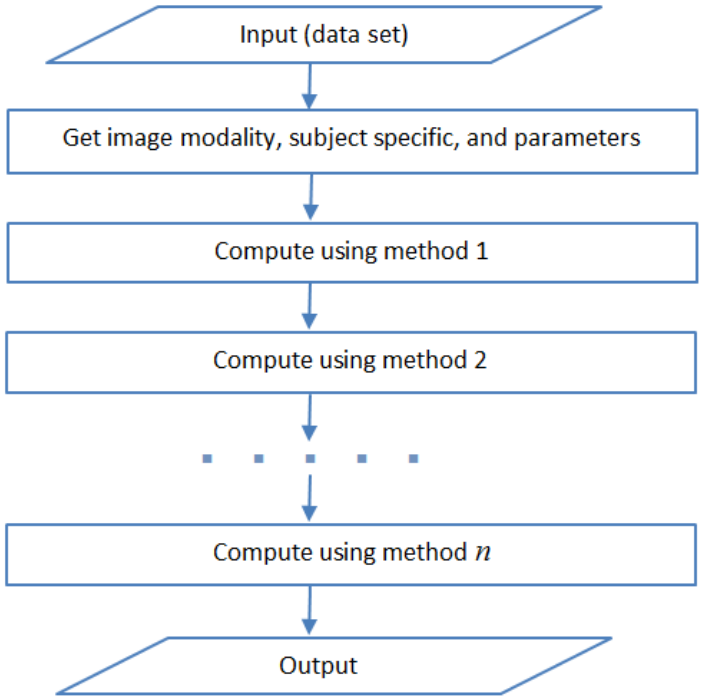

(a) Sequence of process.

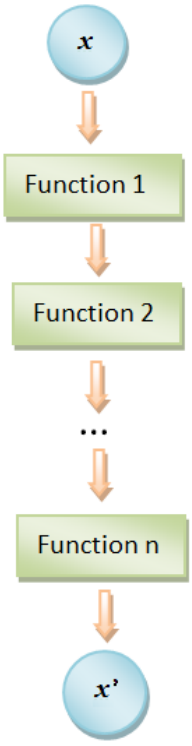

(b) Sequence of function.

Figure 3.4: Sequence of process and function.

This problem may be stated as follows: given as a set of methods, how do we create a path based on this set? Let the number of methods be n and for each defined path, and there is no repeated method. We can create a combinatorial solution path containing at least one method and at most n methods. The used methods indicate the length of a solution path, ℓ, and the total number of possible ways to create a path is

$$\sum_{\ell=1}^{n} \mathrm{P}(n, \ell) \tag{3.6}$$

where $\mathrm{P}(n, \ell)$ is the ℓ permutation of n.

The total number of possible paths rises exponentially with a factor n. However, there is a chance to reduce the number of paths by considering the following cases:

(a) in several references, the number of methods is usually not more than four, as in [88, 90, 16]. Then, the number of possible paths would be

$$\sum_{\ell=1}^{4} \mathrm{P}(n, \ell), n \geq 4. \tag{3.7}$$

This equation significantly reduces the number of possible paths for $n > 4$.

(b) Each method is not used more than once. A method that is applied before will not appear anymore in the next path. Hence, the number of methods is decreased by one for the next node in a path. The possible paths are shown in Figure 3.5. For convenience of illustration, we choose $\ell = 4$.

(c) Some methods usually appear before the others. For instance

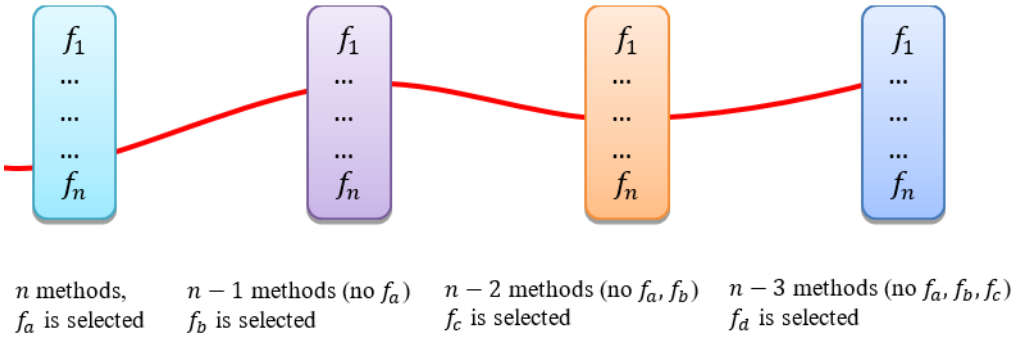

Figure 3.5: Path construction for $\ell = 4$.

thresholding is utilized to obtain an initial result before a more complex segmentation algorithm is applied.

(d) Some methods cannot be incorporated into a path. For example, the level set method and graph cut cannot be combined because the output of one method cannot be an input of another.

(e) For a certain method, some parameters need to be defined first before applying to the algorithm. During trials, the parameters and the performance are recorded. By recording all the trials, the most appropriate parameters can be identified through the image attributes (the modality and the organ/tissue).

3.6 Path Finding

The paths discussed above are the possible paths. Since our goal is not only to create paths but also to obtain the best performance, the problem of finding the path with the highest accuracy can be seen as an optimization

problem as shown in Equation (3.3). However, this path is typically different compared to the common path from a graph where every edge or node may have a value. Let an image I have possible paths as described in Figure 3.6. The path performance cannot be determined iteratively based on the

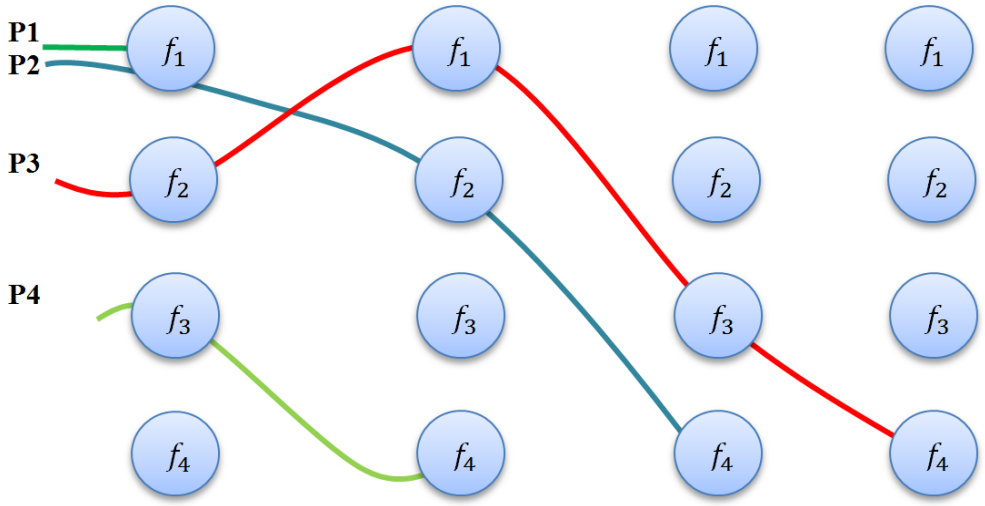

Figure 3.6: Some paths, indicated with colored line.

visited node. Each path has a performance value and can only be computed at the end of the path. It means the performance of $P1, P2, P3$ and $P4$ is computed after visiting f_1, f_4, f_4, and f_4 consecutively.

During training, image I has various performances depending on the path, namely $\eta(P1)$, $\eta(P2)$, $\eta(P3)$, and $\eta(P4)$. All trials are recorded and distinguished by time. The best performance is chosen among the various paths. Assume that the best performance is $\eta(P4)$. Next, if there is a new image which has identical attributes (organ/tissue and modality) with I, the path $P4$ is recommended including its parameters for each method. Otherwise, we have to find the most similar image before cloning the path.

Computing image similarity is a challenging task. Existing methods such as using entropy introduced by Wachinger and Navab [91] is totally

a content based method. There is no way to semantically measure the similarity from a similar imaging modality, for example MRI TI weighted and T2 weighted. An alternative approach is to utilize the content based method which is widely used and easy to measure.

In the reinforcement learning approach [64], the trials for new paths can be associated with the exploration. Initially, when no knowledge is available, the trials may be done intensively. For a particular image with an imaging modality and a specific organ/tissue, segmenting using various methods and their combinations can be applied randomly. Each method is used independently and evaluated by its performance, e.g., its accuracy.

When the system refers to the available knowledge in the database to select a segmentation method which generates the highest rewards, this procedure is known as exploitation. Balancing the trade-off between exploitation and exploration is important. To avoid a large number of combinations, some rules to select the next methods are available as described in Section 3.5. Moreover, each method generates errors which may be accumulated along the path. Therefore, it is necessary to choose only a portion of the best results for expanding the paths through a threshold, e.g., a percentage of best methods or those with a particular accuracy level.

3.7 Implementation

The implementation of the proposed framework requires many algorithms as the component of composite functions. In this thesis, we restrict the combinations to two popular approaches; i.e., classification algorithms and

active contour models using the level set methods.

We first propose a framework for combining standard classification algorithms with the edge-based active contour model. The classifiers are utilized to generate good initializations. Subsequently, more complicated combinations are investigated.

With the gradient magnitude and class probability from classification algorithms, we propose robust edge-stop functions and introduce them into our combinational approach. This combination of algorithms can handle medical images with poorly defined boundaries, particularly for the brain and liver tumor as well as the renal cyst images.

We also propose enhancements to the conventional region-based active contour model. Instead of using the original image, a map of class probability scores from a classification algorithm is employed. Regularization functions are introduced. This method can handle medical images with significant intensity inhomogeneity.

Chapter 4

Active Contour with Initialization from Classification Algorithms

4.1 Introduction

The use of energy minimization in image segmentation has been intensively studied, starting from the snake model [6]. Among energy minimization approaches, the level set method (LSM) has received much attention and is used to minimize an energy functional when segmenting an object [8, 9, 10, 69].

Generally, image segmentation models using LSM can be classified as edge-based models or region-based models [11, 12, 13]. The former utilizes edge information [10] while the latter employs a region descriptor to control the displacement of the active contour [76, 15]. Edge-based active contour models are popular and powerful methods due to their ability to handle poorly defined boundaries [69, 14]. However, one of the major drawbacks of the model is that the initial contour should be close enough to the true boundary to avoid a local minimum [92]. While the active contour segments

an image by evolving an initial curve, machine learning (ML) segmentation algorithms utilize training data to segment a region of interest on the test data. ML algorithms are powerful in identifying complex patterns automatically and allowing radiologists to analyze medical images [93].

An integration of ML algorithms with active contour models is an alternative approach to obtain accurate segmentation results, particularly on various types of medical images. Integrated methods have become popular since they can incorporate the advantages of each component method. ML algorithms can be utilized as an intermediate step to improve a simple user initialization by generating a rough segmentation. Subsequently, the active contour evolves the rough segmentation boundary to obtain the final segmentation.

A number of studies have been reported in which only machine learning is used for segmenting medical images. The k-nearest neighbors (k-NN) was utilized by Martijin et al. [19] to segment white matter lesion and by Kalid et al. [94] to segment brain abnormalities. The Bayesian classifier was used by Lee et al. [95] as a part of their study to segment a brain. The artificial neural network (ANN) was used by Wang et al. to segment cDNA microarray [96] and by Selver et.al. to segment abdominal organs [97]. The fuzzy c-means algorithm was employed by Hasan et al. [98] to segment carotid artery ultrasound images and by Ji et al. [99] to segment the brain. Shanmugam and Banu [100] utilized the extreme learning machine (ELM) algorithm to segment retinal blood vessels. Zhang and Lu [101] combined the ELM and the discriminative random fields to segment human knee cartilage from multi-contrast MR images. Cordeiro et al. [102] applied the ELM

to segment mammography images. In our previous work, we also utilized the ELM to segment vocal cord images [16]. Our preliminary experiments showed that the ELM outperforms the edge-based active contour model using LSM.

The random forest (RF) is also a popular ML algorithm that is well known for its ensemble learning. It was used by Ghose et al. [103] to segment prostate images, Lempitsky et al. [104] to delineate of myocardium in three-dimensional (3D) echocardiography, Cuingnet et al. [105] to segment kidneys, and Azar et al. [106] to diagnose lymph diseases.

A number of studies that utilized both ML algorithms and the LSM have been reported. Wang and Pan [107] incorporated local correntropy-based k-means (LCK) clustering into the region-based level set segmentation framework and tested their proposed method on images with different organs/tissues (brain, retina blood vessels) and acquisition techniques. They utilized LCK to update the level set function. Different from their method, we let a machine learning algorithm fully complete the rough segmentation and utilize its result as the initial contour for the LSM. This idea is also different from Olivier et al.'s method [108] where supervised binary classifiers are used to control the speed function of the active contour.

Bai et al. [109] used mean shift clustering and the region-scalable fitting (RSF)-level set method. Li et al. [110] introduced a combination of the support vector machine (SVM) and level set. They took the advantages of both hierarchical and coupled level sets. Starting with SVM and hierarchical level set segmentation, an improved initial curve placement for coupled level sets is obtained. Lan et al. [111] combined contextual constraint neural

networks (CCNN) and a level set evolution to segment femur and patella images. Li et al. [88] integrated the spatial fuzzy clustering with the level set method for medical image segmentation. Huang et al. [59, 112] used the ELM and the LSM to detect and segment tumor liver images. These studies used ML and the LSM; however, there is no study that discusses the integration of various ML algorithms with the LSM and compares their performances in an image database. Furthermore, no study is found in the literature for integration of the k-NN, the RF, and the Bayesian classifier (NBC) with the edge-based active contour model using the LSM.

4.2 Proposed Framework

Our framework comprises two main stages for segmenting images (Figure 4.1). Firstly, we apply a selected ML algorithm to classify pixels as background or foreground. Secondly, we apply results from the first stage to the edge-based active contour model using the LSM.

In the pre-processing step, the images are normalized to [0,255]. Subsequently, the images are ready to be segmented using a selected ML algorithm. Segmentation using ML algorithms comprises the following steps.

4.2.1 Initialization

From the pre-processing output, three images are selected randomly for data training: from the beginning, in the middle, and the end of a dataset. Subsequently, the images are marked using two colors, i.e, red and green

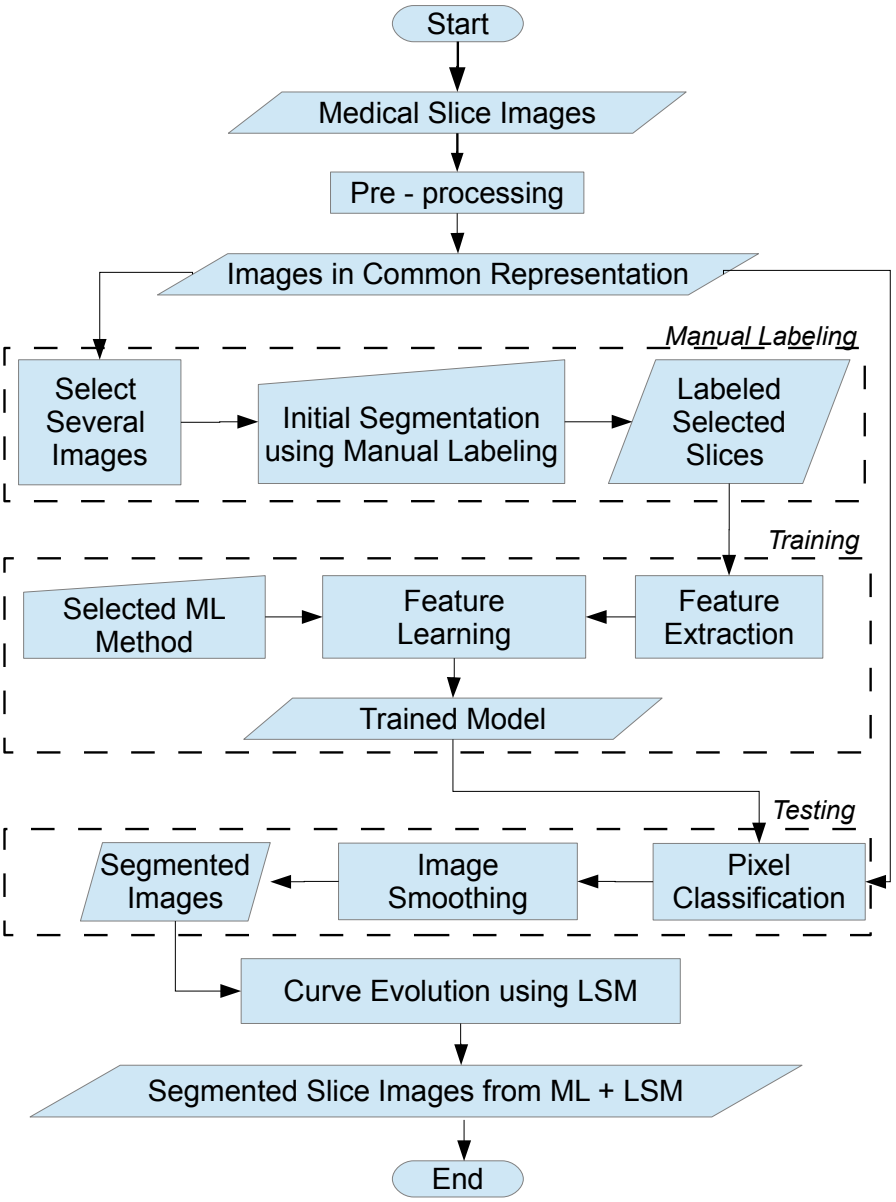

Figure 4.1: Flowchart for the proposed framework

which indicate foreground and background, respectively. An example of initialization can be seen in Figure 4.2(b).

4.2.2 Training

The ML algorithm requires a feature vector which determines the success of classification and regression. For a fair comparison of the integration of ML algorithms with the LSM, we use the same feature vectors for all datasets. The slices containing marked regions in the previous step are utilized to build a model which corresponds to a particular ML algorithm.

Since we do not intend to design sophisticated feature vectors for a specific segmentation problem, a simple feature vector containing an image patch of size 3×3 is used for all the experiments.

4.2.3 Testing

Since only the selected images have initializations, the remaining images will utilize the slices containing marked regions for training purpose. The function f in the previous step is utilized to classify pixels in the target images. After applying an ML algorithm, rough segmented images are obtained. Usually, the images contain a number of misclassified pixels and appear as noisy pixels which can be seen in Figure 4.2(c). Further smoothing can be done via morphological operators to reduce noise, i.e., erosion and dilation. The result of the first can be used as the initial contour for curve evolution using the LSM while that of the second is considered as the segmentation result using a particular ML algorithm (see Figure 4.2(d)).

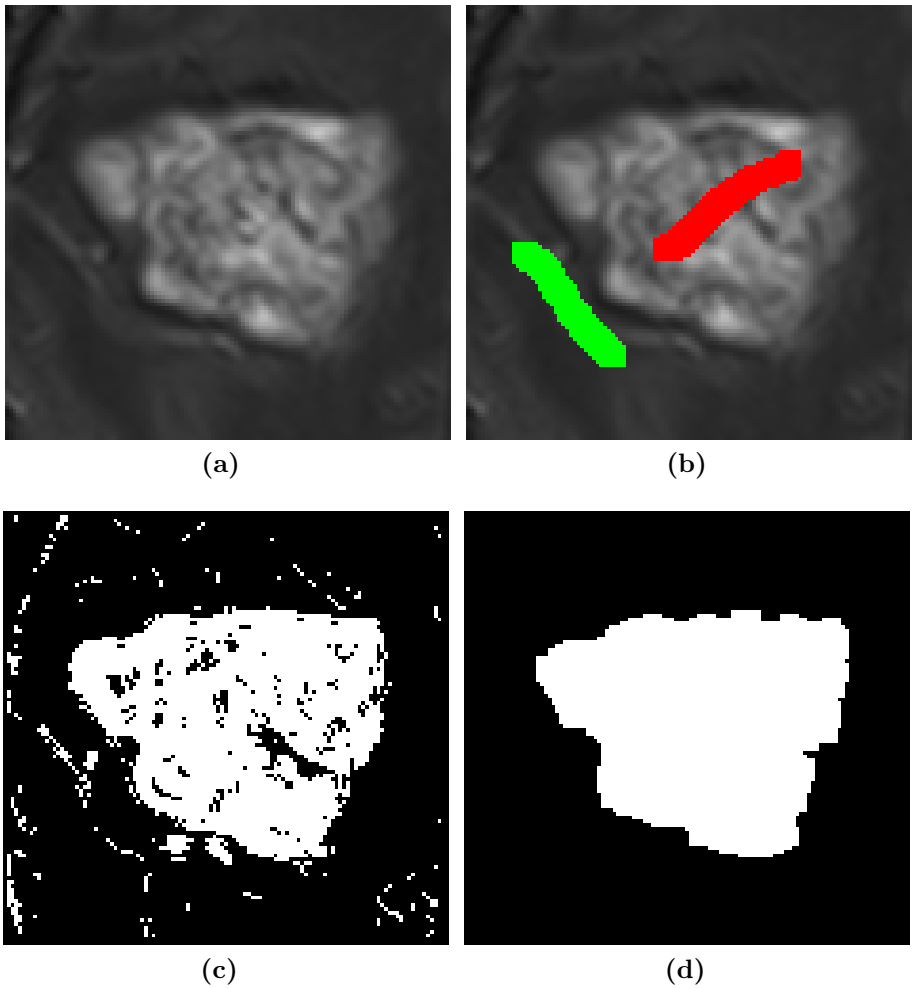

Figure 4.2: An example of: (a) an original image, (b) initializations, (c) a binary classification result using NBC, (d) a segmentation result after applying a morphological operator.

4.3 Results and Discussions

We apply our framework in Section 4.2 to medical images using six ML algorithms and the edge-based active contour model using the DRLSE. The experiments as well as the results are described in this section.

4.3.1 Experimental Setup

The proposed approach is validated on three brain and three liver tumor datasets from different patients. The liver datasets are computed tomography (CT) images while the brain datasets are magnetic resonance (MR) images. The resolution for all images are 512×512. The number of slices for each dataset are 14, 26, and 56 for the brain and 10, 8, and 8 for the liver. For further discussion, the proposed framework is also validated on three ultrasound (US) images containing renal cysts from different patients. Different from CT and MR images, the US images comprise only a single image for each patient. The resolution of the US images is 450×600 pixels. All the datasets are provided by our clinical collaborators.

We conduct experiments using a computer with CPU Intel Core i7 3820, 3.60 GHz and memory 32 GB, starting with pre-processing followed by an initialization and a learning step. The six ML algorithms described in Section 2.2 are utilized. The ML parameter values are determined carefully based on preliminary experiments. They are iteratively adjusted until performance is optimal. The optimal parameter values are given below.

1. k-NN : The number of neighbors, k, is set to 3 and the Euclidean

distance is used.

2. SVM: The input data are centered at their mean and scaled to have unit standard deviation. The kernel is the Gaussian radial basis function with $\sigma = 1$. Sequential minimal optimization is used to find the hyperplane. The parameter for the soft margin cost function is set as C=1.

3. NBC: The normal (Gaussian) distribution is used to construct the model. The parameters μ and σ are estimated using maximum likelihood.

4. RF: The number of trees is set to 50. The number of predictors to select at random for each decision split is set to 3 which is the square root of the number of all predictors.

5. ELM: We normalize the feature values to [0,1]. The number of hidden neurons assigned is 25 and the activation function is a sigmoidal function.

6. ANN: The network comprises three layers, i.e., input, hidden, and output layers where the number of neurons are 9, 10, and 1, respectively. The Levenberg-Marquardt algorithm is used for the training.

For the active contour, the implementation of the DRLSE in the form of edge-based active contour model is used. Similar to the machine learning algorithms, all parameters are carefully chosen based on preliminary experiments. They are iteratively adjusted until performance is optimal. The parameters are: $\eta = 0.04, \lambda = 5.0, \gamma = 1.5, \epsilon = 1.5$, and $\sigma = 1.5$. We record the segmentation accuracy for quantitative measurement. Two

popular metrics are used, i.e., the Jaccard index (JI) and the similarity index (SI). For comparison purposes, the accuracy of the results from the ML algorithm is also recorded.

4.3.2 Results

Experimental results for further analysis containing the Jaccard and the Dice similarity index can be seen in Tables 4.1, 4.2 and 4.3.

Table 4.1: Segmentation performance for the liver tumor datasets (CT images)

#	ML	Using ML only		Using ML + AC		Δ means	
		JI	SI	JI	SI	JI	SI
1	k-NN	0.86±0.11	0.92±0.07	0.88±0.10	0.93±0.06	0.02	0.01
2	SVM	0.86±0.08	0.92±0.05	0.88±0.10	0.93±0.07	0.02	0.01
3	NBC	0.84±0.08	0.91±0.05	0.86±0.09	0.92±0.06	0.02	0.01
4	RF	0.84±0.11	0.91±0.07	0.89±0.09	0.94±0.05	0.05	0.03
5	ELM	0.86±0.10	0.92±0.07	0.87±0.10	0.93±0.06	0.01	0.01
6	ANN	0.83±0.19	0.89±0.19	0.85±0.19	0.90±0.19	0.02	0.01

4.3.3 Discussion

Evaluation for using AC only is not applicable because hand initialization is only applied to three slices among a dataset. Manual initialization for each slice is tedious task and not practical for clinical use. Based on the

Table 4.2: Segmentation performance for the brain tumor datasets (MR images)

#	ML	Using ML only		Using ML + AC		Δ means	
		JI	SI	JI	SI	JI	SI
1	k-NN	0.85±0.12	0.91±0.10	0.86±0.12	0.92±0.10	0.01	0.01
2	SVM	0.84±0.17	0.90±0.16	0.85±0.17	0.91±0.16	0.01	0.01
3	NBC	0.70±0.26	0.79±0.25	0.73±0.25	0.81±0.25	0.03	0.02
4	RF	0.81±0.14	0.88±0.12	0.85±0.13	0.91±0.11	0.04	0.03
5	ELM	0.78±0.25	0.85±0.26	0.80±0.25	0.86±0.26	0.02	0.01
6	ANN	0.78±0.23	0.85±0.22	0.80±0.23	0.86±0.22	0.02	0.01

Table 4.3: Segmentation performance for the renal cyst datasets (US images)

#	ML	Using ML only		Using ML + AC		Δ means	
		JI	SI	JI	SI	JI	SI
1	k-NN	0.79±0.03	0.88±0.02	0.84±0.02	0.91±0.01	0.05	0.03
2	SVM	0.80±0.06	0.89±0.04	0.85±0.01	0.92±0.01	0.05	0.03
3	NBC	0.52±0.45	0.58±0.50	0.56±0.49	0.61±0.53	0.04	0.03
4	RF	0.76±0.04	0.86±0.03	0.83±0.04	0.91±0.02	0.07	0.05
5	ELM	0.64±0.17	0.77±0.14	0.69±0.24	0.80±0.18	0.05	0.03
6	ANN	0.77±0.06	0.87±0.04	0.84±0.01	0.92±0.01	0.07	0.05

initial marks comprising foreground and background regions, all pixels in each image from a single dataset can be classified. After post processing, i.e., applying a morphological operator, segmentations using ML algorithms are obtained. They are presented in Table 4.1 for the liver tumor, Table 4.2 for the brain tumor, and Table 4.3 for the renal cysts.

As can be seen in Table 4.1, using only machine learning algorithms, JI and SI are similar. Applying the edge-based active contour to those results improve the accuracy by between 0.01 to 0.05 for JI and 0.01 to 0.03 for SI. Similar improvements are also true of the brain tumor images (Table 4.2). Even though the accuracy using only machine learning algorithms has a large range, it consistently increases by between 0.01 to 0.04 for JI and 0.01 to 0.03 for SI. The significant improvements appear in Table 4.3. JI increases by between 0.04 to 0.07 while SI by 0.03 to 0.05. Except for the NBC, the accuracy of all algorithms are similar for both JI and SI. Moreover, the higher the JI or SI from using only machine learning algorithms is, the higher the JI or SI from using machine learning algorithms and the active contour model will be.

In general, we can see from the tables that k-NN and SVM are sufficiently consistent to generate good results. In the liver tumor segmentation, even though those methods do not give the highest accuracy for ML+AC, their performance is just slightly less than the best accuracy. In the brain tumor segmentation, those methods outperform others with or without using the active contour. In contrast, NBC generates poor results. It achieves the lowest accuracy in segmenting all tumors and cysts, with or without the active contour. Examples of qualitative results for the the selected ML

algorithms are shown in Figures 4.3, 4.4, and 4.5. They show segmentation results using ML only compared with those using ML + AC. The ground truth, the segmentation results using ML only, and those using ML+AC are indicated by the solid green, red dashed, and blue dot lines, respectively. Note that the accuracy listed in Table 4.1 and Table 4.2 comes from the average accuracy of a dataset which comprises many slices.

Generally, applying the active contour on a segmentation result using an ML algorithm will improve accuracy but this is not always so. Figure 4.6 shows an example of this case where ambiguous pixels have resulted in wrong segmentation. In the vicinity of the boundary, some pixels are misclassified. The segmentation is generated using SVM (Figure 4.6 (a)) and SVM+AC (Figure 4.6 (b)). The misclassified pixels lead to the error in the final segmentation as shown in the figure. The accuracy of the slice using only SVM is 0.87 (JI) and 0.93 (SI) while using SVM+ AC is 0.83 (JI) and 0.90 (SI). This is a special case where applying the active contour decreases the accuracy. This problem can be solved easily by adding more strokes to indicate the foreground and background precisely. Another way is to set parameters for the active contour. However, in practice we retain the initializations from the three selected slices in the beginning and use general settings for the active contour. Furthermore, in most of cases, the accuracy increases although some pixels are misclassified.

Given that the performance of ML+AC methods analyzed above are similar, using other measures such as computational time and *ease-of-use* (i.e., limited use of parameter tuning) can be considered in the selection process. Table 4.4 shows the computation time for each observation. As

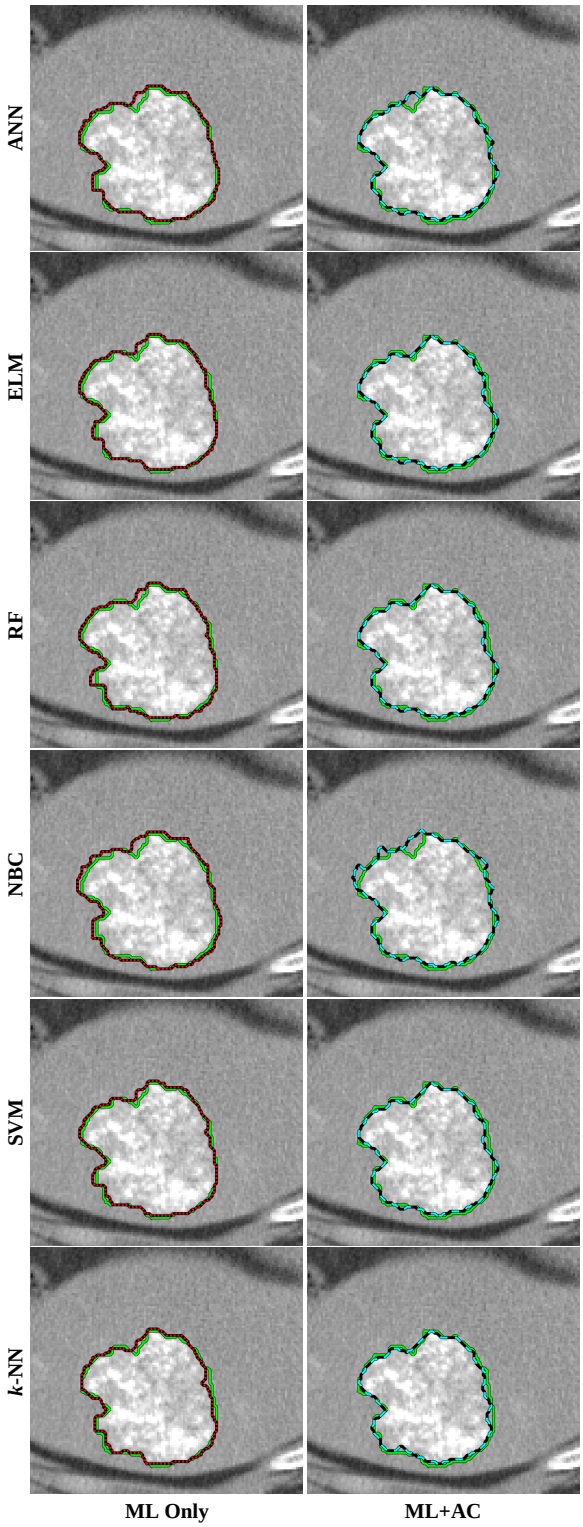

Figure 4.3: Segmentation results for the liver tumor.

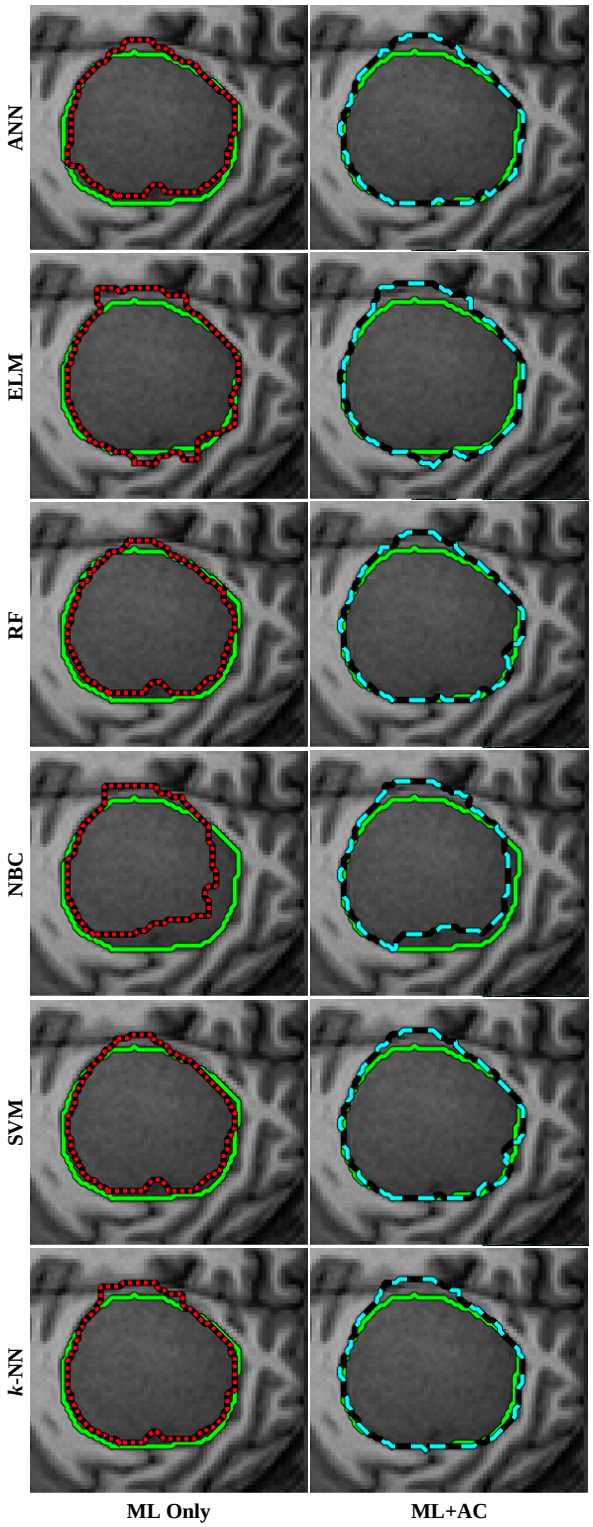

Figure 4.4: Segmentation results for the brain tumor.

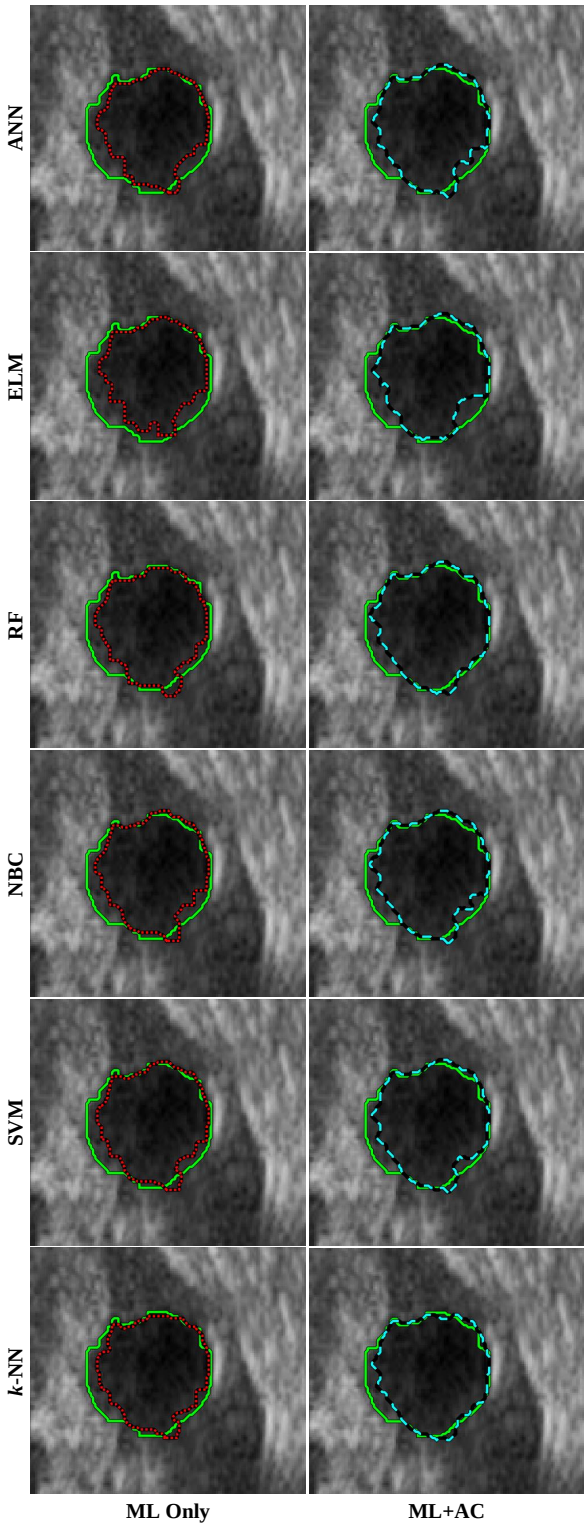

Figure 4.5: Segmentation results for the renal cyst.

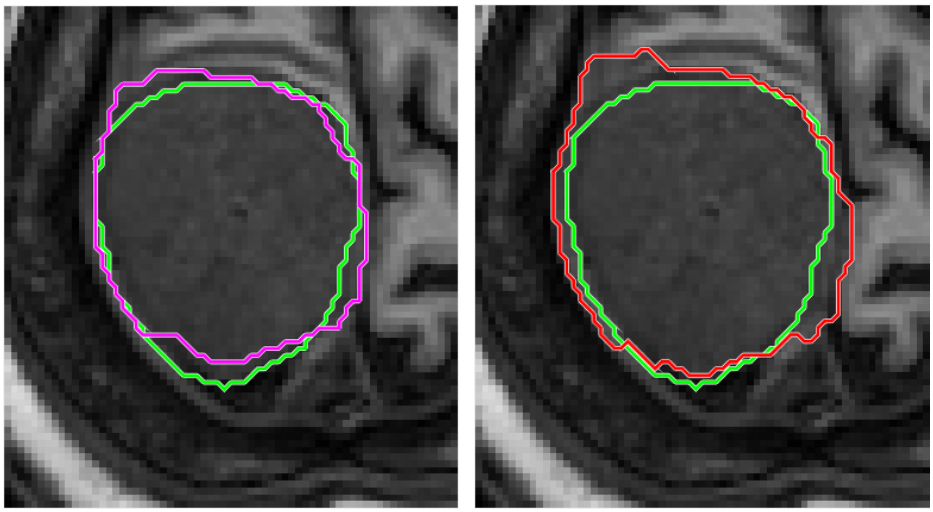

(a) (b)

Figure 4.6: Segmentation results using (a) only the SVM and (b) the SVM + AC. The green, magenta, and red line indicate the ground truth, the result using only the SVM, and the result using the SVM+ AC, respectively.

can be seen, k-NN generally demonstrates the most efficient to complete the segmentation tasks. It is worth to note that the number of images for each of the liver as well as brain tumor are hundreds while the renal cyst only three.

Based on the parameter setting, k-NN is intuitively easy to set. Given the nature of the algorithm, it only requires the number of neighbors (k) and the distance measurement (usually Euclidean distance). Since the accuracy is also high, this algorithm is reasonable to be the first choice for the integration.

Table 4.4: Computational time to complete the segmentation tasks

#	ML Algorithm	Liver Tumor*	Brain Tumor*	Renal Cyst*
1	k-NN	150.55	678.49	19.78
2	SVM	185.45	1,125.21	20.31
3	NBC	232.78	1,642.58	19.28
4	RF	253.98	2,034.09	22.12
5	ELM	291.49	2,495.43	17.80
6	ANN	373.95	3,170.17	25.78

* The unit is in seconds and the best result is highlighted with blue background.

4.4 Summary

The framework presents a new approach for multi-steps segmentation methods which is highly flexible. Different machine learning algorithms can be chosen and integrated with the edge-based active contour model using the LSM. We conducted experiments by applying the framework into the brain tumor, liver tumor, and renal cyst datasets. ML algorithms can generate good coarse initializations which are close enough to the true boundary. The final result is obtained by applying the edge-based active contour model, based on the coarse initialization.

Generally, the better the coarse initialization is, the better the final result will be. The edge-based active contour which is implemented using the LSM improves the accuracy of the final segmentation.

Since there is no one ML algorithm that outperforms all the others, it is important to choose an appropriate ML algorithm. Among the investigated machine learning algorithms, the integration of the k-nearest neighbors and support vector machines with the edge-based active contour generally gives more accurate results.

Chapter 5

Active Contour with Gradient and Class Probability

5.1 Introduction

We have integrated machine learning with the edge-based active contour model in Chapter 4. The segmentation results obtained from machine learning, which are close enough to the true boundaries, are utilized for the initial contours of the edge-based active contour. In this chapter, we integrate machine learning with the edge-based active contour more tightly by utilizing the probability scores from a classification algorithm to stop the contour evolution in edge-based active contour models.

Edge-based models are not sensitive to inhomogeneity of image intensities, i.e., the overlapping of the intensity ranges, but are sensitive to objects with poorly defined boundaries. In images where the intensities change gradually in the vicinity of a poorly defined boundary, the edge-stop function (ESF) fails to stop the contour [16].

To overcome the limitation of the traditional ESFs in edge-based active

contour models, we propose a framework to construct a group of robust ESFs that utilize probability scores instead of the predicted class labels from a classifier. Since the scores fall in $[0, 1]$, this task is similar to fuzzy segmentation. Unlike the methods of [113, 114], which rely only on class probability using Bayes' rule, our framework is more flexible since it utilizes the probability scores from any classifier. At the same time, we retain gradient information to terminate contour evolution when there are no fuzzy values due to distinct boundaries. These ideas differentiate our work from [115], which relies on fuzzy energy and is considered a region-based level set method.

5.2 Proposed Framework

Our new ESFs can be constructed from any classification algorithm and applied to any edge-based model using an LSM. The proposed framework is presented in Figure 5.1. In this chapter, two classification algorithms are investigated to construct ESFs, namely, k-NN and SVM.

Evaluation scores from classifiers generally fall in the range $[0, 1]$ or $(-\infty, +\infty)$. The scores of the k-NN classifier are of the first type and can be considered probability scores while those of the SVM are of the second. The latter can be converted to prior probability scores [116].

The traditional ESFs in Equation (2.32) have a drawback when applied to an image containing an object with poorly defined boundaries. The contour may fail to stop at the desired boundary because of the gradual change in gradient. The binary classification of an image into background

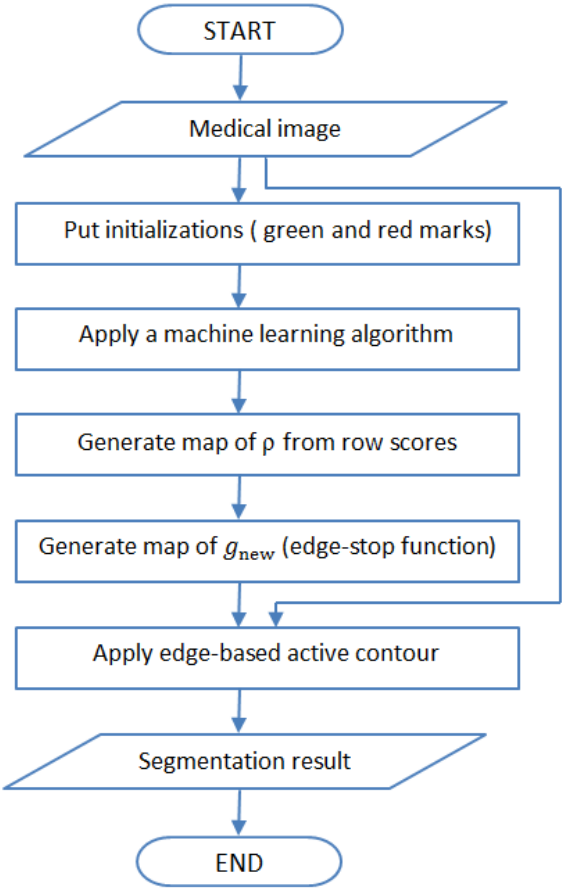

Figure 5.1: The proposed framework.

(class 0) and foreground (class 1) can be solved using a classifier. Instead of binary classification, we utilize a smooth transition from the probability scores to find the desired boundary. Probability scores which lie in the range of $[0, 1]$ can be obtained by applying a classification algorithm to all the pixels. In the vicinity of the object boundary, the scores change from 1 to 0 (or vice versa) through a smooth transition. The chance that a boundary exists is high when an ambiguous classification occurs, i.e., the probability score is 0.5. In terms of energy minimization, a score of 0.5 should generate the lowest energy. Furthermore, a membership of 0 or 1 should generate

high energy because the region is not the desired boundary. We use the fuzzy ESF $\rho(s) : [0, 1] \rightarrow [0, 1]$

$$\rho(s) = 4s^2 - 4s + 1 \tag{5.1}$$

where s is the probability score for the foreground. It is worth noting the properties of ρ in (5.1):

1. the domain as well as the range lie in $[0, 1]$,
2. it is monotonically decreasing in $[0, 0.5]$ and monotonically increasing in $[0.5, 1]$.
3. the following equations hold

$$\lim_{s \to 0} \rho(s) = 1, \tag{5.2}$$

$$\lim_{s \to 0.5} \rho(s) = 0, \tag{5.3}$$

$$\lim_{s \to 1} \rho(s) = 1. \tag{5.4}$$

Any other functions having similar characteristics also can be employed as $\rho(s)$, e.g.,

$$\rho(s) = \cos {}^{p}\pi s, 0 \leq s \leq 1, p = 2, 4, 6, ... \tag{5.5}$$

Subsequently, the fuzzy ESF is used to regularize function g in Equation (2.32) to obtain g_{new} which can be simply expressed by

$$g_{\text{new}} = g\rho. \tag{5.6}$$

A smoothing step, e.g., applying the Gaussian kernel, may be required for highly noisy images to prevent the contour from stopping prematurely. The fuzzy ESF, ρ, will force g_{new} to be close to 0 when ρ is very close to zero even though g is much higher than 0, i.e., when the image intensity drops gradually. Consequently, g_{new} will be close to 0 which will stop a contour at the desired boundary. Therefore, function g_{new} should be used instead of Equation (2.32) for objects with poorly defined boundaries.

5.3 Experimantal Setup

5.3.1 Data Set

To evaluate the effectiveness of the proposed framework, several medical images containing objects with poorly defined boundaries are tested. The images come from different patients. The medical images are computed tomography (CT) scans of liver tumor (3 images), magnetic resonance imaging (MRI) scans of brain tumor (5 images), and ultrasound (US) scans of renal cyst (3 images). The resolution for CT, MRI, and US are 512×512, 512×512, and 450×600 pixels, respectively. The ground truths of the images are drawn by an expert.

To segment an object, two marks are initially drawn to train the classifier (Figures 5.2(a) and 5.3(a)). The red mark indicates the foreground whose boundary is used to initialize the contour while the green mark denotes the background. The red mark boundary is used as the initial contour as well as training data for the classifier at the initial step.

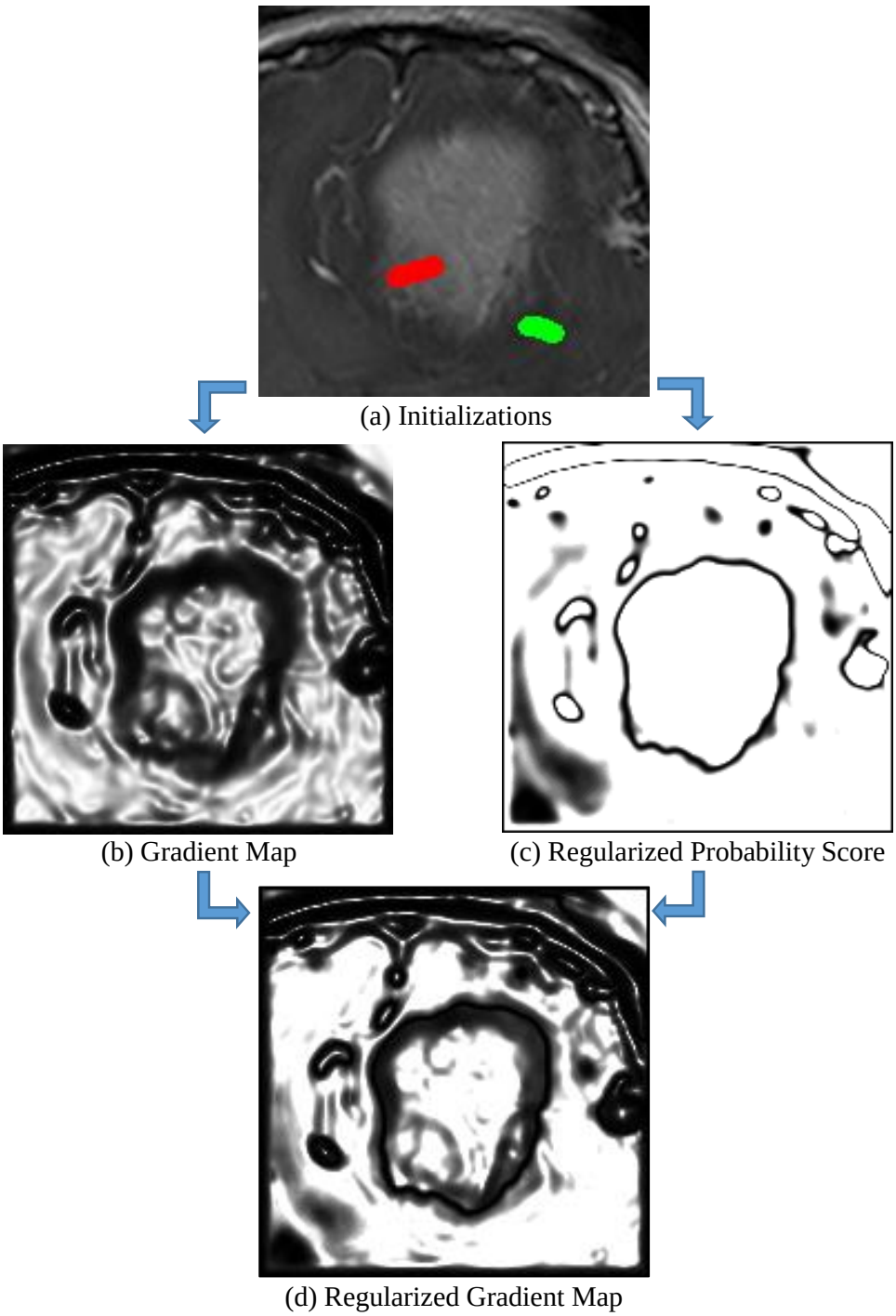

Figure 5.2: Gradient map, regularized probability score map, and their integration.

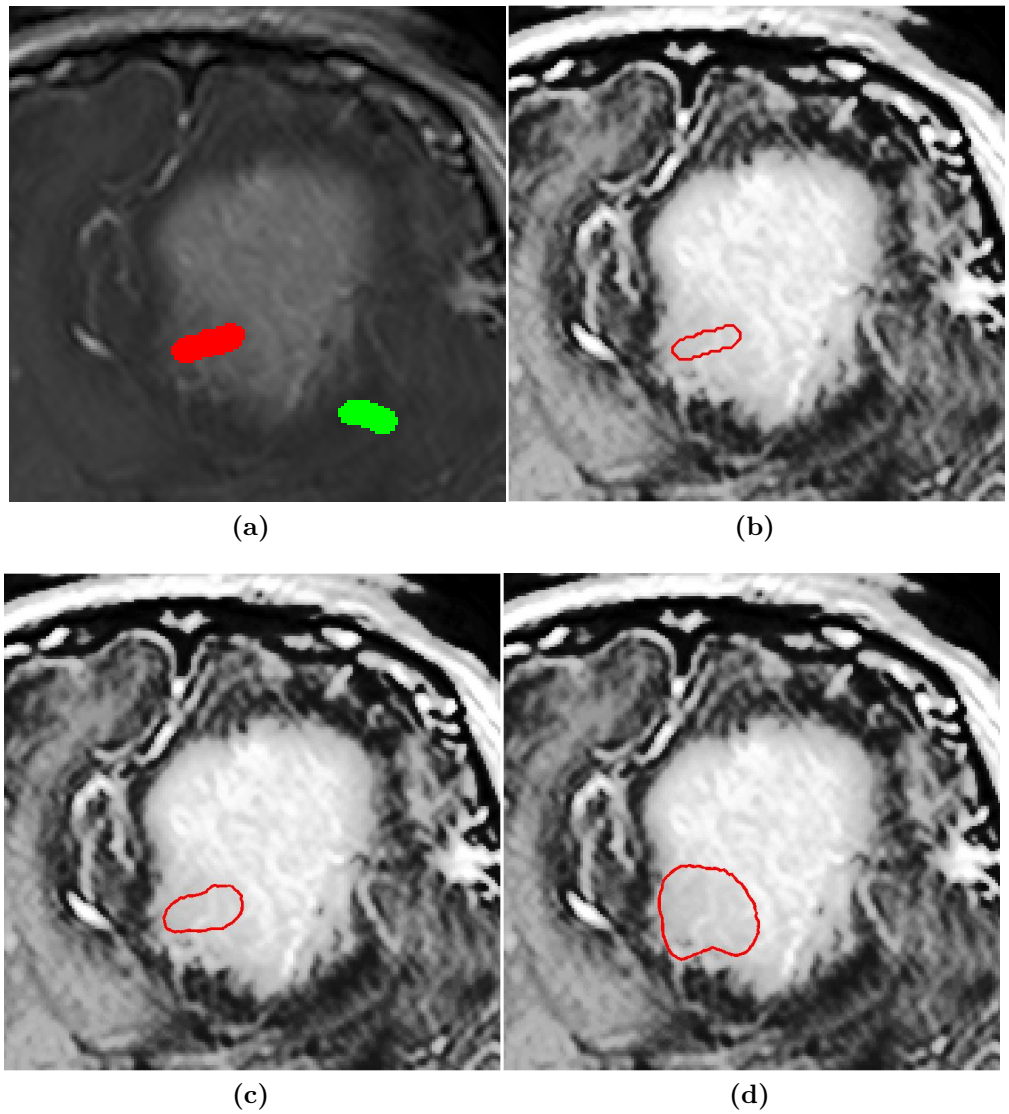

Figure 5.3: (a) User initialization containing red and green marks on the brain tumour image, (b) an initial contour is generated from the red-mark boundary, (c) the contour after 10 iterations, (d) the contour after 40 iterations. For convenience, images (b)−(d) are shown in contrast enhancement.

5.3.2 Parameter Setting and Quality Assessment

We implement the proposed ESFs in Matlab and utilize the DRLSE for the implementation of the edge-based active contour model with parameter values from Li et al. [74], unless otherwise stated. The default parameter values are $\mu = 0.04$, $\alpha = 1.5$, $\epsilon = 1.5$, and $\sigma = 2.5$. The value of λ is set to 3 for the liver tumor and 5 for the brain tumour. The number of neighbors, k, in the fuzzy k-NN algorithm is set to a large value to allow fuzziness in the vicinity of the boundaries. From our preliminary experiments, $k \geq 50$ generates good results (Figure 5.4 and Tables 5.1 and 5.2).

Table 5.1: Preliminary results for the JI on the value of k

No	**Images**	$k =$						
		5	20	35	50	65	80	95
1	Brain tumor (MRI)	0.84	0.85	0.86	0.87	0.88	0.89	0.89
2	Liver tumor (CT)	0.40	0.79	0.82	0.90	0.90	0.90	0.90
3	Renal cyst (US)	0.85	0.85	0.87	0.88	0.88	0.89	0.91

We use $k = 99$ for all the experiments to cover exactly one hundred different membership values and generate smooth transitions between the background and foreground. The kernel function in the SVM is linear with scale parameter = 1. A feature vector, generated from a 3×3 image patch, is used for all the experiments. Preliminary experiments show similar results with Equations (5.1) and (5.5). We use function ρ in Equation (5.1) without any intention to downplay the importance of Equation (5.5). We

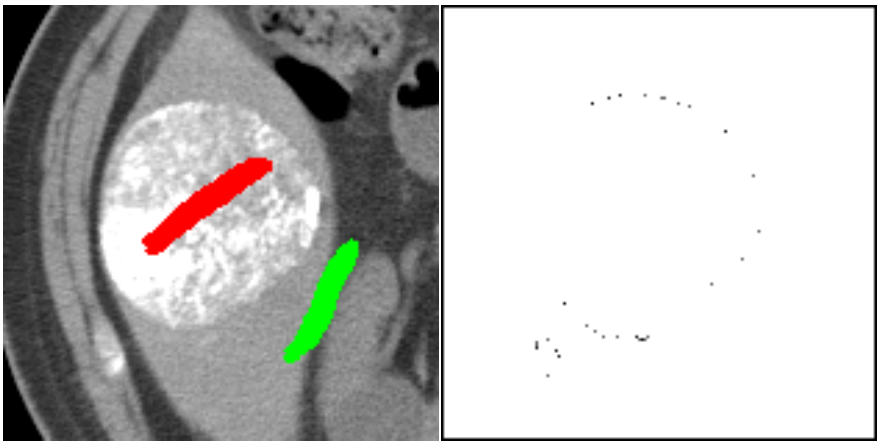

(a) user initializations

(b) $k = 5$

(c) $k = 15$

(d) $k = 25$

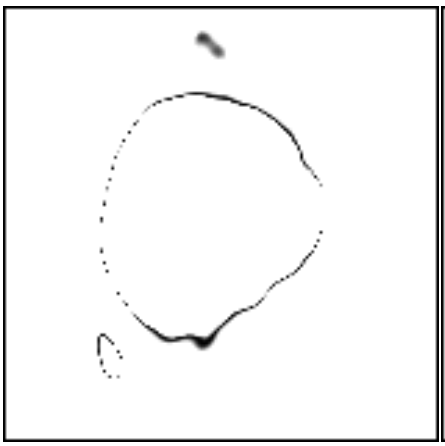

(e) $k = 45$

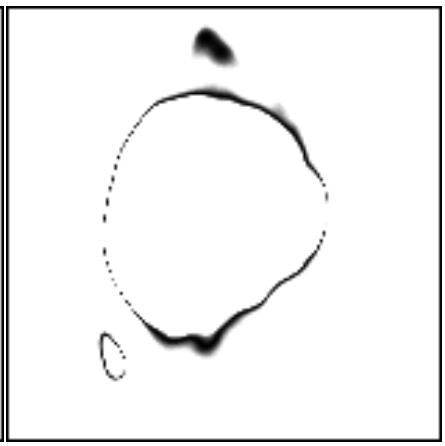

(f) $k = 75$

Figure 5.4: Maps of ρ using various k on a liver tumor image.

Table 5.2: Preliminary results for the SI on the value of k

No	Images	k =						
		5	20	35	50	65	80	95
1	Brain tumor (MRI)	0.91	0.92	0.93	0.93	0.94	0.94	0.94
2	Liver tumor (CT)	0.53	0.88	0.90	0.95	0.95	0.95	0.95
3	Renal cyst (US)	0.91	0.92	0.93	0.94	0.94	0.94	0.95

run the program on a PC with a 64-bit Windows 7 Enterprise, core i7-3820 3.60-GHz processor, and 32 GB RAM.

For comparison purposes, the images are also segmented using Chan-Vese's (C-V's) method [15] as well as Li et al.'s method with the traditional ESF [74]. For C-V's method, the parameters for each modality are carefully chosen. We iterate a range of values for a combination of the time step, the length term coefficient, and the foreground and the background weights to obtain a general setting [117, 118]. For Li et al.'s method, the parameters are identical with our method. The iteration is stopped when the result does not change for 5 consecutive iterations or a pre-defined maximum number of iterations is reached.

Two common quantitative measurements are used, i.e., the Jaccard index (JI) and the Dice coefficient which is also known as the similarity index (SI). These are defined in Equations (2.55) and (2.56).

5.3.3 How the Proposed Method Works

Maps of g can be used to visualize how our proposed ESFs work. A sample of a MR brain tumor image is used (Figure 5.2(a)). The traditional g map, which utilizes only gradient information, is generated based on Equation (2.32) and shown in Figure 5.2(b). At the same time, applying a classification algorithm, e.g., the SVM, to the image will produce the evaluation score of each pixel. Subsequently, the evaluation score is converted to a probability score. The fuzzy ESF (ρ) from Equation (5.1) is applied to the probability score and the resulting ρ map is shown in Figure 5.2(c). Pixels with a high likelihood to be background or foreground have higher ρ values and look brighter. Finally, the g_{new} map (Figure 5.2(d)) based on Equation (5.6) is used as the ESF of the edge-based active contour model. It is worth noting that using only ρ as the ESF does not make the contour converge at the desired boundary as shown in Figure 5.5.

5.4 Results and Discussions

Some of the segmentation results from our experiments using robust ESF (Equation 5.6) are shown in Figures 5.6, 5.7, and 5.8 while the quantitative results are presented in Tables 5.4 and 5.5. Table 5.3 lists the total of the running time for each modality and the time spent for training. Table 5.4 shows the corresponding accuracy for all the methods. The proposed method converges faster compared to Li et al.'s method and gives more accurate segmentations. It is well known that region-based active contour models and C-V's method do not perform well with inhomogeneous images.

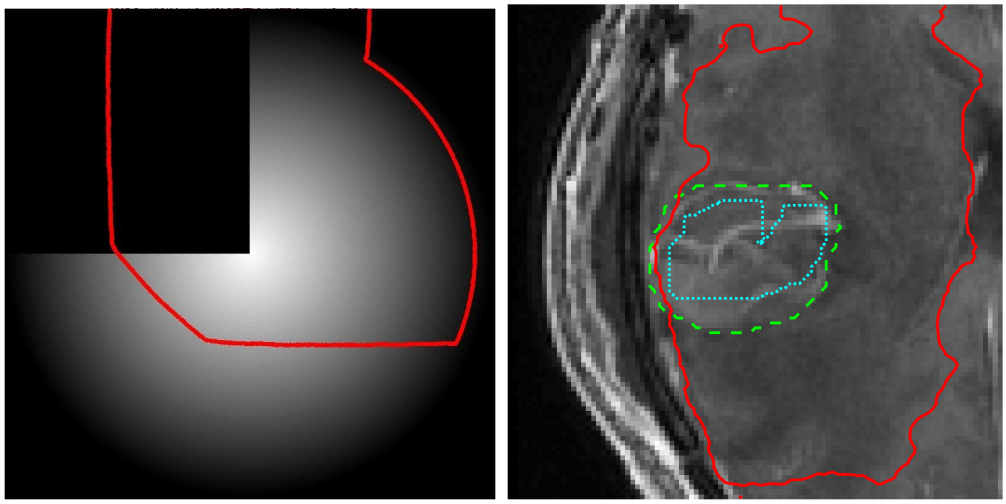

(a) Synthetic image **(b)** Brain tumor

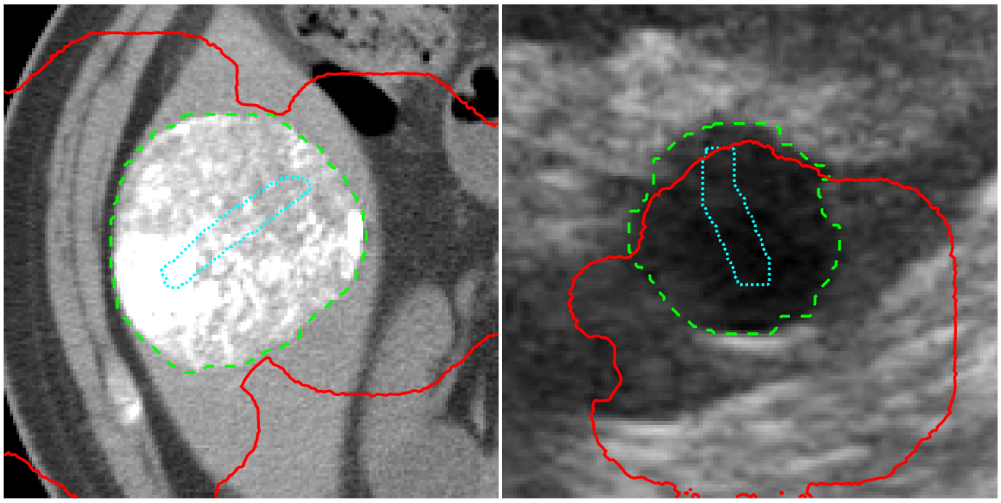

(c) Liver tumor **(d)** Renal cyst

Figure 5.5: Using only ρ as the stop function for various images does not work. Red solid lines denote the final segmentation, blue dotted lines the initialization contour, and green dashed lines the ground truth.

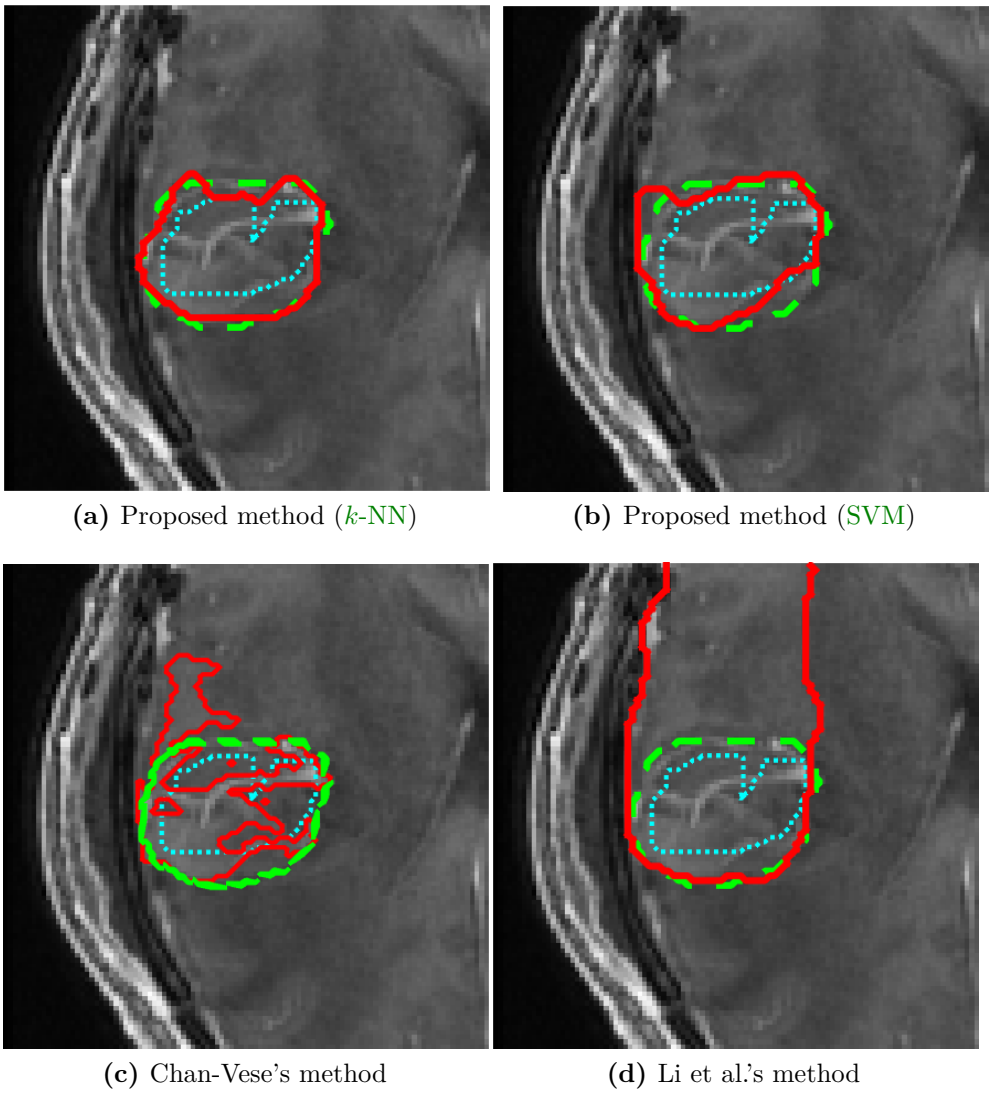

(a) Proposed method (k-NN)

(b) Proposed method (SVM)

(c) Chan-Vese's method

(d) Li et al.'s method

Figure 5.6: Segmentation results for the brain tumor using various methods

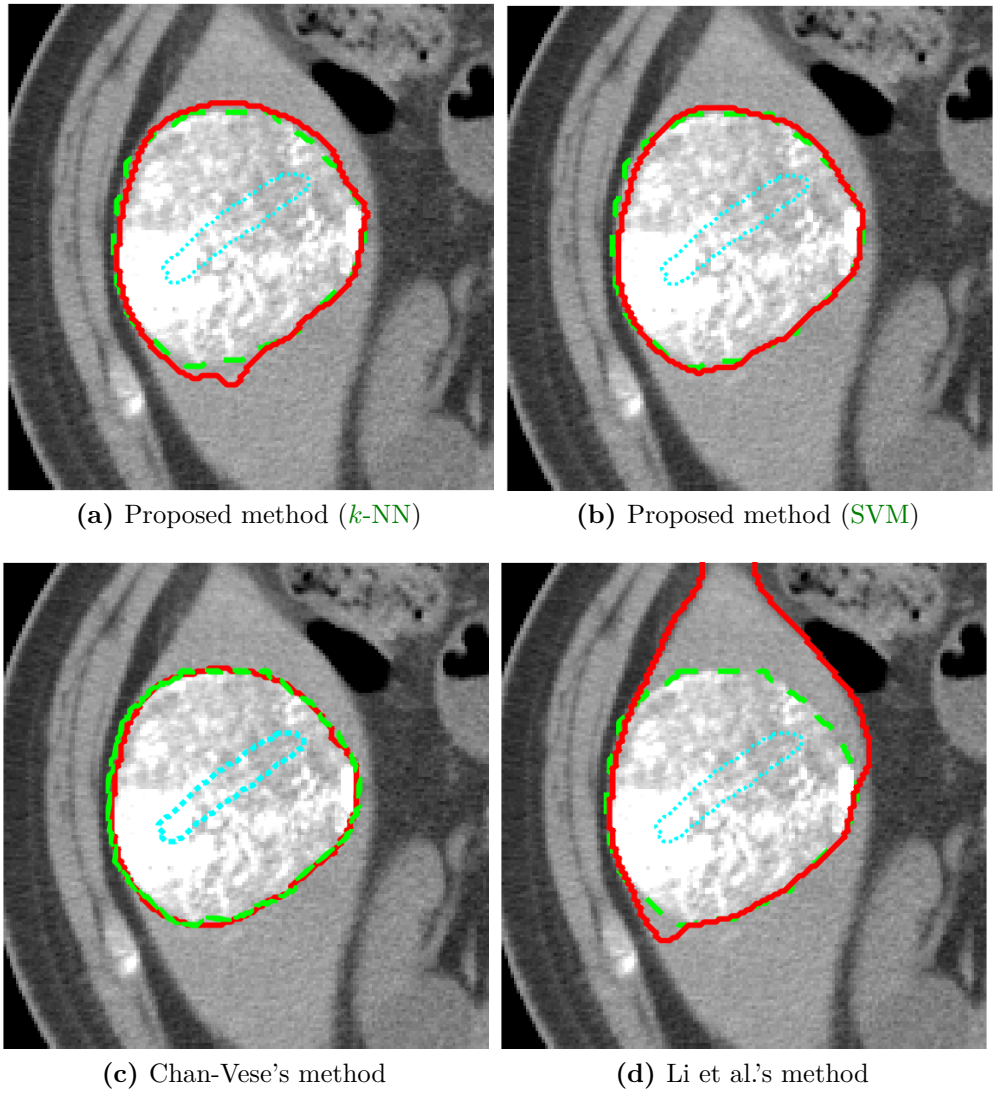

(a) Proposed method (k-NN)

(b) Proposed method (SVM)

(c) Chan-Vese's method

(d) Li et al.'s method

Figure 5.7: Segmentation results for the liver tumor using various methods

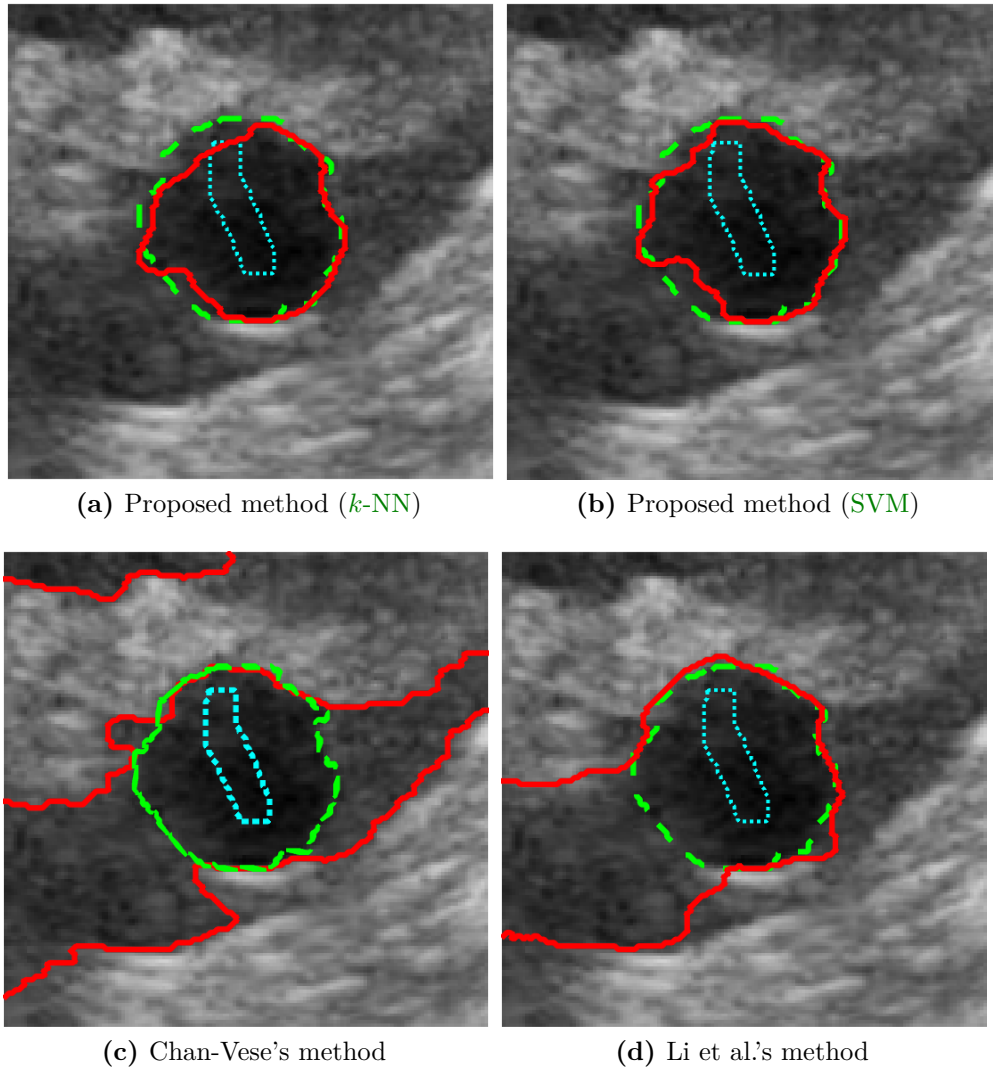

(a) Proposed method (k-NN) **(b)** Proposed method (SVM)

(c) Chan-Vese's method **(d)** Li et al.'s method

Figure 5.8: Segmentation results for the renal cyst using various methods

Table 5.3: Computational time (in second)

#	Images (Modality)	Proposed Method [a]		C-V's Method	Li et al.'s Method
		k-NN	SVM		
1	Brain tumor (MRI)	7.45 (2.11)	7.57 (3.34)	5.05	9.98
2	Liver tumor (CT)	5.49 (2.08)	6.27 (0.16)	3.23	9.58
3	Renal cyst (US)	7.04 (2.57)	6.75 (0.31)	12.11	8.07

[a] Numbers in brackets denote the training time.

In our experiments, C-V's method generates poor results for the brain tumor as well as the renal cyst images in the presence of inhomogeneity. Some images are poorly segmented using the general parameter setting (Figures 5.6(c) and 5.8(c)). The poor results can be avoided by applying a specific setting for the images; however, setting parameters for each image is a difficult and tedious task. It is also known that traditional edge-based active contour models often fail to converge at a poorly defined boundary. This is indeed the case in most of our experiments where the contours in Li et al.'s method evolve beyond the desired boundary. These issues are solved using the proposed method. The results confirm that the active contour model using the proposed ESFs outperforms traditional region-based and edge-based active contour models.

It is clear that function ρ plays an important role when a poorly defined boundary is present. It generates a minimum value when the scores are at the decision boundary. Furthermore, retaining the gradient information is beneficial at clear boundaries since there are no fuzzy values. Function

Table 5.4: Segmentation accuracy from various methods

#	Images	Proposed Method				Chan-Vese's Method		Li et al.'s Method	
		k-NN		SVM					
		JI	SI	JI	SI	JI	SI	JI	SI
1	Brain tumor	0.83	0.91	0.85	0.92	0.68	0.80	0.67	0.79
2	Liver tumor	0.93	0.97	0.94	0.97	0.92	0.96	0.37	0.49
3	Renal cyst	0.89	0.94	0.89	0.94	0.70	0.80	0.60	0.73

Table 5.5: Segmentation accuracy using Equation (5.5)

No	Images	Modality	k-NN		SVM	
			JI	SI	JI	SI
1	Brain tumor	MRI	0.81	0.89	0.85	0.92
2	Liver tumor	CT	0.93	0.96	0.94	0.97
3	Renal syst	US	0.90	0.95	0.90	0.95

g_{new} incorporates both of these advantages to give accurate segmentation results. In addition, the proposed framework is flexible and can be applied to other models that utilize an ESF. Any classifier can be used to construct an ESF using a family of functions ρ. Experiments on medical images using different ρ based on Equation (5.5) for $p = 4$ with the corresponding data test from Table 5.3 are presented in Table 5.5. The accuracy is similar to that obtained with the use of Equation (5.1) which indicates that the

proposed framework is not sensitive to the choice of a good ρ function.

An edge based active contour model is generally sensitive to initialization. In addition, a probability score is sensitive to training data. The foreground initialization in our experiments is used not only to initialize the contour but also to learn the foreground pixels. It is worth noting that an appropriate initialization is required, particularly for inhomogeneous objects. Training data should cover the variety of the foreground to generate a good segmentation result as shown in Figure 5.9(d).

It is worth noting that multi-class classification problem (the number of labels is larger than 2) is very common and important. Even though the nature for each classification type is different, the two-class classification problem may be extended to more-class classification problem. Particularly, the two machine learning algorithms which are used in the experiments can be used for multi-class classification [119, 120, 121]. However, the level set method only utilizes one level embedded function only to represent the curve $\mathcal{C}$, i.e., Equation (2.25). The curve separates the region between $\phi(x) > 0$ and $\phi(x) < 0$. Consequently, there are only two regions (classes) based on $\phi(x)$. This is a limitation in our proposed method where the segmentation is only dedicated to two-class classification problem. Some studies on multi-level set method [122, 123, 124] may be able to handle multi-class classification; however, managing multi-level for the embedded function may be complicated.

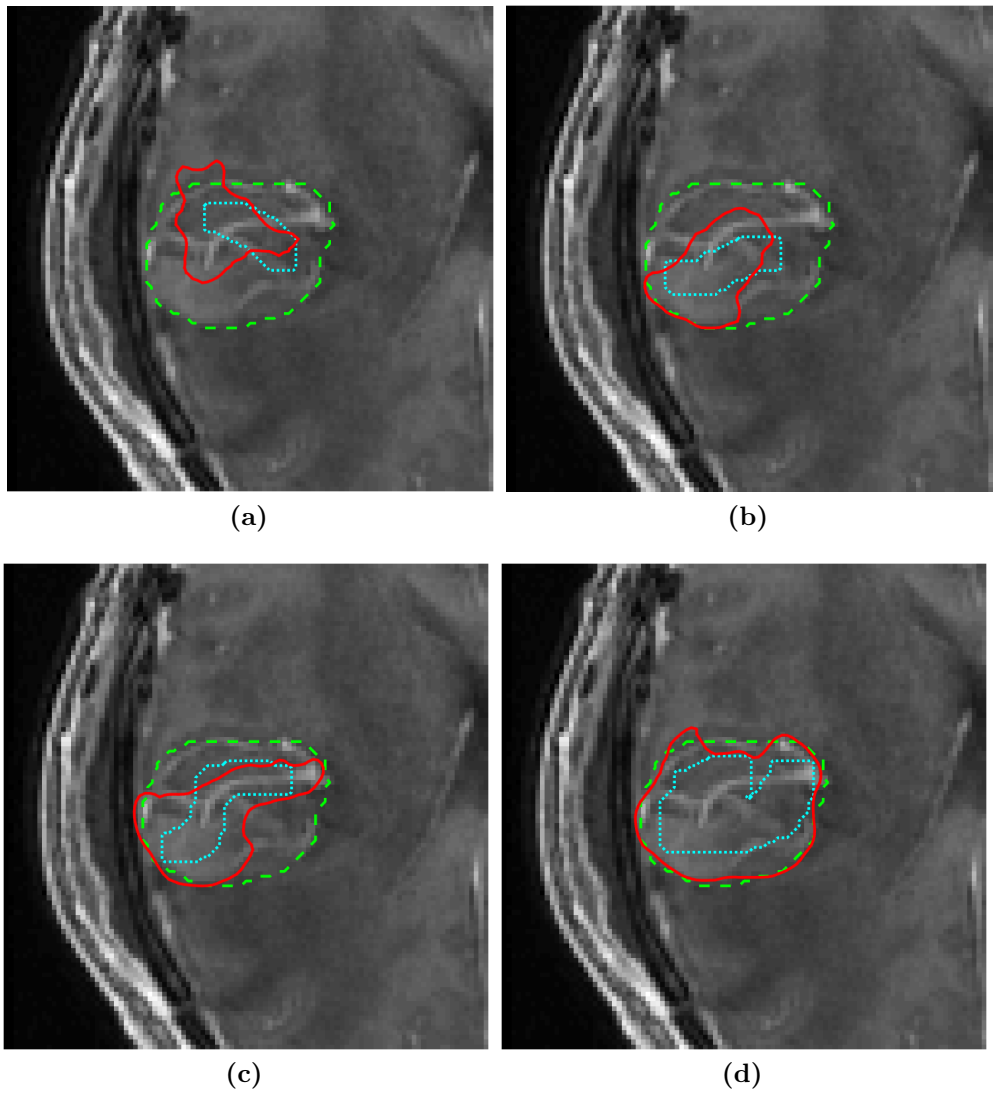

Figure 5.9: Results from various initializations on the brain tumor image.

5.5 Summary

We have proposed a framework to construct a group of robust ESFs for edge-based active contour models which can be used to detect poorly defined boundaries. The framework utilizes edge-based information from image gradient values as well as probability scores from a classifier. Our framework is sufficiently flexible to be applicable to other edge-based active contour models that use ESFs and can be constructed from any classifier.

The proposed framework is tested on medical images comprising the brain and liver tumor as well as renal cyst images. Experiments on these images using the DRLSE for the implementation of the edge-based active contour model as well as the k-NN and the SVM for the classification algorithms confirm the effectiveness of our framework. The proposed framework generates more accurate segmentation results compared to the traditional edge-based active contour model (Li et al.'s method) as well as the region-based active contour model (C-V's method). Furthermore, the framework converges faster compared to Li et al.'s method). Last but not least, the ESFs in our framework is not sensitive to the choice of ρ function as long as it follows the properties of a good ρ.

Chapter 6

Active Contour with Region of Class Probability

6.1 Introduction

Generally, existing image segmentation models using level set methods can be grouped into two categories: edge-based models and region-based models [11, 12, 13, 14]. Edge-based models utilize edge information while region-based models employ a region descriptor to control the motion of the active contour [15]. Region-based models are not sensitive to objects with poorly defined boundaries but are sensitive to inhomogeneity of image intensities, i.e., the overlapping of the intensity ranges. Also, they are sensitive to parameter tuning [17, 18] which is not desirable in practical use.

Another popular approach is the use of machine learning algorithms to classify each pixel based on training data. Many algorithms are found in the literature; e.g., the k-nearest neighbors (k-NN), support vector machine (SVM), extreme learning machine, etc [19, 16]. These algorithms can

handle complex patterns, but further post-processing such as morphological operations are often required to obtain the final solution without employing an objective function.

To overcome the limitation of these approaches, a number of studies include classifier probability scores from overall pixel classification instead of pure intensity values [125, 126, 127, 128, 129]. Different from existing methods, our framework works in a simpler manner. The scores are in a matrix in the range of $[0, 1]$ which are subsequently regularized by a non-linear function. Finally, the region-based active contour model proposed by Chan and Vese is applied to the matrix to find the optimal solution. The solution thus converges faster and is less sensitive to parameter tuning of the LSM without compromising accuracy.

6.2 Proposed Framework

The proposed framework can be constructed from any classification algorithm and applied to any region-based model using an LSM. The k-NN and SVM are selected to generate a matrix of classifier probability scores. Probability scores from classification algorithms generally fall in the range $[0, 1]$ or $(-\infty, +\infty)$. The scores of the k-NN are of the first type while those of the SVM are of the second. Some methods are available to convert the second type to prior probability score, e.g., the Platt method [116].

Originally, classifiers generate binary results which are obtained from applying a hard limiter function for their probability scores. Let $s \in [0, 1]$ be a probability score and ρ a regularization function that maps s to a real

value in $[0, 1]$. The traditional classifier generates binary results by applying

$$\rho(s) = \begin{cases} 1 & \text{if } s \geq \frac{1}{2}, \quad (6.1a) \\ 0 & \text{if } s < \frac{1}{2}. \quad (6.1b) \end{cases}$$

Instead of refining these binary scores using machine learning algorithms, we retain the probability scores to be processed further by applying any region-based active contour model. The map of the probability scores is used to replace the original image during computation.

The simplest function for $\rho(s)$ is the identity function which can be expressed by

$$\rho(s) = s. \quad (6.2)$$

The plot of Equation (6.1) is shown in Figure 6.1(a) while that of Equation (6.2) in Figure 6.1(b). The former is binary while the latter is linear.

Based on our preliminary results, a non-linear function ρ approximately lying under ρ_2 for $s > 0.5$ and above ρ_2 for $s < 0.5$ produces better solutions. It is worth noting the properties of a good ρ:

(a) the domain, s, as well as the range, $\rho(s)$, lie in $[0, 1]$,

(b) it is monotonically increasing,

(c) the following equations hold

$$\lim_{s \to 0} \rho(s) = 0, \quad (6.3)$$

$$\lim_{s \to 0.5} \rho(s) = 0.5, \quad (6.4)$$

$$\lim_{s \to 1} \rho(s) = 1, \tag{6.5}$$

(d) it should be close to 0.5 when s is in the vicinity of 0.5.

In our experiments, the implication

$$0 < |s - 0.5| < 0.1 \implies |\rho(s) - 0.5| < 0.015$$

holds. A function that meets these properties is

$$\rho(s) = \frac{1 + (2s - 1)^p}{2}, \text{ for } s \in [0, 1] \text{ and } p = 3, 5, 7, ... \tag{6.6}$$

Any other functions having similar characteristics also can be employed as $\rho(s)$, e.g.,

$$\rho(s) = \frac{1 - \cos^p \pi s}{2}, \text{ for } s \in [0, 1] \text{ and } p = 3, 5, 7, ... \tag{6.7}$$

The plot of Equations (6.6) and (6.7), for $p = 5$, are shown in Figure 6.1 (c) and (d), respectively. Both functions are non-linear.

The map of ρ is then fed to a region-based active contour model. Through energy minimization using the level set method, the optimum solution for the desired region can be obtained.

6.3 Experimental Setup

We apply our proposed method to several images for evaluation. The experiments and results are described below.

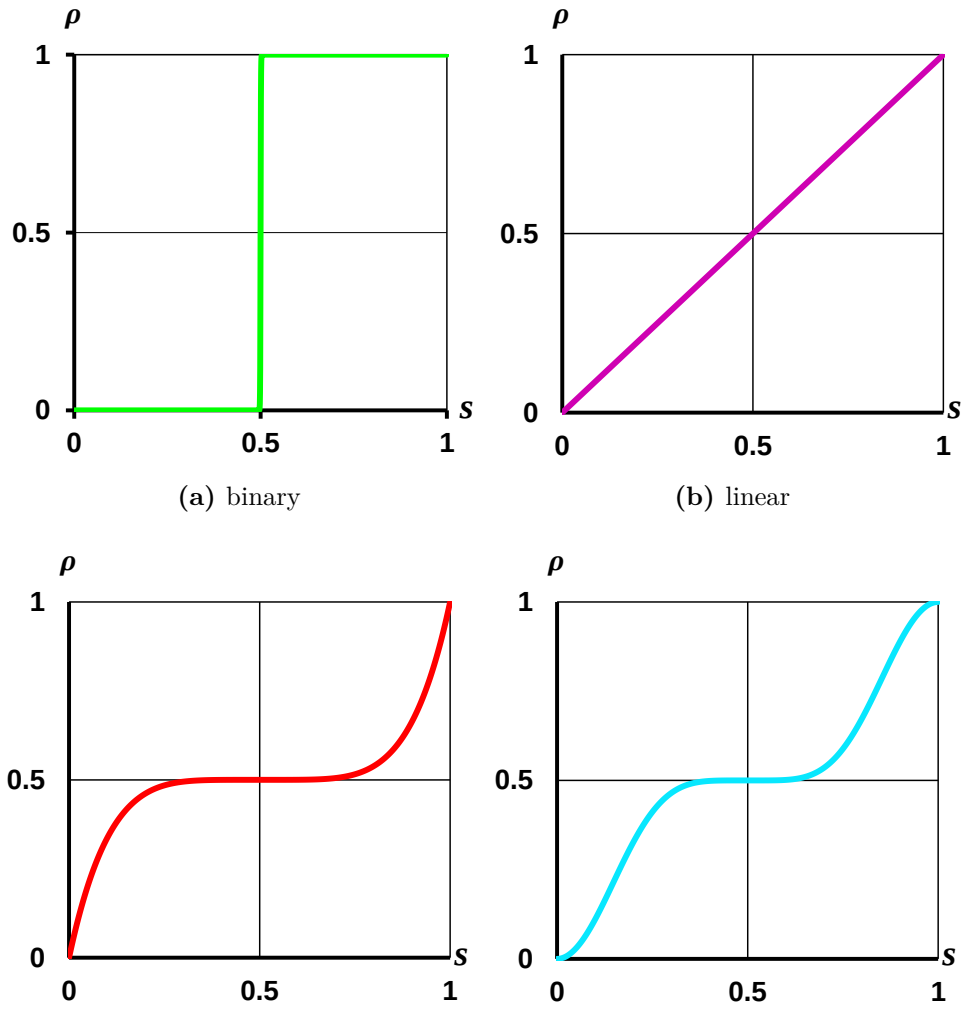

(a) binary **(b)** linear

(c) polynomial **(d)** sinusoidal

Figure 6.1: Various types for regularization function.

6.3.1 Data Set

To evaluate the effectiveness of the proposed method, a number of medical images are used. They are images of brain tumour (5 images), liver tumor (3 images), and renal cyst (3 images) with respective modalities computed tomography (CT), magnetic resonance imaging (MRI), and ultrasound (US). The resolutions are listed in Table 6.1. All images come from different patients and their ground truths are drawn by an expert.

Table 6.1: Image data set

No	Images	Modality	Number of images	Resolution
1	Renal syst	US	3	450 ×6 00
2	Liver tumor	CT	3	512 × 512
3	Brain tumor	MRI	5	512 × 512

6.3.2 Parameter Tuning

The proposed method is implemented in Matlab. The region-based active contour model from Chan and Vese implemented by Getreuer is utilized [130]. Unless otherwise stated, the parameter values are listed in Table 6.2. The radial basis function is used as the kernel function in the SVM. Since this study is not intended to design a sophisticated feature vector, a simple vector containing an image patch of size 3×3 is used for all the experiments.

The segmentation starts with an initialization comprising two manually

Table 6.2: Parameter setting for the experiments

Symbol	Quantity	Value
μ	coefficient of the weighted length term	0.5
v	coefficient of the weighted area term [a]	0
λ_1	coefficient of inside fit penalty	1
λ_2	coefficient of outside fit penalty	1
dt	timestep parameter	1
k	the number of neighbors in the fuzzy k-NN algorithm	8

[a] $v = 0$ means that the area term is not used for the experiments.

drawn marks to train the classifier (Figure 6.2). The green mark indicates

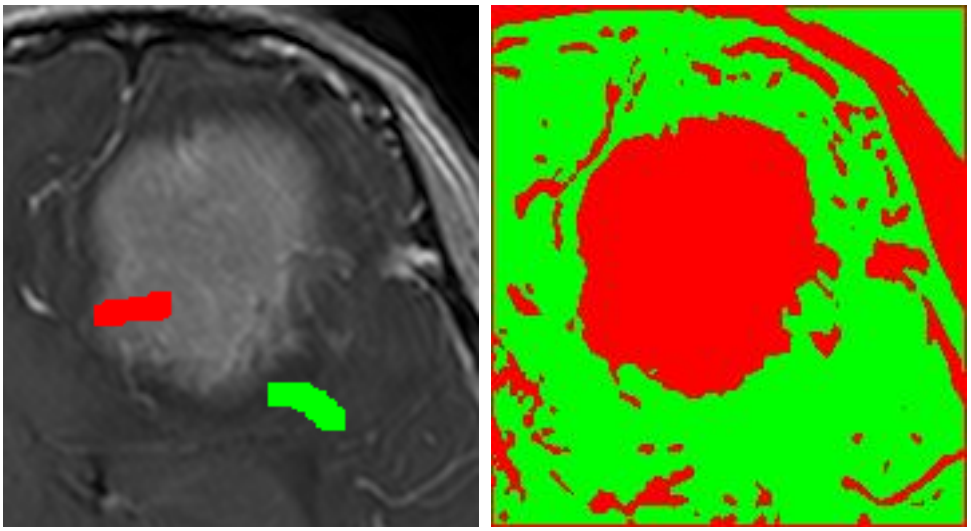

(a) User initialization **(b)** Binary segmentation result

Figure 6.2: User initialization and the corresponding binary result using Equation (6.1).

the background and the red mark the foreground.

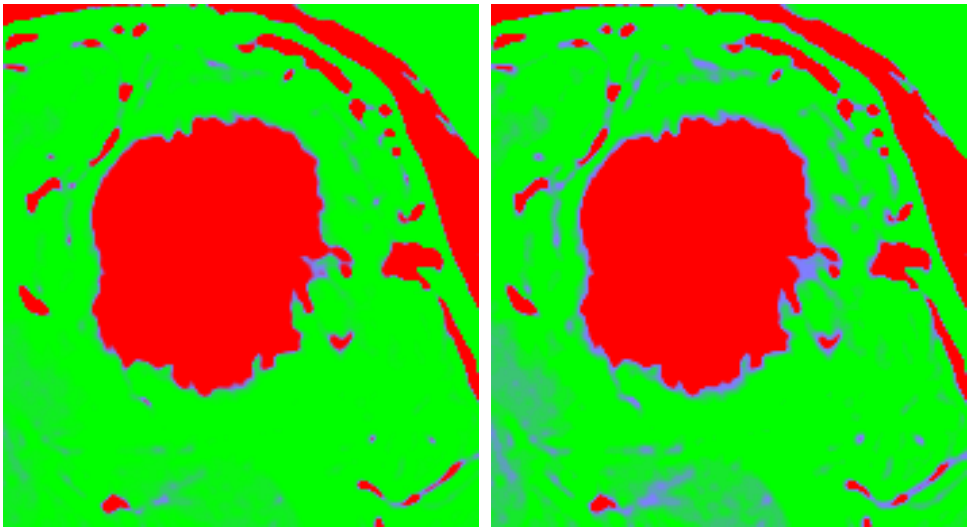

(a) Linear function **(b)** Polynomial function

Figure 6.3: Regularized probability score map using Equations (a) 6.2 and (b) 6.6 in pseudo-color.

6.3.3 Quality Assessment

We compare our results with the original Chan-Vese method as well as another method from the area-based cost function, i.e., the edge-based active contour model proposed by Li et al. Different from our method, which shares the same parameters tuning for all imaging modalities, the original methods of Chan-Vese and the Li et al. use specific parameter values for each imaging modality. The parameters are carefully chosen by iterating the combination of them.

To evaluate the segmentation accuracy, two popular metrics are used, i.e, the Jaccard index (JI) and the Dice coefficient, also known as the similarity index (SI).

6.3.4 How the Proposed Method Works

The ρ maps generated using Equations (6.1), (6.2), and (6.6) are shown in Figures 6.2(b), 6.3(a), and (b), respectively. As can be seen, the original binary result from a machine learning algorithm (Figure 6.2(b)) is very noisy and it would be difficult to refine the solution. Applying a morphological operator is commonly done to remove the noise, but there is no objective function inside. In addition, applying Equation (6.1) ignores the degree of certainty. A pixel in class one may come from either the absolute probability score 1 or a real value in $[0.5, 1)$.

A better map of ρ is obtained by applying a linear mapping as expressed in Equation (6.2) (Figure 6.3(a)). Pixels whose scores are close to 0.5 are shown in purple. Since we wish to emphasize the fuzziness, we introduce a non-linear mapping which gives more weight for scores close to 0.5 through either Equation (6.6) or (6.7). An example of a ρ map using Equation (6.6) is shown in Figure 6.3(a). Pixels with high confidence of being background are in green, and those with low confidence are in red. The regularized ρ map is subsequently used to replace the original image (image u_0) in the Chan-Vese's method where the level set method computation is applied on the original image.

Based on experiments, the use of the regularized ρ map makes the algorithm converge faster. Further more, the accuracy is also improved. The detailed results for the computational time and accuracy are presented in Sub Section 6.4.

6.4 Results and Discussions

The optimum solution is obtained by applying the region-based active contour model proposed by Chan and Vese (C-V) to ρ using Equation (6.7) without any intention to downplay the importance of Equation (6.6). The initial zero level set is obtained from the foreground boundary during training. The map of ρ plays an important role in our method.

A number of qualitative segmentation results are shown in Figures 6.4, 6.5, and 6.6 while the quantitative results are listed in Tables 6.3 and 6.4.

Table 6.3: Comparison of segmentation accuracy

Exp.	Images	Our Method				C-V's Method		Li et al.'s Method	
		k-NN		SVM					
		JI	SI	JI	SI	JI	SI	JI	SI
1	Renal cyst	0.84	0.91	0.84	0.91	0.83	0.90	0.83	0.91
2	Liver tumor	0.93	0.97	0.93	0.96	0.66	0.70	0.68	0.77
3	Brain tumor	0.82	0.90	0.81	0.90	0.59	0.69	0.81	0.89

As can be seen in Table 6.3, our method using k-NN and SVM generate similar results. Experiment 2, where the liver tumor images are used, achieves the best performance compared to the brain tumor and renal cyst images. Applying either the k-NN or SVM generates accuracy 0.93 for JI. The slight difference for SI, i.e., 0.01, comes from the rounding of real numbers.

For comparison purpose, the segmentation accuracy from C-V's and Li

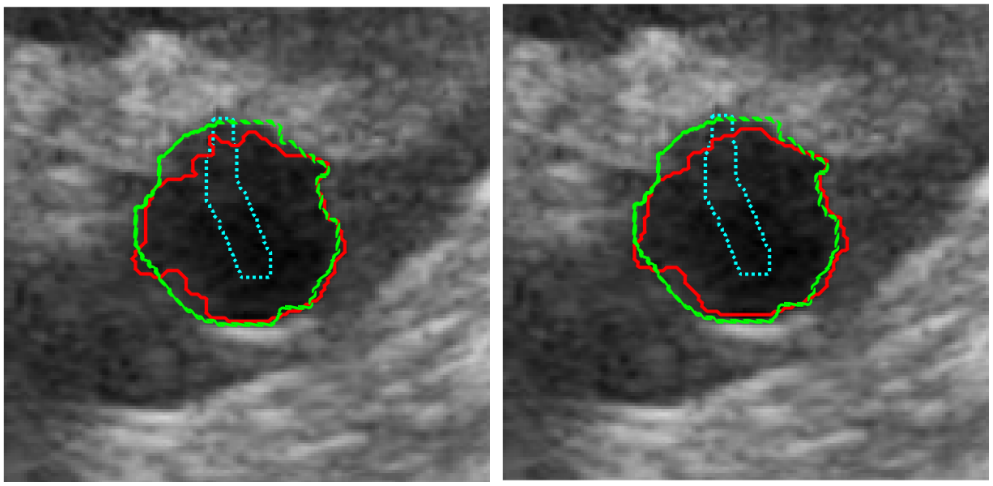

(a) Proposed method (k-NN) **(b)** Proposed method (SVM)

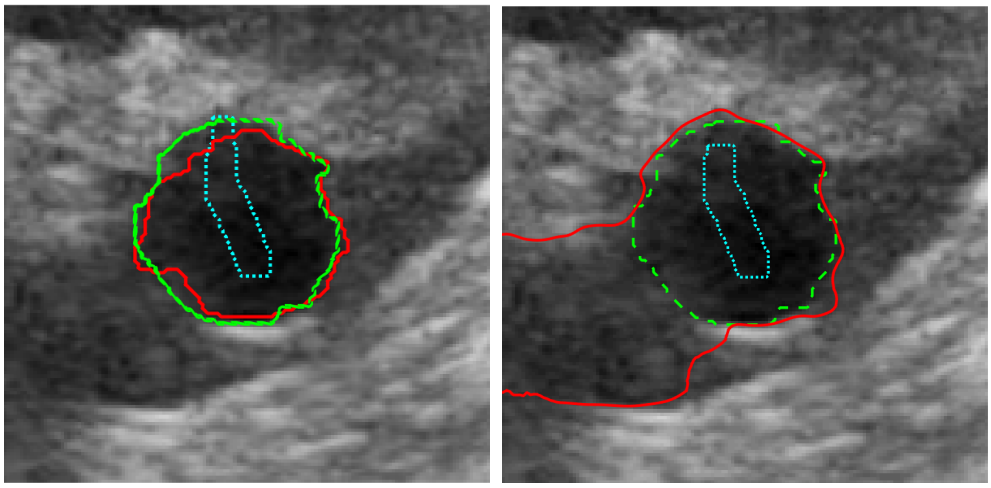

(c) Chan-Vese's method **(d)** Li et al.'s method

Figure 6.4: Segmentation results for the renal cyst using various methods

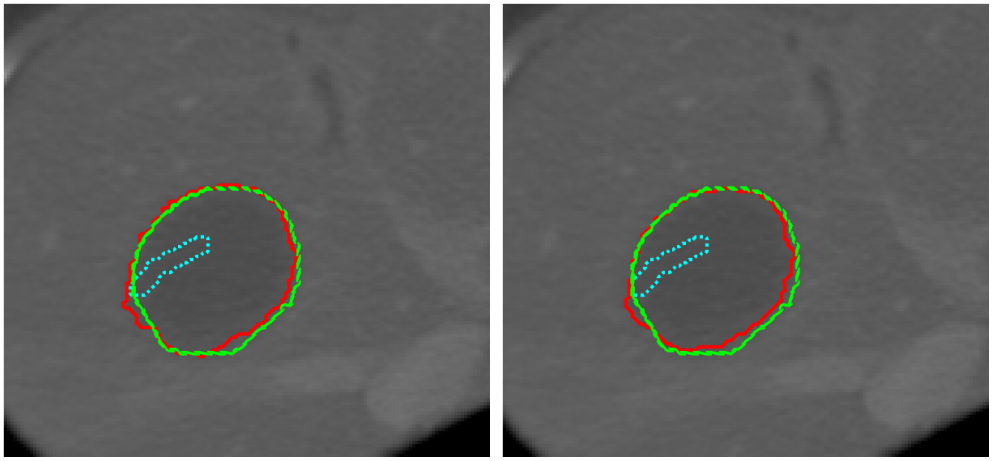

(a) Proposed method (*k*-NN) **(b)** Proposed method (SVM)

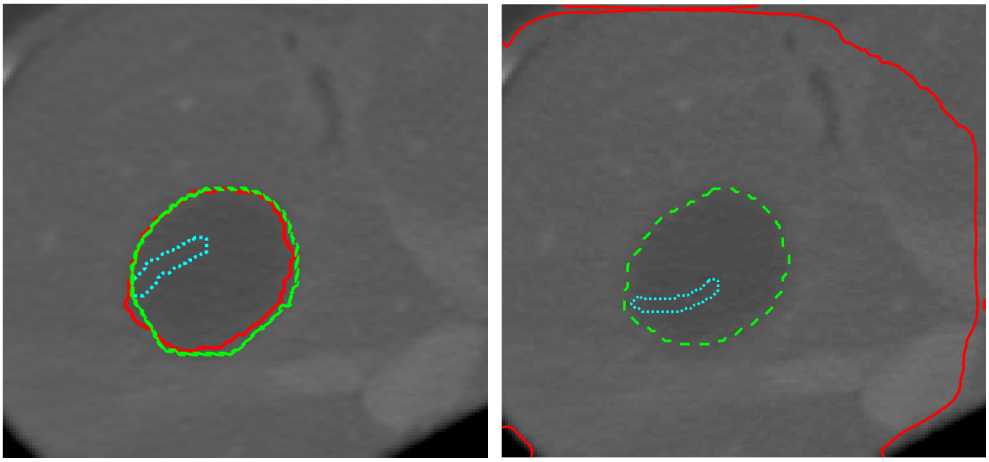

(c) Chan-Vese's method **(d)** Li et al.'s method

Figure 6.5: Segmentation results for the liver tumor using various methods

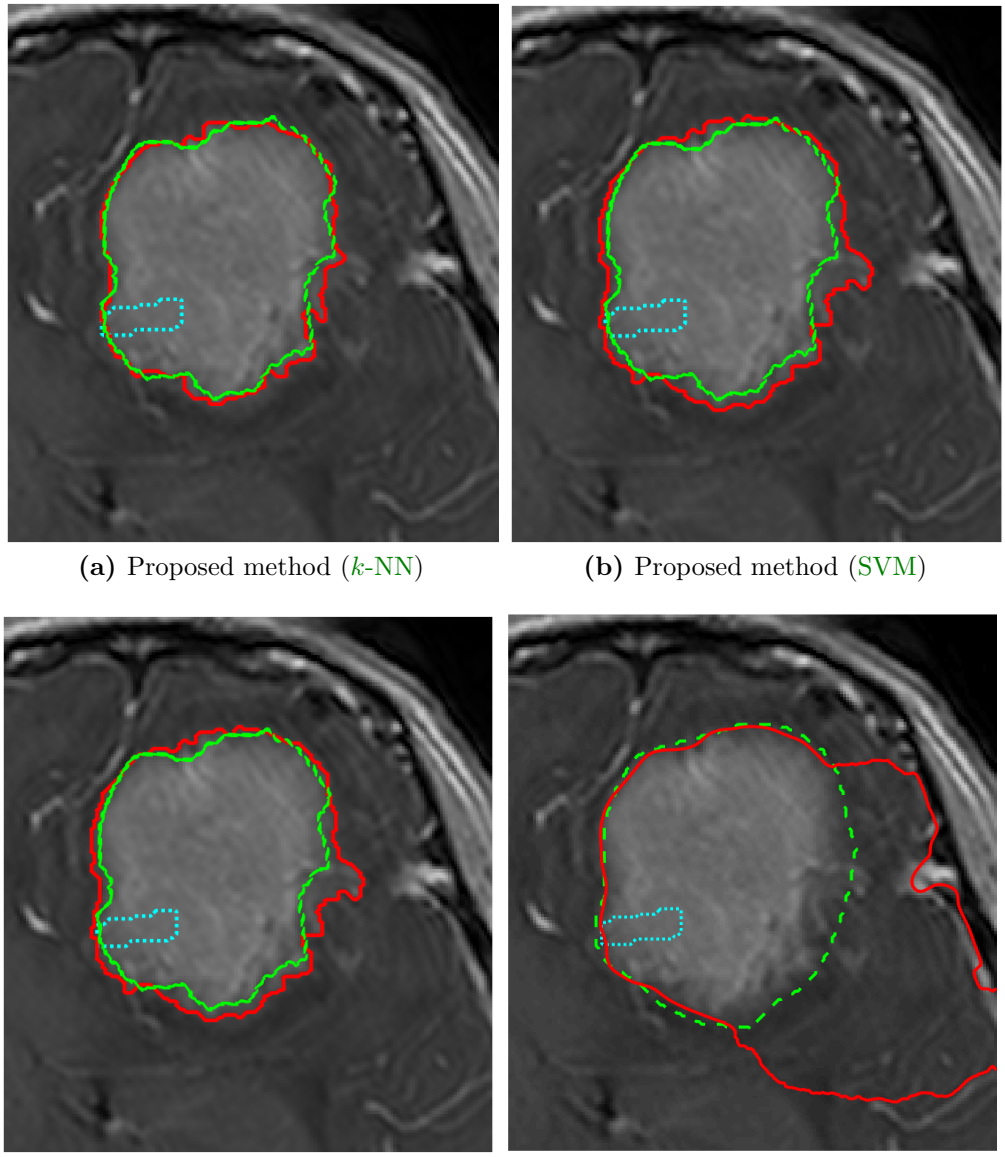

(a) Proposed method (k-NN)

(b) Proposed method (SVM)

(c) Chan-Vese's method

(d) Li et al.'s method

Figure 6.6: Segmentation results for the brain tumor using various methods

Table 6.4: Segmentation accuracy using Equation (6.6)

No	Images	k-NN		SVM	
		JI	SI	JI	SI
1	Renal cyst (US)	0.83	0.90	0.85	0.92
2	Liver tumor (CT)	0.93	0.96	0.93	0.96
3	Brain tumor (MRI)	0.81	0.89	0.81	0.90

et al.'s methods are also listed in Table 6.3. As can be seen, the proposed method consistently generates higher accuracy. Compared to C-V's method, the proposed method significantly generates higher accuracy for segmenting the brain and liver tumor images and slightly higher for the renal cyst. The proposed method is also significantly better for segmenting the liver tumors and slightly better for the remaining.

It is worth noting that in C-V's and Li et al.'s methods, it is difficult to find a general setting for parameter tuning even for the set of images in a data volume. A set of parameters may generate a good result on a certain slice but gives poor results for other slices. Some of the almost perfect results from C-V's method are shown Figure 6.5, and 6.6. The same is true for Li et al.'s method when segmenting the brain tumors. Note that our parameter values are the same overall imaging modalities, unlike the others.

The ρ map is less sensitive to parameter tuning compared to the pixel intensities in the traditional C-V's as well as Li et al.'s method. The key for a good ρ map is the regularization function that emphasizes the ambiguity

of the class probability. The experimental results using Equation (6.6) with $p = 5$, which generate similar results, are shown in Table 6.4. The proposed method is not sensitive to the choice of non-linear function as long as it follows the properties of a good ρ.

The computational times to complete the task for all methods are presented in Table 6.5. As can be seen, the proposed method generally converges faster even though it requires training time. Compared to C-V's method, the proposed method using either k-NN or SVM is significantly faster for segmenting the brain and liver tumors, and slightly longer for renal cysts. In addition, the proposed method using either k-NN or SVM is faster for all images compared to Li et al's method.

Table 6.5: Computational time (in second)

No	Images	Our Method [a]		C-V's	Li et al.'s
		k-NN	SVM	Method	Method
1	Renal cyst (US)	3.80 (1.61)	8.91 (5.78)	8.74	11.40
2	Liver tumor (CT)	1.82 (1.10)	2.04 (1.20)	2.24	7.04
3	Brain tumor (MRI)	3.79 (1.56)	5.61 (2.93)	6.40	10.29

[a] Numbers in brackets denote the training time which are already included in the computational time.

6.5 Summary

We have proposed a framework to integrate machine learning algorithms with region-based active contour models. The framework utilizes classification

probability scores which are regularized using a non-linear mapping. Our framework is flexible to be applied to any classifier integrated to region-based active contour models.

An experimental implementation using the k-NN and the SVM integrated to the C-V's method confirms the effectiveness of our framework. Three data sets of the brain and liver tumor as well as the renal cyst are used in the experiments. The proposed method generally outperforms the traditional C-V's method as well as the Li et al.'s method, both in accuracy and computational time.

The proposed method is not sensitive to the choice of regularization function as long as it follows the properties of a good ρ. Experimental results using polynomial and trigonometric function consistently show the similar results.

The experiments also show that the solutions can be obtained easily with a simple feature vector and lower sensitivity to parameter tuning. All experiments, which cover several modalities containing tumor and cyst images, utilize the same parameter tuning for the implementation of the region-based active contour model using the LSM. This is almost impossible in the traditional method such as C-V's and Li et al.'s method where the parameter tuning is a quite difficult task. Each parameter in the LSM should be tuned carefully for different modalities, organs, or tumors.

Chapter 7

Conclusions and Future Work

7.1 Conclusions

Machine learning algorithms and the level set methods continue to play increasingly important roles in medical image analysis. This thesis has introduced a framework for combinatorial methods. Since there are numerous possible combinations, only two popular approaches i.e., classification algorithm and active contour are explored further by proposing several ways to integrate classification algorithms with the active contour models using the LSMs. The integration covers both the edge-based as well as region-based active contour models.

First, we demonstrate how to integrate classification algorithms and the edge-based active contour models in Chapter 4. A classifier is first applied followed by the edge-based active contour model. classification algorithms effectively generate results that can be employed as initial contours. These contours are close enough to the true boundaries even with minimal user initialization. The contours are subsequently evolved using edge-based active contour models toward the true boundaries. In general,

the better the initializations, the better the results. The experiments using six selected classification algorithms confirm the effectiveness of our framework to segment medical images. The use of the combination can enhance the segmentation accuracy compared to that of a single algorithm. Among the selected algorithms, the k-NN and the SVM combined with the edge-based active contour model consistently demonstrates above-average accuracy compared to the integration from NBC, ELM, ANN, and random forests.

The integration above can be considered as a simple combination of various methods. In the second work, which is described in Chapter 5, we integrate the classification algorithm and level set methods more closely to construct robust ESFs. Instead of refining the binary classification, we retain the class probability score to be embedded in the edge-stop function to control the contour motion. We introduce two fuzzy edge-stop functions which are used to regularize the traditional ESF. These functions make the contours stop precisely at poorly defined boundaries. Experimental results also indicate that our proposed method outperforms the methods from Li et. al and Chan-Vese. The edge-based active contour model using ESF converges faster and gives more accurate segmentations.

The integration described in Chapter 4 and 5 combine classification algorithms with the edge-based active contour models. In Chapter 6, we extend our investigation to integrate classification algorithm with the region-based active contour model. Similar to the previous work in Chapter 5, classification algorithms are employed to generate maps of class probability scores. Instead of being applied to pixel intensities, the region-based active

contour employs the obtained maps. We also propose two functions to regularize the maps before applying the region-based active contour model. Empirical experiments confirm that the two functions effectively generate better results compared to the traditional methods from Li et al. and Chan-Vese. The proposed method generally converges faster even though it requires training time. The segmentation results are more accurate compared to the other selected methods. Moreover, parameter tuning is not an issue any more since our framework utilize global setting for all the experiments to generate the results while the others require tuning for each modality and even for a particular image.

7.2 Future Work

Some directions for our future works which are apparent from my thesis are described below.

1. Future investigation including implementation of other segmentation techniques in Chapter 3

   There are many possible combinations that can be explored further to generate better accuracy and computational time. While combining and integrating ML algorithm and active contour models are only small parts of the possible combinations, research for not only combining but also tightly integrating on other methods is still widely open.

2. Using various feature vectors in Chapter 4

   The feature vectors can be enhanced by utilizing shape descriptors to

learn an object form which may increase the segmentation accuracy. The relation between organs and imaging modalities to predict the appropriate segmentation methods may also be investigated.

3. Using deep learning for feature learning in Chapters 4, 5, and 6

   The feature vector used in Chapters 4,5, and 6 is manually designed. Recent approach for feature learning in deep learning may be implemented to obtain better results.

4. Combining the methods in Chapter 4 and 5

   In Chapter 4, classification algorithms are utilized to generate good initialization followed by applying the traditional edge-based active contour model. On the other hand, the work in Chapter 5 utilize the boundary of user's initial marks followed by enhanced edge-based contour model containing a robust ESF. The advantage from each work can be combined by generating initializations as described in Chapter 4 followed by applying an edge-based active contour model with a robust ESF.

5. Integrating the fuzzy ESF with the contour speed

   The fuzzy ESF in Chapter 5 is utilized only to stop contour only and implicitly control the contour speed. The fuzzy ESF may be embedded explicitly to the contour speed equation.

6. Applying the methods to larger datasets

   In our work, the datasets are limited particularly for the ground-truth. Applying the proposed methods for larger datasets can be investigated

to cover problems that may not appear in smaller datasets.

7. Extending the methods to 3D segmentation

   We work on 2D segmentation for all works in this thesis. Extending the proposed method to 3D segmentation is also possible to be investigated by considering the existing works in segmentation, e.g., 3D level set segmentation.

References

[1] R. Jain, R. Kasturi, and B. G. Schunck, *Machine Vision*. McGraw-Hill, Inc., 1995.

[2] F. Zhao and X. Xie, "An overview of interactive medical image segmentation," *Annals of the BMVA*, vol. 2013, no. 7, pp. 1–22, 2013.

[3] A. Elnakib, G. Gimel'farb, J. S. Suri, and A. El-Baz, *Multi Modality State-of-the-Art Medical Image Segmentation and Registration Methodologies*. New York: Springer, Feb 2011, ch. Medical Image Segmentation: A Brief Survey, pp. 1–39.

[4] N. Gordillo, E. Montseny, and P. Sobrevilla, "State of the art survey on MRI brain tumor segmentation," *Magnetic Resonance Imaging*, vol. 31, no. 8, pp. 1426–1438, Oct. 2013.

[5] J. Liu, X. Liu, J. Chen, and J. Tang, *Advanced Intelligent Computing Theories and Applications. With Aspects of Artificial Intelligence*. Springer Berlin Heidelberg, 2012, vol. 6839, ch. Mass Segmentation in Mammograms Based on Improved Level Set and Watershed Algorithm, pp. 502–508.

[6] M. Kass, A. Witkin, and D. Terzopoulos, "Snakes: Active contour models," *International Journal of Computer Vision*, vol. 1, no. 4, pp. 321–331, 1988.

[7] A. Dervieux and F. Thomasset, "A finite element method for the simulation of a Rayleigh-Taylor instability," in *Approximation Methods for Navier-Stokes Problems*. Springer, 1980, pp. 145–158.

[8] S. Osher and J. A. Sethian, "Fronts propagating with curvature dependent speed: Algorithms based on Hamilton-Jacobi formulations," *Journal of Computational Physics*, vol. 79, no. 1, pp. 12–49, 1988.

[9] V. Caselles, F. Catté, T. Coll, and F. Dibos, "A geometric model for active contours in image processing," *Numerische mathematik*, vol. 66, no. 1, pp. 1–31, 1993.

[10] V. Caselles, R. Kimmel, and G. Sapiro, "Geodesic active contours," *International Journal of Computer Vision*, vol. 22, no. 1, pp. 61–79, 1997.

[11] C. Li, R. Huang, Z. Ding, J. Gatenby, D. N. Metaxas, and J. C. Gore, "A level set method for image segmentation in the presence of intensity inhomogeneities with application to MRI," *IEEE Transactions on Image Processing*, vol. 20, no. 7, pp. 2007–2016, 2011.

[12] Y. Wang, L. Liu, H. Zhang, Z. Cao, and S. Lu, "Image segmentation using active contours with normally biased GVF external force," *IEEE Signal Processing Letters*, vol. 17, no. 10, pp. 875–878, 2010.

[13] S. Mukherjee and S. Acton, "Region based segmentation in presence of intensity inhomogeneity using legendre polynomials," *IEEE Signal Processing Letters*, vol. 22, no. 3, pp. 298–302, March 2015.

[14] A. Pratondo, C.-K. Chui, and S.-H. Ong, "Robust edge-stop functions

for edge-based active contour models in medical image segmentation," *IEEE Signal Processing Letters*, vol. 23, no. 2, pp. 222–226, 2016.

[15] T. F. Chan and L. Vese, "Active contours without edges," *IEEE Transactions on Image Processing*, vol. 10, no. 2, pp. 266–277, 2001.

[16] A. Pratondo, B. P. Nguyen, C.-K. Chui, and S.-H. Ong, "Vocal cord segmentation from CT images using machine learning," in *Proceedings of the 10th Asian Conference on Computer Aided Surgery (ACCAS 2014)*. The Japan Society of Computer Aided Surgery, 2014, pp. 40–41.

[17] X. Cai and A. Sowmya, "Learning to tune level set methods," in *The 24th International Conference on Image and Vision Computing New Zealand (IVCNZ 2009)*. IEEE, 2009, pp. 310–315.

[18] E. A. Mylona, M. A. Savelonas, and D. Maroulis, "Automated adjustment of region-based active contour parameters using local image geometry," *IEEE Transactions on Cybernetics*, vol. 44, no. 12, pp. 2757–2770, 2014.

[19] M. D. Steenwijk, P. J. Pouwels, M. Daams, J. W. van Dalen, M. W. Caan, E. Richard, F. Barkhof, and H. Vrenken, "Accurate white matter lesion segmentation by k-nearest neighbor classification with tissue type priors (kNN-TTPs)," *NeuroImage: Clinical*, vol. 3, pp. 462–469, 2013.

[20] C. Li, C. Xu, C. Gui, and M. D. Fox, "Distance regularized level set evolution and its application to image segmentation," *IEEE Transactions on Image Processing*, vol. 19, no. 12, pp. 3243–3254, 2010.

[21] N. Gordillo, E. Montseny, and P. Sobrevilla, "State of the art survey on MRI brain tumor segmentation," *Magnetic Resonance Imaging*, vol. 31, no. 8, pp. 1426–1438, 2013.

[22] J. Liu, X. Liu, J. Chen, and J. Tang, "Mass segmentation in mammograms based on improved level set and watershed algorithm," in *Advanced Intelligent Computing Theories and Applications*. Springer, 2011, pp. 502–508.

[23] I. Bankman, *Handbook of Medical Image Processing and Analysis*. Academic Press, 2008.

[24] C. A. Glasbey and G. W. Horgan, *Image Analysis for The Biological Sciences*. Wiley Chichester, 1995, vol. 1.

[25] R. C. Gonzalez and R. E. Woods, *Digital Image Processing, Third Edition*. Prentice Hall Press, 2002.

[26] R. Adams and L. Bischof, "Seeded region growing," *IEEE Transactions on Pattern Analysis and Machine Intelligence*, vol. 16, no. 6, pp. 641–647, 1994.

[27] D. Chaudhuri and A. Agrawal, "Split-and-merge procedure for image segmentation using bimodality detection approach," *Defence Science Journal*, vol. 60, no. 3, p. 290, 2010.

[28] V. Grau, A. Mewes, M. Alcaniz, R. Kikinis, and S. K. Warfield, "Improved watershed transform for medical image segmentation using prior information," *IEEE Transactions on Medical Imaging*, vol. 23, no. 4, pp. 447–458, 2004.

[29] A. Oliver, X. Munoz, J. Batlle, L. Pacheco, and J. Freixenet, "Improving clustering algorithms for image segmentation using contour and region information," in *2006 IEEE International Conference on Automation, Quality and Testing, Robotics*, vol. 2. IEEE, 2006, pp. 315–320.

[30] D. Withey and Z. Koles, "Medical image segmentation: Methods and software," in *Noninvasive Functional Source Imaging of the Brain and Heart and the International Conference on Functional Biomedical Imaging, 2007. NFSI-ICFBI 2007. Joint Meeting of the 6th International Symposium on.* IEEE, 2007, pp. 140–143.

[31] C. Zhan, X. Duan, S. Xu, Z. Song, and M. Luo, "An improved moving object detection algorithm based on frame difference and edge detection," in *Fourth International Conference on Image and Graphics, 2007. ICIG 2007.* IEEE, 2007, pp. 519–523.

[32] Z. Yin, R. Bise, M. Chen, and T. Kanade, "Cell segmentation in microscopy imagery using a bag of local bayesian classifiers," in *2010 IEEE International Symposium on Biomedical Imaging: From Nano to Macro.* IEEE, 2010, pp. 125–128.

[33] A. Lobo, "Image segmentation and discriminant analysis for the identification of land cover units in ecology," *IEEE Transactions on Geoscience and Remote Sensing*, vol. 35, no. 5, pp. 1136–1145, 1997.

[34] J. C. Bezdek, L. Hall, and L. Clarke, "Review of MR image segmentation techniques using pattern recognition." *Medical Physics*, vol. 20, no. 4, pp. 1033–1048, 1992.

[35] T. Rohlfing, D. B. Russakoff, and C. R. Maurer, "Performance-based classifier combination in atlas-based image segmentation using expectation-maximization parameter estimation," *IEEE Transactions on Medical Imaging*, vol. 23, no. 8, pp. 983–994, 2004.

[36] K.-S. Chuang, H.-L. Tzeng, S. Chen, J. Wu, and T.-J. Chen, "Fuzzy c-means clustering with spatial information for image segmentation," *Computerized Medical Imaging and Graphics*, vol. 30, no. 1, pp. 9–15, 2006.

[37] T. McInerney and D. Terzopoulos, "Deformable models in medical image analysis: a survey," *Medical Image Analysis*, vol. 1, no. 2, pp. 91–108, 1996.

[38] Y. Boykov and G. Funka-Lea, "Graph cuts and efficient ND image segmentation," *International Journal of Computer Vision*, vol. 70, no. 2, pp. 109–131, 2006.

[39] G. Dong and M. Xie, "Color clustering and learning for image segmentation based on neural networks," *IEEE Transactions on Neural Networks*, vol. 16, no. 4, pp. 925–936, 2005.

[40] T. F. Cootes, C. J. Taylor, D. H. Cooper, and J. Graham, "Active shape models-their training and application," *Computer Vision and Image Understanding*, vol. 61, no. 1, pp. 38–59, 1995.

[41] T. F. Cootes, G. J. Edwards, C. J. Taylor *et al.*, "Active appearance models," *IEEE Transactions on Pattern Analysis and Machine Intelligence*, vol. 23, no. 6, pp. 681–685, 2001.

[42] P. Aljabar, R. A. Heckemann, A. Hammers, J. V. Hajnal, and D. Rueckert, "Multi-atlas based segmentation of brain images: atlas selection and its effect on accuracy," *Neuroimage*, vol. 46, no. 3, pp. 726–738, 2009.

[43] P. Simon, *Too Big to Ignore: The Business Case for Big Data*. John Wiley & Sons, 2013, vol. 72.

[44] S. J. Russell, P. Norvig, J. F. Canny, J. M. Malik, and D. D. Edwards, *Artificial Intelligence: A Modern Approach*. Prentice hall Upper Saddle River, 2003, vol. 2.

[45] K. Z. Mao, P. Zhao, and P.-H. Tan, "Supervised learning-based cell image segmentation for P53 immunohistochemistry," *IEEE Transactions on Biomedical Engineering*, vol. 53, no. 6, pp. 1153–1163, 2006.

[46] D. L. Pham, C. Xu, and J. L. Prince, "Current methods in medical image segmentation," *Annual Review of Biomedical Engineering*, vol. 2, no. 1, pp. 315–337, 2000.

[47] F. Sahba, H. R. Tizhoosh, and M. M. Salama, "A reinforcement learning framework for medical image segmentation," in *The 2006 IEEE International Joint Conference on Neural Network Proceedings*. IEEE, 2006, pp. 511–517.

[48] C. M. Bishop, *Pattern Recognition and Machine Learning*. Springer Science + Business Media, 2006.

[49] R. O. Duda, P. E. Hart, and D. G. Stork, *Pattern Classification*. John

Wiley & Sons, 2012.

[50] J. Friedman, T. Hastie, and R. Tibshirani, *The elements of statistical learning*. Springer series in statistics Springer, Berlin, 2001, vol. 1.

[51] B. E. Boser, I. M. Guyon, and V. N. Vapnik, "A training algorithm for optimal margin classifiers," in *Proceedings of The Fifth Annual Workshop on Computational Learning Theory*. ACM, 1992, pp. 144–152.

[52] C. Cortes and V. Vapnik, "Support-vector networks," *Machine Learning*, vol. 20, no. 3, pp. 273–297, 1995.

[53] N. Cristianini and J. Shawe-Taylor, *An Introduction to Support Vector Machines and Other Kernel-based Learning Methods*. Cambridge University Press, 2000.

[54] W. H. Press, S. A. Teukolsky, W. T. Vetterling, and B. Flannery, "Section 16.5. support vector machines," *Numerical Recipes: The Art of Scientific Computing*, 2007.

[55] S. Haykin and N. Network, "A comprehensive foundation," *Neural Networks*, vol. 2, no. 2004, 2004.

[56] S. S. Haykin, *Neural Networks and Learning Machines*. Pearson Education, 2009, vol. 3.

[57] C. M. Bishop, *Neural Networks for Pattern Recognition*. Oxford University Press, 1995.

[58] F. M. Ham and I. Kostanic, *Principles of Neurocomputing for Science*

and Engineering. McGraw-Hill Higher Education, 2000.

[59] W. Huang, N. Li, Z. Lin, G.-B. Huang, W. Zong, J. Zhou, and Y. Duan, "Liver tumor detection and segmentation using kernel-based extreme learning machine," in *Engineering in Medicine and Biology Society (EMBC), 35th Annual International Conference*, 2013, pp. 3662–3665.

[60] G.-B. Huang, Q.-Y. Zhu, and C.-K. Siew, "Extreme learning machine: theory and applications," *Neurocomputing*, vol. 70, no. 1, pp. 489–501, 2006.

[61] L. Breiman, "Random forests," *Machine Learning*, vol. 45, no. 1, pp. 5–32, 2001.

[62] A. Liaw and M. Wiener, "Classification and regression by random forest," *R News*, vol. 2, no. 3, pp. 18–22, 2002.

[63] F. Woergoetter and B. Porr. (2008) Reinforcement Learning. [Online]. Available: http://www.scholarpedia.org/article/Reinforcement_learning

[64] R. S. Sutton and A. G. Barto, *Reinforcement learning: An introduction*. MIT Press Cambridge, 1998, vol. 1, no. 1.

[65] L. Getoor, *Introduction to statistical relational learning*. MIT Press, 2007.

[66] M. Kearns and S. Singh, "Near-optimal reinforcement learning in polynomial time," *Machine Learning*, vol. 49, no. 2-3, pp. 209–232, 2002.

[67] R. Malladi, J. A. Sethian, and B. C. Vemuri, "Topology-independent shape modeling scheme," in *SPIE's 1993 International Symposium on Optics, Imaging, and Instrumentation*. International Society for Optics and Photonics, 1993, pp. 246–258.

[68] R. Malladi, J. A. Sethian, and B. C. Vemuri, "Evolutionary fronts for topology-independent shape modeling and recovery," in *European Conference on Computer Vision*. Springer, 1994, pp. 1–13.

[69] R. Malladi, J. A. Sethian, and B. C. Vemuri, "Shape modeling with front propagation: A level set approach," *IEEE Transactions on Pattern Analysis and Machine Intelligence*, vol. 17, pp. 158–175, 1995.

[70] V. Caselles, R. Kimmel, and G. Sapiro, "Geodesic active contours," in *Proceedings of Fifth International Conference on Computer Vision, 1995.*, 1995, pp. 694–699.

[71] S. Kichenassamy, A. Kumar, P. Olver, A. Tannenbaum, and A. Yezzi, "Gradient flows and geometric active contour models," in *Proceedings of Fifth International Conference on Computer Vision, 1995.*, 1995, pp. 810–815.

[72] S. Osher and R. Fedkiw, *Level Set Methods and Dynamic Implicit Surfaces*. Springer Science & Business Media, 2003, vol. 153.

[73] J. A. Sethian, *Level Set Methods and Fast Marching Methods: Evolving Interfaces in Computational Geometry, Fluid Mechanics, Computer Vision, and Materials Science*. New York, NY: Cambridge University Press, 1999, vol. 3.

[74] C. Li, C. Xu, C. Gui, and M. D. Fox, "Distance regularized level set evolution and its application to image segmentation," *IEEE Transactions on Image Processing*, vol. 19, no. 12, pp. 3243–3254, Dec. 2010.

[75] H.-K. Zhao, T. Chan, B. Merriman, and S. Osher, "A variational level set approach to multiphase motion," *Journal of Computational Physics*, vol. 127, no. 1, pp. 179–195, 1996.

[76] D. Mumford and J. Shah, "Optimal approximations by piecewise smooth functions and associated variational problems," *Communications on Pure and Applied Mathematics*, vol. 42, no. 5, pp. 577–685, 1989.

[77] Y. Wang, "Conditional random fields for image labeling," May 2009. [Online]. Available: www.cs.unc.edu/~lazebnik/fall09/random_fields.pptx

[78] J. Lafferty, A. McCallum, and F. Pereira, "Conditional random fields: Probabilistic models for segmenting and labeling sequence data," in *Proceedings of the eighteenth international conference on machine learning, ICML*, vol. 1, 2001, pp. 282–289.

[79] J. Verbeek and W. Triggs, "Scene segmentation with crfs learned from partially labeled images," in *NIPS 2007-Advances in Neural Information Processing Systems*, vol. 20. MIT Press, 2007, pp. 1553–1560.

[80] C.-H. Lee, M. Schmidt, A. Murtha, A. Bistritz, J. Sander, and R. Greiner, "Segmenting brain tumors with conditional random fields

and support vector machines," in *International Workshop on Computer Vision for Biomedical Image Applications*. Springer, 2005, pp. 469–478.

[81] D. M. Greig, B. T. Porteous, and A. H. Seheult, "Exact maximum a posteriori estimation for binary images," *Journal of the Royal Statistical Society. Series B (Methodological)*, pp. 271–279, 1989.

[82] Y. Y. Boykov and M.-P. Jolly, "Interactive graph cuts for optimal boundary & region segmentation of objects in ND images," in *Computer Vision, 2001. ICCV 2001. Proceedings. Eighth IEEE International Conference on*, vol. 1. IEEE, 2001, pp. 105–112.

[83] Y. Boykov and V. Kolmogorov, "An experimental comparison of min-cut/max-flow algorithms for energy minimization in vision," *IEEE Transactions on Pattern Analysis and Machine Intelligence*, vol. 26, no. 9, pp. 1124–1137, 2004.

[84] Y. Boykov, D. Cremers, and V. Kolmogorov, "Graph cuts vs. level sets: Global vs. local optimisation algorithms," May 2006. [Online]. Available: http://www.csd.uwo.ca/~yuri/Presentations/ECCV06_tutorial_partIV_vnk.pdf

[85] Y. Boykov, D. Cremers, and V. Kolmogorov, "Graph cuts vs. level sets: Connecting graph cuts and level sets," May 2006. [Online]. Available: http://www.csd.uwo.ca/~yuri/Presentations/ECCV06_tutorial_partIV_vnk.pdf

[86] J. Novosel, M. Ostermann, G. Thepass, H. Lemij, K. Vermeer, and L. van Vliet, "Comparison of coupled level sets and graph cuts for reti-

nal layer segmentation in optical coherence tomography," *Investigative Ophthalmology & Visual Science*, vol. 54, no. 15, pp. 1462–1462, 2013.

[87] K. O. Babalola, B. Patenaude, P. Aljabar, J. Schnabel, D. Kennedy, W. Crum, S. Smith, T. Cootes, M. Jenkinson, and D. Rueckert, "An evaluation of four automatic methods of segmenting the subcortical structures in the brain," *Neuroimage*, vol. 47, no. 4, pp. 1435–1447, 2009.

[88] B. N. Li, C. K. Chui, S. Chang, and S. H. Ong, "Integrating spatial fuzzy clustering with level set methods for automated medical image segmentation," *Computers in Biology and Medicine*, vol. 41, no. 1, pp. 1–10, 2011.

[89] K. Parmar and R. Kher, "A comparative analysis of multimodality medical image fusion methods," in *Modelling Symposium (AMS), 2012 Sixth Asia*. IEEE, 2012, pp. 93–97.

[90] G. Wang, B. N. Li, C. Chee-Kong, O. Sim-Heng, S. K. Venkatesh, and S. Chang, "Image categorization for combinatorial CT liver tumor segmentation," *International Journal of Computer Assisted Radiology and Surgery*, vol. 6, no. 1, pp. 46–52, 2011.

[91] C. Wachinger and N. Navab, "Entropy and Laplacian images: Structural representations for multi-modal registration," *Medical Image Analysis*, vol. 16, no. 1, pp. 1–17, 2012.

[92] H. Zhang, J. Liu, Z. Zhu, and H. Li, "An automated and simple method for brain MR image extraction," *BioMedical Engineering OnLine*, vol. 10, no. 81, Sep. 2011.

[93] S. Wang and R. M. Summers, "Machine learning and radiology," *Medical Image Analysis*, vol. 16, no. 5, pp. 933–951, Jul. 2012.

[94] N. E. A. Khalid, S. Ibrahim, and P. Haniff, "MRI brain abnormalities segmentation using k-nearest neighbors(k-NN)," *International Journal on Computer Science and Engineering*, vol. 3, no. 2, pp. 980–990, 2011.

[95] N. Lee, J. Caban, S. Ebadollahi, and A. Laine, "Interactive segmentation in multimodal brain imagery using a Bayesian transductive learning approach," in *SPIE Medical Imaging*. International Society for Optics and Photonics, 2009, pp. 72 601W–72 601W.

[96] Z. Wang, B. Zineddin, J. Liang, N. Zeng, Y. Li, M. Du, J. Cao, and X. Liu, "A novel neural network approach to cDNA microarray image segmentation," *Computer Methods and Programs in Biomedicine*, vol. 111, no. 1, pp. 189–198, 2013.

[97] M. A. Selver, "Segmentation of abdominal organs from CT using a multi-level, hierarchical neural network strategy," *Computer Methods and Programs in Biomedicine*, vol. 113, no. 3, pp. 830–852, 2014.

[98] M. Hassan, A. Chaudhry, A. Khan, and M. A. Iftikhar, "Robust information gain based fuzzy c-means clustering and classification of carotid artery ultrasound images," *Computer Methods and Programs in Biomedicine*, vol. 113, no. 2, pp. 593–609, 2014.

[99] Z. Ji, Q. Sun, Y. Xia, Q. Chen, D. Xia, and D. Feng, "Generalized rough fuzzy c-means algorithm for brain MR image segmentation," *Computer Methods and Programs in Biomedicine*, vol. 108, no. 2, pp. 644–655, 2012.

[100] V. Shanmugam and R. Wahida Banu, "Retinal blood vessel segmentation using an extreme learning machine approach," in *Point-of-Care Healthcare Technologies (PHT)*. IEEE, 2013, pp. 318–321.

[101] K. Zhang and W. Lu, "Automatic human knee cartilage segmentation from multi-contrast MR images using extreme learning machines and discriminative random fields," in *Machine Learning in Medical Imaging*. Springer, 2011, pp. 335–343.

[102] F. R. Cordeiro, S. M. Lima, A. G. Silva-Filho, and W. Santos, "Segmentation of mammography by applying extreme learning machine in tumor detection," in *Intelligent Data Engineering and Automated Learning-IDEAL 2012*. Springer, 2012, pp. 92–100.

[103] S. Ghose, J. Mitra, A. Oliver, R. Martí, X. Lladó, J. Freixenet, J. C. Vilanova, D. Sidibé, and F. Meriaudeau, "A random forest based classification approach to prostate segmentation in MRI," *MICCAI Grand Challenge: Prostate MR Image Segmentation*, vol. 2012, 2012.

[104] V. Lempitsky, M. Verhoek, J. A. Noble, and A. Blake, "Random forest classification for automatic delineation of myocardium in real-time 3D echocardiography," in *Functional Imaging and Modeling of the Heart*. Springer, 2009, pp. 447–456.

[105] R. Cuingnet, R. Prevost, D. Lesage, L. D. Cohen, B. Mory, and R. Ardon, "Automatic detection and segmentation of kidneys in 3D CT images using random forests," in *Medical Image Computing and Computer-Assisted Intervention–MICCAI 2012*. Springer, 2012, pp. 66–74.

[106] A. T. Azar, H. I. Elshazly, A. E. Hassanien, and A. M. Elkorany, "A random forest classifier for lymph diseases," *Computer Methods and Programs in Biomedicine*, vol. 113, no. 2, pp. 465–473, 2014.

[107] L. Wang and C. Pan, "Robust level set image segmentation via a local correntropy-based k-means clustering," *Pattern Recognition*, vol. 47, no. 5, pp. 1917–1925, 2014.

[108] J. Olivier, R. Boné, J.-J. Rousselle, and H. Cardot, "Active contours driven by supervised binary classifiers for texture segmentation," *Advances in Visual Computing*, pp. 288–297, 2008.

[109] P. R. Bai, Q. Y. Liu, L. Li, S. H. Teng, J. Li, and M. Y. Cao, "A novel region-based level set method initialized with mean shift clustering for automated medical image segmentation," *Computers in Biology and Medicine*, vol. 43, no. 11, pp. 1827–1832, 2013.

[110] S. Li, T. Fevens, and A. Krzyżak, "A SVM-based framework for autonomous volumetric medical image segmentation using hierarchical and coupled level sets," in *International Congress Series*, vol. 1268. Elsevier, 2004, pp. 207–212.

[111] H.-C. Lan, T.-R. Chang, W.-C. Liao, Y.-N. Chung, and P.-C. Chu, "Knee MR image segmentation combining contextual constrained neural network and level set evolution," in *IEEE Symposium on Computational Intelligence in Bioinformatics and Computational Biology, 2009. CIBCB'09.* IEEE, 2009, pp. 271–277.

[112] W. Huang, Z. Tan, Z. Lin, G. Huang, J. Zhou, C. Chui, Y.-C. Su, and S. Chang, "A semi-automatic approach to the segmentation of liver

parenchyma from 3D CT images with extreme learning machine," in *Engineering in Medicine and Biology Society (EMBC), 2012 Annual International Conference of the IEEE*. IEEE, 2012, pp. 3752–3755.

[113] J. Wu, Z. Yin, and Y. Xiong, "The fast multilevel fuzzy edge detection of blurry images," *IEEE Signal Processing Letters*, vol. 14, no. 5, pp. 344–347, 2007.

[114] D. Smeets, D. Loeckx, B. Stijnen, B. De Dobbelaer, D. Vandermeulen, and P. Suetens, "Semi-automatic level set segmentation of liver tumors combining a spiral-scanning technique with supervised fuzzy pixel classification," *Medical Image Analysis*, vol. 14, no. 1, pp. 13–20, 2010.

[115] S. Krinidis and V. Chatzis, "Fuzzy energy-based active contours," *IEEE Transactions on Image Processing*, vol. 18, no. 12, pp. 2747–2755, 2009.

[116] J. Platt, "Probabilistic outputs for support vector machines and comparisons to regularized likelihood methods," *Advances in Large Margin Classifiers*, vol. 10, no. 3, pp. 61–74, 1999.

[117] Z. Li, W. Wang, and P. Shui, "Parameter estimation and two-stage segmentation algorithm for the Chan-Vese model," in *IEEE International Conference on Image Processing*. IEEE, 2006, pp. 201–204.

[118] P. Getreuer, "Chan-Vese segmentation," *Image Processing On Line*, vol. 2, pp. 214–224, 2012.

[119] R. Rifkin and A. Klautau, "In defense of one-vs-all classification," *Journal of machine learning research*, vol. 5, no. Jan, pp. 101–141,

2004.

[120] C.-W. Hsu and C.-J. Lin, "A comparison of methods for multiclass support vector machines," *IEEE transactions on Neural Networks*, vol. 13, no. 2, pp. 415–425, 2002.

[121] E. Mayoraz and E. Alpaydin, "Support vector machines for multi-class classification," in *International Work-Conference on Artificial Neural Networks*. Springer, 1999, pp. 833–842.

[122] L. A. Vese and T. F. Chan, "A multiphase level set framework for image segmentation using the mumford and shah model," *International Journal of Computer Vision*, vol. 50, no. 3, pp. 271–293, 2002.

[123] X.-F. Wang and D.-S. Huang, "A novel multi-layer level set method for image segmentation," *J. Univers. Comput. Sci*, vol. 14, no. 14, pp. 2428–2452, 2008.

[124] A. Dirami, K. Hammouche, M. Diaf, and P. Siarry, "Fast multilevel thresholding for image segmentation through a multiphase level set method," *Signal Processing*, vol. 93, no. 1, pp. 139–153, 2013.

[125] D. Cremers, M. Rousson, and R. Deriche, "A review of statistical approaches to level set segmentation: integrating color, texture, motion and shape," *International Journal of Computer Vision*, vol. 72, no. 2, pp. 195–215, 2007.

[126] Y. Wang, S. Xiang, C. Pan, L. Wang, and G. Meng, "Level set evolution with locally linear classification for image segmentation," *Pattern Recognition*, vol. 46, no. 6, pp. 1734–1746, 2013.

[127] Y. Liu and Y. Yu, "Interactive image segmentation based on level sets of probabilities," *IEEE Transactions on Visualization and Computer Graphics*, vol. 18, no. 2, pp. 202–213, 2012.

[128] J. Folkesson, E. Samset, R. Y. Kwong, and C.-F. Westin, "Unifying statistical classification and geodesic active regions for segmentation of cardiac mri," *IEEE Transactions on Information Technology in Biomedicine*, vol. 12, no. 3, pp. 328–334, 2008.

[129] Y.-T. Chen and D.-C. Tseng, "Medical image segmentation based on the bayesian level set method," in *Medical Imaging and Informatics*. Springer, 2008, pp. 25–34.

[130] P. Getreuer, "Chan-Vese Segmentation," *Image Processing On Line*, vol. 2, pp. 214–224, 2012.

List of Publications

1. A. Pratondo, C.-K. Chui, and S.-H. Ong, "Region growing for medical image segmentation using a modified multiple-seed approach on a multi-core CPU computer" in *The 15th International Conference on Biomedical Engineering*, Springer International Publishing, 2013, pp. 112–115.

2. A. Pratondo, B. P. Nguyen, C.-K. Chui, and S.-H. Ong, "Vocal cord segmentation from CT images using machine learning," in *Proceedings of the 10th Asian Conference on Computer Aided Surgery (ACCAS 2014)*. The Japan Society of Computer Aided Surgery, 2014, pp. 40–41.

3. A. Pratondo, B. P. Nguyen, C.-K. Chui, and S.-H. Ong, "Pancreas segmentation on non-contrast-enhanced CT scan images" in *Proceedings of the AUN/SEED-Net Regional Conference for Computer and Information Engineering*. AUN/SEED-NET, 2015.

4. A. Pratondo, C.-K. Chui, and S.-H. Ong, "Robust edge-stop functions for edge-based active contour models in medical image segmentation," *IEEE Signal Processing Letters*, vol. 23, no. 2, pp. 222–226, 2016.

5. A. Pratondo, C.-K. Chui, and S.-H. Ong, "Integrating machine learning with region-based active contour models in medical image segmentation," accepted for publication in *Journal of Visual*

Communication and Image Representation.

6. A. Pratondo, B. P. Nguyen, C.-K. Chui, and S.-H. Ong, "A comparative study of integrating machine learning with edge-based active contour model," in preparation for publication.